IN-PLANE BLADE-HUB DYNAMICS OF HORIZONTAL-AXIS WIND TURBINES WITH TUNED AND MISTUNED BLADES

By

Ayse Sapmaz

A DISSERTATION

Submitted to
Michigan State University
in partial fulfillment of the requirements
for the degree of

Mechanical Engineering – Doctor of Philosophy

2020

ABSTRACT

IN-PLANE BLADE-HUB DYNAMICS OF HORIZONTAL-AXIS WIND TURBINES WITH TUNED AND MISTUNED BLADES

By

Ayse Sapmaz

Understanding vibration of wind turbine blades is of fundamental importance. This study focuses on the effect of blade mistuning on the coupled blade-hub dynamics. Unavoidably, the set of blades are not precisely identical due to inhomogeneous materials, manufacturer tolerances, etc.

This work is focused on the blade-hub dynamics of horizontal-axis wind turbines with mistuned blades. The reduced-order equations of motion are derived for the wind turbine blades and hub exposed to centrifugal effects and gravitational and cyclic aerodynamic forces. Although the blades and hub equations are coupled, they can be decoupled from the hub by changing the independent variable from time to rotor angle and by using a small parameter approximation. The resulting blade equations include parametric and direct excitation terms. The method of multiple scales is applied to examine response of the linearized system. This analysis shows that superharmonic and primary resonances exist and are influenced by the mistuning. Resonance cases and the relations between response amplitude and frequency are studied. Besides illustrating the effects of damping and forcing level, the first-order perturbation solutions are verified with comparisons to numerical simulations at superharmonic resonance of order two. The simulation point to speed-locking phenomenon, in which the superharmonic speed is locked in for an interval of applied mean loads. Additionally, the effect of rotor loading on the rotor speed and blade amplitudes is investigated for different initial conditions and mistuning cases. Lastly, we aim to analytically confirm the blade response amplitudes at various rotor speeds near resonance and verify speed locking phenomenon by applying method of harmonic balance. The study shows that the speed-locking is due to the average interaction between the blade vibration and rotor motion in the rotor equation, and its balance against the mean rotor moment. The phenomenon is examined for an effective (balanced) single blade-rotor system.

Next, a second-order method of multiple scales is applied in the rotor-angle domain to analyze in-plane blade-hub dynamics. A superharmonic resonance case at one third the natural frequency is revealed. This resonance case is not captured by a first-order perturbation expansion. The relationship between response amplitude and frequency is studied. Resonances under constant loading are also analyzed. The effect of blade mistuning on the coupled blade-hub dynamics is taken into account.

To better understand parametrically excited multi-degree-of-freedom behavior, approximate solutions to tuned and mistuned four-degree-of-freedom systems with parametric stiffness are studied. The solution and stability of a four-degree-of-freedom Mathieu-type system is investigated with and without broken symmetry. The analysis is done using Floquet theory with harmonic balance. A Floquet-type solution is composed of a periodic and an exponential part. The harmonic balance is applied when the Floquet solution is inserted into the original differential equation of motion. The analysis brings about an eigenvalue problem. By solving this, the Floquet characteristic exponents and the corresponding eigenvectors that give the Fourier coefficients are found in terms of the system parameters. The stability transition curve can be found by analyzing the real parts of the characteristic exponents. The frequency content can be determined by analyzing imaginary parts at the exponents. A response that involves a single Floquet exponent (and its complex conjugate) can be generated with a specific set of initial conditions, and can be regarded as a "modal response". The method is applied to both tuned and detuned four-degree-of-freedom examples.

This thesis is dedicated to my son, Burak Aral. You have made me stronger, better and more fulfilled than I could have ever imagined. I love you to the moon and back.

ACKNOWLEDGEMENTS

The journey I have taken during my PhD has been the most impactful of my life. I learned not only professional and practical skills, but also learned a lot about myself in the process.

This achievement did not come without help from many people that I am very lucky to be surrounded by. First and foremost, I would like to express my heartfelt gratitude and appreciation to my academic advisor Professor Brian F. Feeny for his unique contributions to this study and my development as researcher, scholar, and educator. Your unyieldingly positive attitude, boundless energy, and enthusiasm sustained me, while your excellence and dedication inspired me. Thank you, Dr. Feeny, for so generously providing mentorship and guidance, while also valuing me as a colleague.

I would like to thank Professor Steven Shaw for being a great instructor, and for the intellectual conversations we had, both on science and life in general, which have broadened my horizons in different directions. I have been extremely fortunate to take some classes with Dr. Shaw, from whom I learned many interesting theories and methods that helped me in my work on this dissertation. I am truly honored to have had an opportunity to work with Professor Shaw on centrifugal pendulum vibration absorber (CPVA) experiment and learn from him. I was also fortunate to learn from Professor Thomas Pence and I am very grateful for his precious inputs to my research too. His supportive comments and questions that helped improve my work by thinking out of the box. My sincerely thanks to Professor Keith Promislow for accepting being part of my dissertation committee, and his invaluable feedback and delightful suggestions on my research.

In addition to the committee, I offer sincere thanks to my former and fellow lab-mates: Scott Strachan, Venkat Ramakrishnan, Pavel Polunin, Smruti Panigrahi, Rickey Caldwell, Gizem Dilber Acar, Mustafa Acar, Xing Xing, Ming Mu, Fatemeh Afzali, Mahdieh Tanha, Gaurav Chauda, Zhaobin Zhan, Jun Guo, Aakash Gupta, Jamal Ardister, Jack Metzger. You have been consistently supportive, collaborative, insightful, and a true joy to labor alongside. You have made the lab a fun place to work. The debates, lunches, dinners, camping, jokes and driving to the conferences as well as editing advice, having coffee and ice cream, general help and friendship were all greatly appreciated. More specifically, I was so lucky to have Fatemeh and Ehsan who have been always besides me, lend me their hands when I am in need. Words cannot express my appreciation of having you always near, being the marvelous aunt and uncle to my son and being a family to us in the United States. A huge thanks goes to my wonderful friends Yen, Hayriye and Firat for listening, motivating and supporting me emotionally all the time. I feel very lucky to have you all in my life. I would also like to express my gratitude to many other doctoral students, faculties and staff of the Mechanical Engineering Department. Thank you for caring and supporting me wholeheartedly.

I gratefully acknowledge the funding received towards my PhD from the Republic of Turkey Ministry of National Education, National Science Foundation (NSF) under grant numbers CMMI-1335177 and CMMI-1435126, the MSU College of Engineering, Department of Mechanical Engineering, Graduate School, Office of International Student Service (OISS), Student Parents on the Mission (SPOM) and The Council of Graduate Students (COGS). They made this work materialized.

I most of all want to thank my family back in Turkey for their ongoing supports and unconditional love that they have given to me. Words can not express how grateful I am to my mother, Nazmiye and my father, Recep for all of the sacrifices that they've made on my behalf. Also, to my brother, Hasan Ali thanks for being the wonderful younger brother who is always protective and takes care of me. You always believed me that I would achieve things I planned even when I doubted myself. Your prayer for me was what sustained me thus far. This thesis would not have been completed without your unconditional support. I know how much you would proud of me, and just imagining your proud faces give me the strength I need for the next steps in my career. I truly respect and love my parents!

A very special word of thanks goes for my dear husband Bilal for all he has done to support me, uplift me, comfort me, and bring joy to my soul. We are not just husband and wife, but best friends and companions in both in the pursuit of the PhD and this journey in life. We have learned and experienced all the steps together how to become mom and dad adequately to our little sunshine. Also, I am thankful you for bearing with my absence from my parenting duties especially the last few weeks of my extensive dissertation study. You have been invaluable throughout this dissertation. Thank you for being part of my journey.

Last but not least, I would like to express my thanks to my beloved son, Burak Aral who has been the light of my life for the last three and half years and who has given me the extra strength and motivation to get things done with all the innocence. Thank you for being such a good boy who always cheer me up and for keeping my spirit up. I have taken a lot from our mom and son time and thank you for your understanding. You are my inspiration to achieve greatness. Without you, I would not be where I am today. Also, I would like to thank my unborn baby, who is coming in around August, for bringing the joy and happiness of our lives. Thanks to many other people whose names are not listed here.

TABLE OF CONTENTS

LIST OF TABLES

LIST OF FIGURES

CHAPTER 1

INTRODUCTION

1.1 Objectives

The purpose of this study is to advance the understanding of the wind turbine blade vibration and the dynamic relationship between the blades and hub. The blades are under the effects of gravitational and cyclic aerodynamics forces and centrifugal forces. The tangential and radial components of the gravity force create cyclic changes, causing the effective stiffness of the blade to vary the with rotational angle. Additionally, centrifugal forces affect the stiffness terms, and as the turbine rotates, the blades are exposed to cyclically varying wind forces. Therefore, parametric stiffness and direct forcing effects are taken into account in the equation of motion. Understanding these cyclic gravitational and aerodynamic loadings have fundamental importance for improving the turbine life-span and designing more reliable wind turbines structures.

Further, Mathieu-type multi degree of freedom systems with parametric excitation are studied to find the general responses. Indeed, 4DOF systems with parametic excitation matches the motivation of three-blade wind turbine and rotor.

Particularly, this work focuses on the in-plane blade-hub dynamics of a three-blade horizontal-axis wind turbine, involving cyclically changing gravitational and aerodynamic loading, and aspires to the following

1. Analyze the blade-hub dynamics of a non-identical three-blade horizontal-axis wind turbine.

2. Obtain the steady-state amplitude-frequency relations and the stabilities of the solutions for coupled mistuned three-blade equations by applying a first-order perturbation method.

3. Analyze the speed-locking phenomena both numerically and analytically by applying harmonic balance method, and interpreted for the various blades.

4. Determine the steady-state dynamics for in-plane, tuned blades of horizantal-axis wind turbine by applying a second-order method of multiple scales to the equations of motion.

5. Analyze the steady-state dynamics for in-plane, mistuned blades of wind turbine by applying a second-order perturbation analysis.

6. Obtain the general response of both tuned and mistuned four-degree-of-freedom systems with parametric excitation, and establish a basis for the transient dynamics of a three-blade turbine.

1.2 Motivation

Renewable power generation can help countries to access clean, secure, reliable and affordable energy. The world market for wind energy has been experiencing solid growth through the year 2017. Total installed capacity wordwide reached about 540 GW by the end of 2017 as seen in Fig. 1.1. According to the Global Wind Energy Council (GWEC) [2], the records in 2017 point out an increment of installed capacity of about 52 GW, taking the total installed wind energy level to about 540 GW.

Electricity generation from wind energy sources has grown consistently [3]. For the first time, montly electricity generation from the wind exceeded 8 % of total electricity generation in the United States in 2017 as shown in Fig. 1.2.

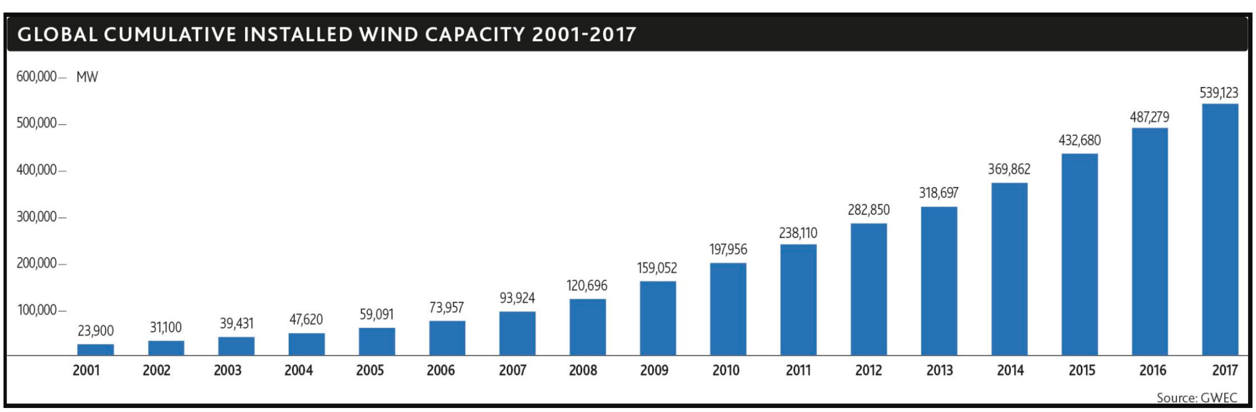

Figure 1.1: Global cumulative installed wind capacity between 2001-2017

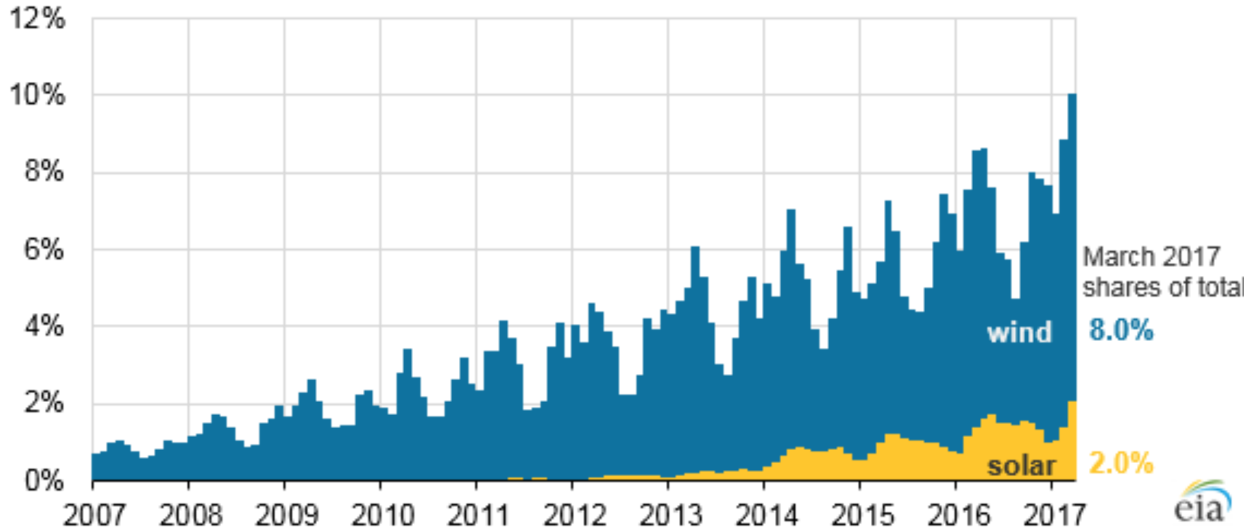

Figure 1.2: Monthly net electricity generation from selected fuels between Jan 2007- Mar 2017- share of total electricity generation.

The Wind Vision Report by Department of Energy [4] projects a scenario with wind energy supplying 10 % of the U.S. electricity in 2020, 20 % in 2030 and 35 % in 2050 total from both land-based and offshore wind energies types as seen in Fig. 1.3. Since the wind energy industry has growing export volume continuously, research on wind turbines has become more important for the global renewable energy market. This rapid growth in the wind industry has attracted attention for research and development to modify the fundamental design of wind turbines, in order to enhance gearbox and bearing life of conventional horizontal-axis wind turbines (HAWTs) and vertical-axis wind turbines (VAWT). Also essential for improving wind turbine capacity and output is blade design and technology developments [5]. Figure 1.4 shows that increasing tower height and rotor diameter allows turbines to capture more wind energy and therefore produce more electrical output, because power output of a wind turbine is proportional to the area swept by the blades [6].

Sandia National Laboratory (SNL) Wind Energy Technologies Department developed a 100 meter all-glass baseline wind turbine blade model with a 13.2 MW capacity [7]. The National Renewable Energy Laboratory (NREL) has a design of an offshore 5-MW baseline wind turbine with 61.5 m blades [8] and The Dutch Offshore Wind Energy Project (DOWEC) modeled a wind turbine with 62.6 m blades [9]. GE Renewable Energy introduced a wind turbine Haliade-X-12, the most powerful offshore wind turbine in the world, with a 12 MW capacity. It has a 220 meter rotor diameter, 107 m blades, and a 260 m height [10]. Some offshore wind developers are working together on 13 to 15 MW turbines to be in the market by 2024 (DONG Energy, 2017) [11]. However, the increase in size of turbines creates significant loading on turbine components. Therefore, there is a focus on materials fatigue and structure and equipments loadings in order to reduce gearbox failures. This is important for decreasing installation and maintanence costs as seen in Figure 1.5 [12].

Studying blade dynamics is important to understand how the blades induce loading in the hub since failures occur generally in the hub and gearbox in the horizontal-axis wind turbines. Blades are coupled through the hub so dynamical loadings of blades on rotor are transmitted to the each other by hub. A variety of dynamic loadings can induce vibrations and instabilities. So, understanding the coupled blade and hub dynamic responses is inspiring as a research problem.

1.3 Background and Literature Review

1.3.1 In-plane Blade-Hub Dynamics of Wind Turbines with Mistuned Blades

The energy produced by a wind turbine is proportional to its rotor area, which makes larger wind turbine designs more favorable [7, 8]. However, as the blades get larger in size, they become more susceptible to failure due to variations in dynamic loadings. Therefore, understanding the blade

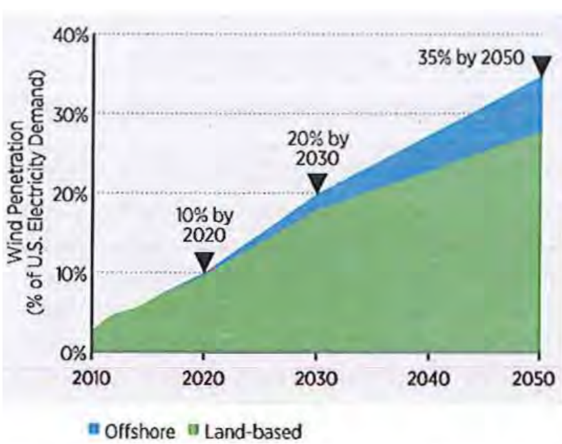

Cumulative Wind Capacity (GW)		2013	2020	2030	2050
Baseline Scenario	Land-based	61			
Central Study Scenario	Land-based	61	110	202	318
	Offshore	0	3	22	86
	Total	**61**	**113**	**224**	**404**

Figure 1.3: The Wind Vision study scenario about share in electricity production in the U.S.

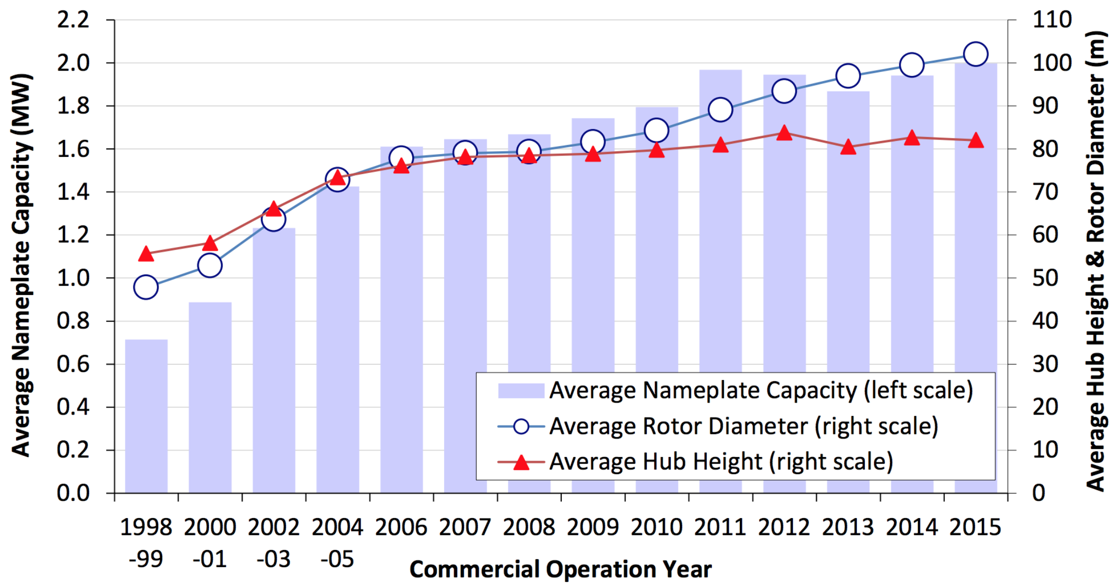

Figure 1.4: Average turbine nameplate capacity, rotor diameter, and hub height installed during period.

dynamics and blade-hub interactions is important for making predictions about turbine durability as well as building a framework for reliable designs.

In the past, researchers worked on single blade dynamics [13–17]. Ramakrishnan and Feeny [16] found a nonlinear equation of motion that governs the in-plane dynamics for a single blade. In their study, parametric and direct excitation terms due to gravity were taken into account. Through single mode reduction, the equation of motion can be represented with a forced nonlinear Mathieu equation, which was then analyzed to find the steady state dynamics via first-order method of multiple scales [16, 18]. By changing related parameters, they examined effects of parametric excitation, direct forcing and nonlinearity. Acar and Feeny derived the equations of motion for a blade under bend-bend-twist vibrations, where they accounted for stiffness changes due to gravity and centrifugal effects [17].

Reliability is one of the problems for large wind turbine designs. When horizontal-axis wind-turbine blades increase in size, variations in dynamic loading become more likely to the durability of the turbine. Understanding vibration of the blades and relationship between blades and hub have fundamental importance for predicting the turbine life-span and developing more reliable designs.

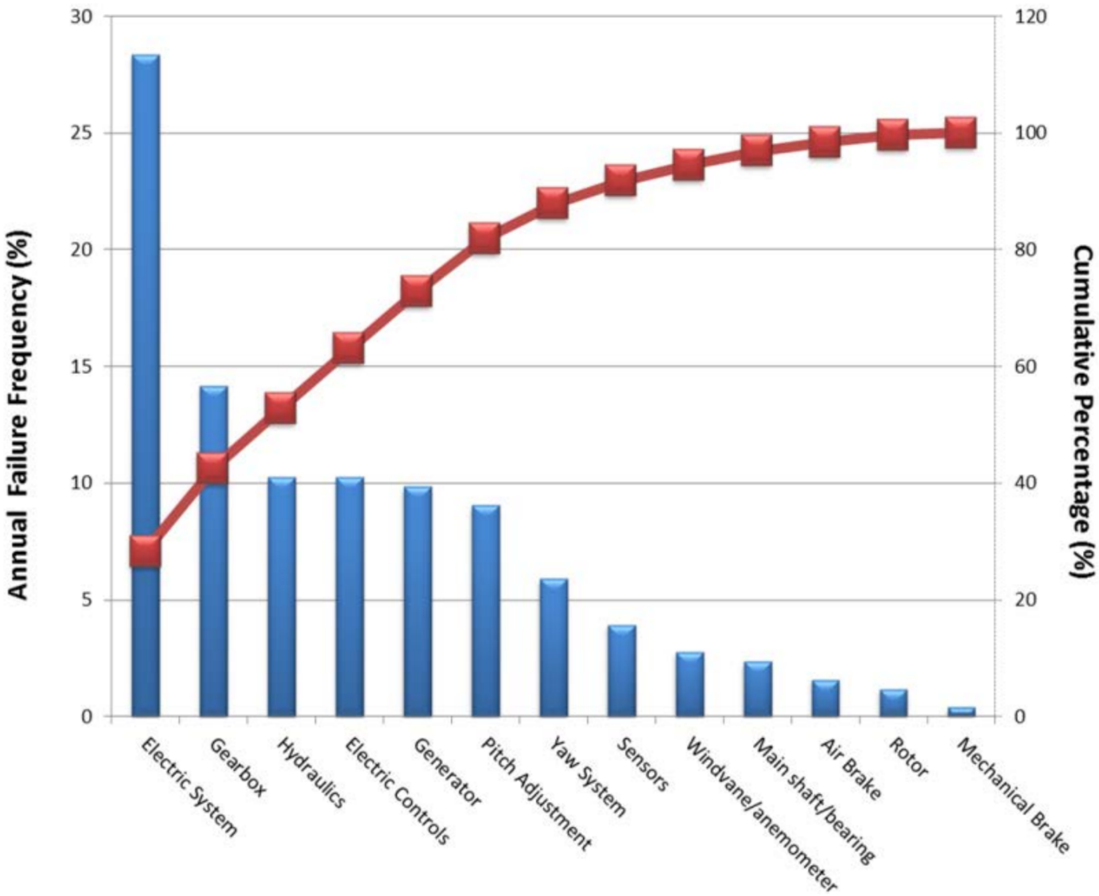

Figure 1.5: Annual Failure Frequency per Turbine Subsystem 2012.

Silva [13], Bir and Oyague [14], and Acar and Feeny [19] dealt with blade loading and vibration of a single blade. Experimental studies have been done to estimate structural and modal properties of the blade and tower of a three-bladed upwind turbine [14]. Effects of gravity, pitch action and varying rotor speed were included in the partial differential equations of blade motion by Kallesøe [15]. A dynamics model for a rotor-blade system in horizontal axis wind turbines is developed and model accuracy is improved by including additional coupling terms [20]. Ramakrishnan and Feeny [16] focused on in-plane dynamics of a single blade using a linear and nonlinear single-mode model. A first-order perturbation analysis showed that superharmonic resonances of order two existed in the linear model. They also applied a second-order perturbation method to a blade-motivated linear and nonlinear forced Mathieu equation to describe superharmonic resonances of order three [21]. A second-order method of multiple scales is applied to the equations of motion for in-plane tuned and weakly mistuned blades of horizontal axis wind turbine to determine the steady-state dynamics, with focus on the superharmonic resonance of order three for the linear system with hard forcing [22]. Inonue and Ishida [23, 24] performed the out-of phase nonlinear vibration analysis of wind turbine blade to investigate the superharmonic resonance case and they also showed the existence of superharmonic resonance at orders two and three. Higher-order perturbation expansions have been applied to study dynamics of systems [25–28]. Nayfeh and Mook [29] used higher-order perturbation method to find the stability wedges of the Mathieu equation.

1.3.2 Approximate General Reponse of Four-Degree-of-Freedom Systems with Parametric Excitation

Many mechanical systems have parametric excitation characteristics [18, 23, 30, 31]. A number of different types of methods have been used to study the Mathieu equation. The method of multiple scales has been used to examine a forced Mathieu equation for resonances [18]. Likewise, stability characteristics are found by using the method of van der Pol [23]. Another way to approach the Mathieu equation is to use Floquet theory. Acar and Feeny [32] used a method combining Floquet theory with harmonic balance to find the tuned 2-DOF and 3-DOF systems responses. An assumed Floquet-type solution is composed of a periodic $p(t)$ and an exponential part $\mathrm{e}^{\hat{\mu}t}$ such as $x(t) = \mathrm{e}^{\hat{\mu}t} p(t)$. The theory indicates that the fundamental solution to a Mathieu equation on stability boundaries is purely periodic [33]. In consequence of that, stability regions can be procured by assuming a periodic solution without solving for the general response itself [34], [24, 35–37]. The response characteristics of time-periodic systems have been studied by using system identification methods. Allen *et al.* [38] presented an output-only system identification methodology to identify the modal functions of the Mathieu equation and the Floquet exponents.

1.4 Thesis Overview

This thesis includes the analysis of in-plane blade-hub dynamics of horizontal-axis wind turbines with mistuned blades by applying perturbation analysis. In Chapter 2, low-order in-plane vibration equation of motion are derived for a mistuned three-blade wind turbine. The blade equations and the rotor equation are coupled through the inertial terms. Pendulum vibration absorber equations are similar to these equations where absorber inertia is small compared to rotor inertia [39, 40]. To decouple the absorber equations from the rotor equation, Chao *et al.* [41, 42] changed the independent variable from time to rotor angle. Following the analysis of these vibration-absorber systems, the independent variable is transformed from time to rotor angle in this work, then a non-dimensionalization procedure and a scaling process are followed to separate the blade equations from the hub equation. Next, the method of multiple scales is applied to equations of the mistuned blades to analyze the steady-state amplitude-frequency relations and the stabilities of solutions.

Moreover, in Chapter 3, second-order method of multiple scales is applied to the equations of motion for in-plane tuned and weakly mistuned blades of horizontal axis wind turbine to obtain the steady state dynamics, with focus on the superharmonic resonance of order three for the linear system with hard forcing, and also superharmonic resonances under a constant load.

Additionally, in Chapter 4, general solutions of Mathieu-type four-degree-of-freedom mass-spring system with parametric excitation are studied. Assuming a Floquet-type solution, and using the harmonic balance method, the frequency content and stability of the solution are obtained. Finally, the analysis is extended to a system with mistuned parameters, and the effect of symmetry breaking on system response is analyzed.

Lastly, Chapter 5 discusses studies which are underway but have not been completed. These include a nonlinear analysis of a single blade and an approach for parametric identification of a system with cyclic stiffness.

1.5 Contributions

Literature contibutions of this thesis are:

– Equations of motions are derived for in-plane vibrations of a mistuned three-blade wind turbine. This study allows us to determine that superharmonic and primary resonances, which were observed in the previous study of symmetric case, can be split into multiple resonance peaks, and that the blades take on different steady state amplitudes.

- The effects of parameters, such as damping, forcing level, positive and negative mistuning on the superharmonic resonant responses were analyzed. Also, the analytical solution approximations of the blade vibration and rotor dynamics with numerical solutions are verified. In doing so, the simulations expose a rotor-speed locking phenomenon at the superharmonic resonances. Additionally, the speed-locking phenomena is verified analytically by applying harmonic balanca method.

- A second-order pertubation analysis is applied on both tuned and mistuned three-blade wind turbines. The analysis reveals the superharmanic resonances at one-third natural frequency. This resonance case is not able to be captured with a first-order multiple scales analysis. The superharmonic resonance splits from a single resonance peak in the tuned case into multiple resonance peaks with mistuning. The amplitude inceases while the modal damping factor ζ decreases for steady-state superharmonic resonance response.

- General responses of a 4 degree-of-freedom mass-spring system with parametric excitation are investigated. The frequency content and stability of the solution are obtained by assuming a Floquet-type solution, and using the harmonic balance method. Further, the analysis is broaden to a system with mistuned parameters, and the effect of symmetry breaking on system response is analyzed.

CHAPTER 2

IN-PLANE BLADE-HUB DYNAMICS OF HORIZONTAL-AXIS WIND TURBINES WITH MISTUNED BLADES

2.1 Introduction

In this chapter, wind-turbine blade-hub interactions are considered as a whole. Dynamics of a linearized symmetric three-blade horizontal-axis wind turbine was studied previously in [43], where all three blades were assumed to have identical inertial and stiffness properties. In that work, the parametrically excited blade equations exhibited superharmonic and primary resonances. Since the system was linear and perfectly symmetric, each blade had the same vibration amplitude. Ikeda *et al.* investigated unstable vibrations of a two-blade wind turbine tower theoretically [44]. Nonlinearity could cause the blades to deviate from this symmetric response (e.g. in Griffin *et al.*, [45], Dick *et al.* [46]). Alternatively, in this chapter, one of the blades is mistuned to show the effects of breaking the cyclic symmetry. Many researchers worked on mistuned rotational systems [47–50]. Whitehead [51] analyzed the effect of broken-symmetry on forced vibration of turbine blades with mechanical coupling. Mistuning in bladed disks has been studied by Ewins [52] and Cha and Sinha [53]. Localization phenomenon in three-blade horizontal-axis wind turbine vibrations were analyzed by Ikeda *et al.* [54]. Approximate general responses of tuned and mistuned 4-degree-of-freedom systems with parametric stiffness were found by applying Floquet theory with harmonic balance [55].

Following up the work on a symmetric blade-hub system, the method of multiple scales is applied to equations of the mistuned blades and hub to examine the steady state dynamics. By using a procedure that is similar to the one used in [43], linearized equations of motion for non-identical blades and hub were found. By assuming a single uniform cantilever beam mode for each blade, energy equations are approximated. Then, blade and hub equations are obtained by applying Lagrange's equations [43]. The tangential and radial components of the gravity force create cyclic changes, varying the effective stiffness of the blade with rotational angle. Also, centrifugal forces contribute to the stiffness as the rotor spins. Although horizontal-axis wind-turbines do not spin at high speeds generally, the stiffness contribution of centrifugal effects should be taken into account while designing turbine blades. Moreover, wind velocity generally varies with altitude, the blades are exposed to cyclically varying wind forces as the blade rotates. In the equations of motion, parametric stiffness and direct forcing effects were taken into consideration. Derivation of equations can be found from [17].

In place of assuming a symmetric model, in this study, we mistune one of the blades in order to understand how broken-symmetry affects the turbine dynamics. As can be seen in the following sections, even when the mistuning is small, it can introduce larger forced responses when compared to the perfectly tuned system. The blade-hub dynamics of a non-identical three-blade horizontal axis wind turbine, involving cyclically changing aerodynamic loadings, direct and parametric excitation is analyzed. Primary resonance and superharmonic resonance at order 2 were unfolded due to the parametric and direct excitation of gravity. The blade equations and the rotor equation are coupled through the inertial terms.

Pendulum vibration absorber equations are similar to these equations where absorber inertia is small compared to rotor inertia [39, 40]. To decouple the absorber equations from the rotor equation, Chao *et al.* [41, 42] changed the independent variable from time to rotor angle. Then they applied method of averaging to find steady state dynamics. Gravitational effects on absorbers and the internal resonances introduced by the parametric effect were studied by Theisen [56].

Like with the analysis of these vibration-absorber systems, the independent variable is transformed from time to rotor angle in this work, and then, a non-dimensionalization procedure and a scaling process are followed. To analyze the steady-state amplitude-frequency relations and the stabilities of solutions for coupled mistuned three-blade equations, a first-order method of multiple scales is applied. This analysis is focused on superharmonic resonance and a primary resonance.

This chapter also includes the effects of parameters, notably negative mistuning, damping, and forcing level, on the superharmonic resonant responses. On the other hand, the analytical solution

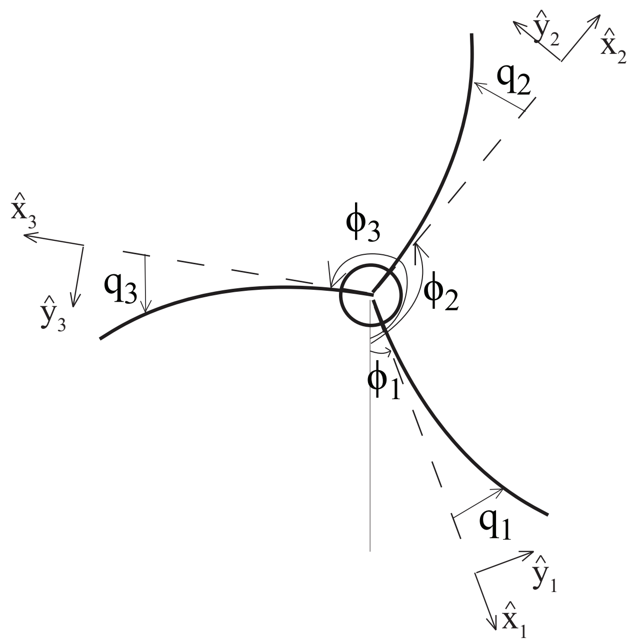

Figure 2.1: A mistuning three-blade turbine with blades under in-plane bending.

approximations of the blade vibration and rotor dynamics with numerical solutions is verified. In doing so, the simulations expose a rotor-speed locking phenomenon at the superharmonic resonances. Last, the speed-locking phenomenon and the blade response amplitudes at various rotor speeds near resonance are verified analytically by applying harmonic balanca method.

2.2 Mistuned Three-Blade Turbine Equations

Following reference [43], the hub is modeled as a rigid body in a fixed-axis rotation with damping. As shown in Figure 2.1, only in-plane vibration is taken into consideration by using a simplified model, and tower motion is neglected. The blades and rotor equations are coupled. The blades are modeled as nonuniform slender beams of length L with in-plane transverse displacement $y(x,t) \cong \gamma_v(x) q_j(t)$, where $\gamma_v(x)$ is the assumed modal displacement function of position x, and $q_j(t)$ is the modal coordinate of the j^{th} blade. One of the blades' elastic modal stiffness terms is assumed to have a small mistuning.

The equations of motion for the j^{th} blade and the rotor are, for $j = 1$, 2 and 3,

$$m_b\ddot{q}_j + c_b\dot{q}_j + (k_{0_j} + k_1\dot{\phi}^2 + k_2\cos\phi_j)q_j + d\sin\phi_j + e\ddot{\phi} = Q_j, \tag{2.1}$$

$$J_r\ddot{\phi} + c_r\dot{\phi} + \sum_{k=1}^{3}(d\cos\phi_k q_k + e\ddot{q}_k) = Q_\phi, \tag{2.2}$$

where $k_{0_1} = k_{0_2} = k_0$, $k_{0_3} = k_0 + \epsilon k_v$ and k_0 is a single blade's elastic stiffness, k_v is the elastic stiffness variation of the mistuned blade, m_b is the modal mass of a single blade according to the equation given in the Appendix A.1, J_r is the total inertia of three blades plus the hub about the shaft axis, e is the coupling term, q_j is the assumed modal coordinate for the j^{th} blade, ϕ is the rotor angle, and $\phi_j = \phi + \frac{2\pi}{3}j$ is the blade-root angle, which differs from ϕ by a constant (i.e. $\phi_1 = \phi + 2\pi/3$, $\phi_2 = \phi + 4\pi/3$, $\phi_3 = \phi$), $k_1\dot{\phi}^2$ is the centrifugal stiffness, k_2 is the stiffness contribution of the gravitational effect, Q_j and Q_ϕ are generalized forcing terms due to aeroelastic loading, and c_b and c_r are generic damping coefficients. These parameters are defined in the Appendix A.1.

For a system under zero gravity, the first two modal frequencies are: $\omega_{n1} = 0$ with mode shape $\vartheta_1 = (q_1, q_2, q_3, \phi) = (0, 0, 0, 1)$ (rigid body rotation), $\omega_{n2} = \sqrt{\dfrac{k_0 + k_1\Omega^2}{m_b}}$ (frequency of a single blade) with $\vartheta_2 = (0.707, -0.707, 0, 0)$. The third and the fourth modal frequencies are rather complicated, and they are given in the Appendix A.2. For specific parameter values, the natural frequencies are plotted as functions of the stiffness variation term (k_v), as demonstrated in Figure 2.2. When $k_v = 0$, the symmetric case, $\omega_{n3} = \omega_{n2}$, which is consistent with [43]. Schematic blade-rotor mode shapes are given in Figure 2.3 for the symmetric case. For the mistuned blades case, first and second mode shapes are the same as shown in Figure 2.3, but the third and forth mode shapes are slightly perturbed. In the case of mode 2, the mistuned blade and hub are motionless while the tuned blades vibrate equally and oppositely.

Similar to references [39, 41–43], the independent variable is changed from time to rotor angle ϕ. The rotor speed $\dot{\phi}$ is not constant. By $\nu = \dot{\phi}/\Omega$, where Ω is the mean speed, one can find the derivative expressions:

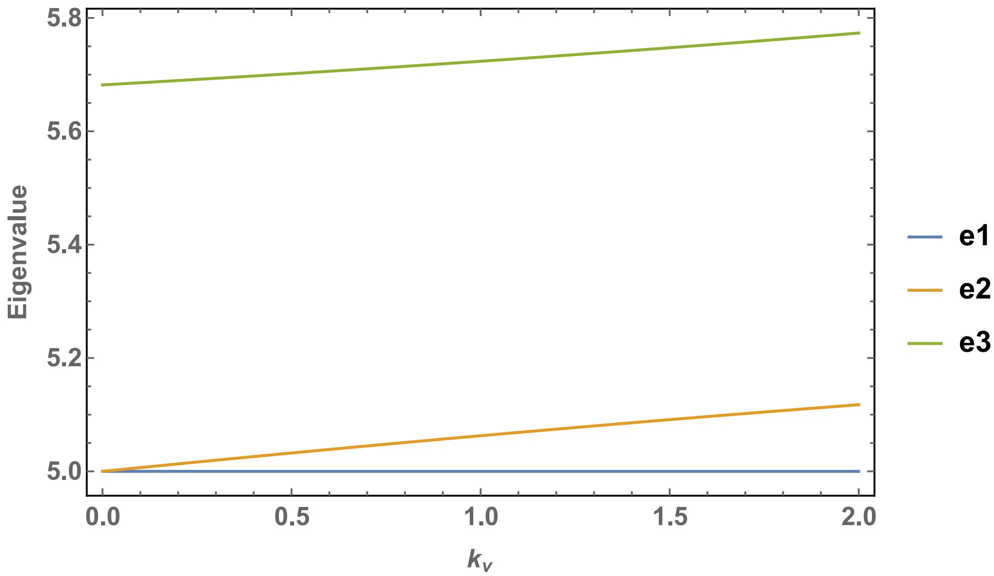

Figure 2.2: Eigenvalues versus elastic stiffness mistuning parameter (k_v) plot for $k_0 = 5$, $k_1 = 0.5$, $\dot{\Phi} = 0$, $m = 1$, $J = 1$, $e = 0.2$, $\epsilon = 0.1$ (e1: first blade, e2: second blade, e3: third blade)

$$\frac{\mathrm{d}}{\mathrm{d}t} = \frac{\mathrm{d}\phi}{\mathrm{d}t}\frac{\mathrm{d}}{\mathrm{d}\phi} \quad \text{and} \quad \frac{\mathrm{d}^2}{\mathrm{d}t^2} = \nu'\nu\Omega^2\frac{\mathrm{d}}{\mathrm{d}\phi} + \nu^2\Omega^2\frac{\mathrm{d}^2}{\mathrm{d}\phi^2}\ .$$

Equations (2.1) and (2.2) are modified with rotor angle as the new independent variable. The equations become

$$\nu^2 q_j'' + \nu\nu' q_j' + \tilde{c}_b \nu q_j' + (\tilde{k}_{0_j} + \tilde{k}_1\nu^2 + \tilde{k}_2\cos\phi_j)q_j + \tilde{d}\sin\phi_j + \tilde{e}\nu\nu' = \tilde{Q}_j, \tag{2.3}$$

$$\nu\nu' + \tilde{c}_r\nu + \chi\sum_{k=1}^{3}\left[\tilde{d}\cos\phi_k q_k + \tilde{e}(\nu^2 q_k'' + \nu\nu' q_k')\right] = \tilde{Q}_\phi, \tag{2.4}$$

where $()' = d()/d\phi$, and $\tilde{k}_{0_1} = \tilde{k}_{0_2} = \tilde{k}_0$ and $\tilde{k}_{0_3} = \tilde{k}_0 + \epsilon\tilde{k}_v$ and where $\tilde{c}_b = \dfrac{c_b}{m_b\Omega}$, $\tilde{e} = \dfrac{e}{m_b}$,

$\tilde{k}_0 = \dfrac{k_0}{m_b\Omega^2}$, $\tilde{k}_v = \dfrac{k_v}{m_b\Omega^2}$, $\tilde{k}_1 = \dfrac{k_1}{m_b}$, $\tilde{k}_2 = \dfrac{k_2}{m_b\Omega^2}$, $\tilde{d} = \dfrac{d}{m_b\Omega^2}$, $\tilde{Q}_j = \dfrac{Q_j}{m_b\Omega^2}$, $\chi = \dfrac{m_b}{J_r}$,

$\tilde{c}_r = \dfrac{c_r}{J_r\Omega}$, $\tilde{Q}_\phi = \dfrac{Q_\phi}{J_r\Omega^2}$.

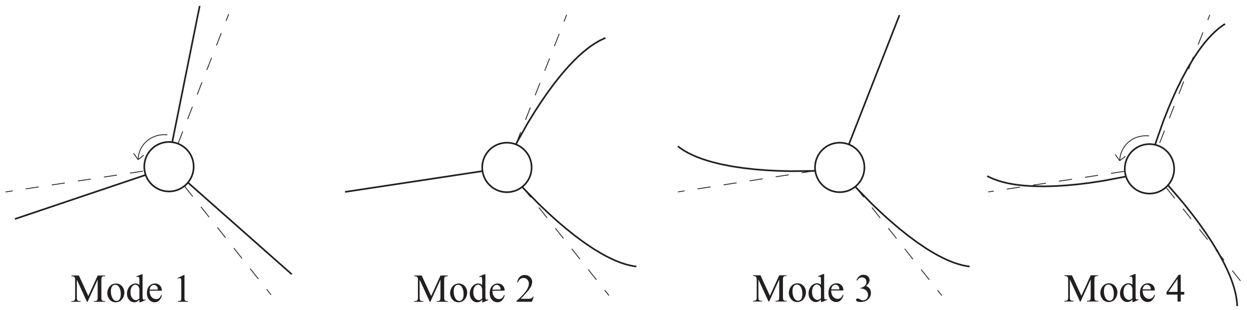

Figure 2.3: In-plane mode shapes of a symmetric three-blade turbine.

The term $\nu\nu'$ refers to the variations in the rotor speed, and can be called the dimensionless rotor acceleration ($\frac{d\nu}{dt} = \frac{d\nu}{d\phi}\frac{d\phi}{dt} = \nu'(\Omega\nu)$). This can be seen from Equation (2.4), where the summation represents the loads applied by the blades on the rotor.

The parameter J_r contains inertia of the three undeformed blades and the hub inertia about the shaft axis. m_b is the cumulative inertia of elements of a single modally displaced blade about the transverse axes of their own undeflected positions. Since m_b is small compared to J_r, a small parameter is defined as $\epsilon = m_b/J_r$. The expressions for these parameters can be found in the Appendix A.1. For the purpose of the decoupling of the blade-hub equations, the following scaling is applied to Equation (2.3) and Equation (2.4):

$$\nu = 1 + \epsilon^2\nu_1, \quad \tilde{c}_b = \epsilon\hat{c}_b, \quad \tilde{k}_2 = \epsilon\hat{k}_2, \quad \tilde{d} = \epsilon\hat{d}, \quad \tilde{c}_r = \epsilon^2\hat{c}_r, \quad \chi = \epsilon, \quad q_j = \epsilon s_j, \quad \tilde{Q}_j = \epsilon\hat{Q}_j,$$
$$\tilde{Q}_\phi = \epsilon^2\hat{Q}_\phi.$$

The equations are revised with respect to scaled blade coordinates s_j and hub coordinate ν_1 as

$$s_j'' + \epsilon\hat{c}_b s_j' + (\tilde{k}_{0_j} + \tilde{k}_1 + \epsilon\hat{k}_2\cos\phi_j)s_j + \hat{d}\sin\phi_j + \epsilon\tilde{e}\nu_1' = \hat{Q}_j + H.O.T., \tag{2.5}$$

$$\nu_1' + \hat{c}_r + \sum_{k=1}^{3}(\epsilon\hat{d}\cos\phi_k s_k + \tilde{e}s_k'') = \hat{Q}_\phi + H.O.T. \tag{2.6}$$

where H.O.T stands for higher-order terms.

The constant elastic stiffness term $\tilde{k}_{0_j}$ is larger relative to the $\tilde{k}_1$ and $\tilde{k}_2$ terms. These can be evaluated according to the equations which can be found in the Appendix A.1.

v_1' which is obtained from Equation (2.6) is inserted into Equation (2.5) to get

$$s_j'' + \epsilon\hat{c}_b s_j' + (\tilde{k}_{0_j} + \tilde{k}_1 + \epsilon\hat{k}_2\cos\phi_j)s_j + \hat{d}\sin\phi_j + \epsilon\tilde{e}\left[\hat{Q}_\phi - \hat{c}_r - \sum_{k=1}^{3}(\epsilon\hat{d}\cos\phi_k s_k + \tilde{e}s_k'')\right]$$
$$= \hat{Q}_j + H.O.T. \tag{2.7}$$

$\hat{Q}_j$ and $\hat{Q}_\phi$ are generalized forcing terms due to aeroelastic loading and are simplified as a mean plus small variation, as $\hat{Q}_j = Q_{j0} + \epsilon\hat{Q}_{j1}(\phi)$ and $\hat{Q}_\phi = Q_{\phi 0} + \epsilon\hat{Q}_{\phi 1}(\phi)$. Blade speed is approximated by the rotor speed (i.e. $u_{blade} = \dot{\phi}x$). It is assumed that the flow is steady and the wind speed increases linearly with height h (i.e. $u_{wind} = u_0 + \epsilon h u_1 = u_0 - \epsilon\cos\phi_j u_1$). This indicates that the relative speed contains ϕ and $\dot{\phi}$ terms. The detailed assumption and form of the aerodynamics force can be found in the Appendix A.1. Inserting $\tilde{k}_{0_j} = \tilde{k}_0 + \epsilon\tilde{k}_{v_j}$, $\hat{k}_0 = \tilde{k}_0 + \tilde{k}_1$, and $\phi_j = \phi + \dfrac{2\pi}{3}j$ into Equation (2.7) and reorganizing terms, we get the decoupled blade equations as

$$s_j'' + \hat{k}_0 s_j = Q_{j0} - \hat{d}\sin\left(\phi + \tfrac{2\pi}{3}j\right) + \epsilon\left[Q_{j1}\cos\left(\phi + \tfrac{2\pi}{3}j\right) - \tilde{e}Q_{\phi 0} + \tilde{e}\hat{c}_r - \hat{c}_b s_j' - \tilde{k}_{v_j}s_j\right.$$
$$\left.-\hat{k}_2\cos\left(\phi + \tfrac{2\pi}{3}j\right)s_j + \tilde{e}^2\sum_{k=1}^{3}s_k''\right], \tag{2.8}$$

for $j = 1, 2$, and 3, where $\tilde{k}_{v_1} = \tilde{k}_{v_2} = 0$ and $\tilde{k}_{v_3} = \tilde{k}_v$, and the term with $\hat{k}_2$ is the gravitational parametric excitation. $p_1 = \sqrt{\dfrac{k_0/\Omega^2 + k_1}{m_b}}$ is the modal order of the unexcited angle-based system equation. The time-based system natural frequency is scaled by Ω, such as $p_1 = \omega_{n2}/\Omega$.

As we noted before, blades are coupled through the inertial terms. One way to handle this is to make a coordinate transformation to get the equations coupled through the stiffness terms, and then apply an averaging method to study the steady state dynamics. Alternatively, the system with inertial coupling can be studied by using a Fourier matrix, as expressed in [57]. The method of multiple scales can also be used to get the relations of the slow flow. In this paper, we used the method of multiple scales to analyze the internal resonances.

2.3 Multiple-Scales Analysis

We rewrite the equations of motion in terms of new independent variable $\psi = p_1\phi$, where $p_1 = \sqrt{\hat{k_0}} = \sqrt{\dfrac{k_0/\Omega^2 + k_1}{m_b}}$.

The scaled equations of motion in the ψ domain are

$$s_j'' + s_j = F_j - \delta \sin\left(\omega_1\psi + \tfrac{2\pi}{3}j\right) + \epsilon\left[F_{j1}\cos\left(\omega_1\psi + \tfrac{2\pi}{3}j\right) + f - \hat{\zeta}s_j' - \kappa_{v_j}s_j + \tilde{e}^2\sum_{k=1}^{3} s_k'' \right.$$
$$\left. -\kappa\cos\left(\omega_1\psi + \tfrac{2\pi}{3}j\right)s_j\right], \tag{2.9}$$

where now $(\,)' = \dfrac{d}{d\psi}$ and $F_j = \dfrac{Q_{j0}}{\hat{k}_0}$, $\delta = F_{j0} = \dfrac{\hat{d}}{\hat{k}_0}$, $\omega_1 = \dfrac{1}{p_1}$, $F_{j1} = \dfrac{Q_{j1}}{\hat{k}_0}$, $\hat{\zeta} = \dfrac{\hat{c}_b}{p_1}$,

$f = \dfrac{\tilde{e}(\hat{c}_r - Q_{\phi 0})}{\hat{k}_0}$, $\kappa = \dfrac{\hat{k}_2}{\hat{k}_0}$, $\kappa_{v_j} = \dfrac{\tilde{k}_{v_j}}{\hat{k}_0}$

The parameter ω_1 is a scaled "excitation order", and is given by

$$\omega_1 = \frac{\Omega}{\omega_{n2}},$$

where $\omega_{n2} = \sqrt{\dfrac{k_0 + k_1\Omega^2}{m_b}}$ is a modal frequency of the turbine. As a result, when the mean rotor speed, Ω, varies, the excitation order ω_1 will vary as well.

The steady state dynamics of the decoupled blade equations is analyzed by applying a first-order method of multiple scales [29]. s_j has slow and fast scales (ψ_0, ψ_1) and is split into dominant solution s_{j0} and a variation of that solution s_{j1}, i.e. $s_j = s_{j0}(\psi_0, \psi_1) + \epsilon s_{j1}(\psi_0, \psi_1)$, where $\psi_i = \epsilon^i \psi_0$. Then $d/d\psi = D_0 + \epsilon D_1$, where $D_i = \partial/\partial\psi_i$. These formulations are inserted into Equation (2.9) and then we separate out the coefficients of ϵ^0 and ϵ^1.

The equation for the coefficient of ϵ^0:

$$D_0^2 s_{j0} + s_{j0} = F_j - \delta \sin\left(\omega_1\psi_0 + \frac{2\pi}{3}j\right) \tag{2.10}$$

The equation for the coefficient of ϵ^1:

$$2D_0D_1s_{j0} + D_0^2 s_{j1} + s_{j1} = F_{j1}\cos\left(\omega_1\psi_0 + \tfrac{2\pi}{3}j\right) + f - \hat{\zeta}D_0 s_{j0} + \kappa_{v_j} s_{j0} - \kappa\cos\left(\omega_1\psi_0 + \tfrac{2\pi}{3}j\right)s_{j0}$$
$$+\tilde{e}^2 \textstyle\sum_{k=1}^{3} D_0^2 s_{k0} \tag{2.11}$$

s_{j0} is found as the solution of Equation (2.10):

$$s_{j0} = \frac{F_j}{2} + A_j e^{i\psi_0} + \mathrm{i}Be^{i(\omega_1\psi_0 + \frac{2\pi}{3}j)} + c.c. \tag{2.12}$$

where A_j is complex and $B = \dfrac{\delta}{2(1-\omega_1^2)}$.

Inserting the solution for s_{j0}, $D_0 s_{j0} = \mathrm{i}A_j\mathrm{e}^{\mathrm{i}\psi_0} - B\omega_1\mathrm{e}^{\mathrm{i}(\omega_1\psi_0 + \frac{2\pi}{3}j)} + c.c.$, and $D_0D_1s_{j0} = \mathrm{i}A_j'\mathrm{e}^{\mathrm{i}\psi_0} + c.c.$ into Equation (2.11) , we find the s_{j1} equation:

$$D_0^2 s_{j1} + s_{j1} = \frac{F_{j1}}{2} e^{i(\omega_1 \psi_0 + \frac{2\pi}{3} j)} + \frac{f}{2} - 2\mathrm{i}A_j' e^{i\psi_0} - \frac{F_j}{2} \kappa e^{i(\omega_1 \psi_0 + \frac{2\pi}{3} j)} - \kappa i \frac{B}{2} e^{2i(\omega_1 \psi_0 + \frac{2\pi}{3} j)}$$

$$+\kappa_{v_j} (\frac{F_j}{2} + A_j e^{i\psi_0} + Bie^{i(\omega_1 \psi_0 + \frac{2\pi}{3} j)}) + \tilde{e}^2 \sum_{k=1}^{3} \left(-A_k e^{i\psi_0} - i\omega_1^2 B e^{i(\omega_1 \psi_0 + \frac{2\pi}{3} k)} \right)$$

$$-\frac{\kappa}{2} \left(A_j e^{i(\omega_1+1)\psi_0 + i\frac{2\pi}{3} j} + \bar{A}_j e^{i(\omega_1-1)\psi_0 + i\frac{2\pi}{3} j} \right) - \hat{\zeta} \left(A_j i e^{i\psi_0} - \omega_1 B e^{i(\omega_1 \psi_0 + \frac{2\pi}{3} j)} \right) + c.c. \tag{2.13}$$

The solvability condition for Equation (2.13) is obtained by eliminating secular terms. The solvability condition depends on the resonance case.

2.3.1 Nonresonant Case

We eliminate coefficients of $e^{i\psi_0}$ which constitute the secular terms and the solvability condition is found

$$-2\mathrm{i}A_j' - \mathrm{i}\hat{\zeta} A_j - \kappa_{v_j} A_j - \tilde{e}^2 \sum_{k=1}^{3} A_k = 0.$$

Writing $A_j = X_j + \mathrm{i}Y_j$, and splitting the above equation into real and imaginary parts, we obtain

Real part:

$$Y_j' = -\frac{\hat{\zeta}}{2} Y_j + \frac{\kappa_{v_j}}{2} X_j + \frac{\tilde{e}^2}{2} \sum_{k=1}^{3} X_k, \tag{2.14}$$

Imaginary part:

$$X_j' = -\frac{\hat{\zeta}}{2} X_j - \frac{\kappa_{v_j}}{2} Y_j - \frac{\tilde{e}^2}{2} \sum_{k=1}^{3} Y_k. \tag{2.15}$$

Representing in Equation (2.14) and Equation (2.15) matrix form

$$
\begin{pmatrix} X_1' \\ X_2' \\ X_3' \\ Y_1' \\ Y_2' \\ Y_3' \end{pmatrix} = \frac{1}{2} \begin{bmatrix} -\hat{\zeta} & 0 & 0 & -\tilde{e}^2 & -\tilde{e}^2 & -\tilde{e}^2 \\ 0 & -\hat{\zeta} & 0 & -\tilde{e}^2 & -\tilde{e}^2 & -\tilde{e}^2 \\ 0 & 0 & -\hat{\zeta} & -\tilde{e}^2 & -\tilde{e}^2 & -(\tilde{e}^2+\kappa_{v_j}) \\ \tilde{e}^2 & \tilde{e}^2 & \tilde{e}^2 & -\hat{\zeta} & 0 & 0 \\ \tilde{e}^2 & \tilde{e}^2 & \tilde{e}^2 & 0 & -\hat{\zeta} & 0 \\ \tilde{e}^2 & \tilde{e}^2 & (\tilde{e}^2+\kappa_{v_j}) & 0 & 0 & -\hat{\zeta} \end{bmatrix} \begin{pmatrix} X_1 \\ X_2 \\ X_3 \\ Y_1 \\ Y_2 \\ Y_3 \end{pmatrix}. \tag{2.16}
$$

At steady state, the solution is $X_j = 0$ and $Y_j = 0$. Eigenvalues of the system define the stability. As such, $\lambda_{1,2} = -\hat{\zeta}$, and $\lambda_{3,4,5,6}$ can be found in the Appendix A.2, for which it can be shown that the real parts are all negative if $\hat{\zeta} < 0$.

The matrix in Equation (2.16) has the form $\boldsymbol{A} = \frac{1}{2}(-\hat{\zeta}\boldsymbol{I}+\boldsymbol{B})$. Eigenvalues satisfy $\mid \boldsymbol{B}-\hat{\zeta}\boldsymbol{I}-\lambda\boldsymbol{I} \mid = \mid \boldsymbol{B}-\gamma\boldsymbol{I} \mid = 0$, where $\gamma = \hat{\zeta}+\lambda$. Since $\boldsymbol{B} = -\boldsymbol{B}^T$, its eigenvalues $\gamma = \pm\mathrm{i}\omega$ are imaginary, and hence dynamical system eigenvalues $\lambda = -\hat{\zeta} \pm \mathrm{i}\omega$ indicate stability.

2.3.2 Superharmonic Resonance ($2\omega_1 \approx 1$ or $2\Omega \approx \omega_{n2}$), $\quad 2\omega_1 = 1 + \epsilon\sigma$

A first-order multiple scales analysis of the symmetric case [43] showed the existence of superharmonic resonance at half the second natural frequency of the system. Ramakrishnan and Feeny [21] have shown that a second-order perturbation analysis of a single-blade model also reveals superharmonic resonances with order of 3.

We eliminate coefficients of secular terms in Equation (2.13) that are leading to an unbounded solution and find the solvability condition for $2\omega_1 \approx 1$ as

$$
-2\mathrm{i}A_j' - \mathrm{i}\hat{\zeta}A_j - \kappa_{v_j}A_j - \mathrm{i}\frac{B\kappa}{2}\mathrm{e}^{\mathrm{i}(\sigma\psi_1+\frac{4\pi}{3}j)} - \tilde{e}^2\sum_{k=1}^{3}A_k = 0.
$$

We insert $A_j = \Lambda_j \mathrm{e}^{\mathrm{i}(\sigma\psi_1+\frac{4\pi}{3}j)}$ with $\Lambda_j = X_j + \mathrm{i}Y_j$ into above equation, and then we can split up the real and imaginary parts as below.

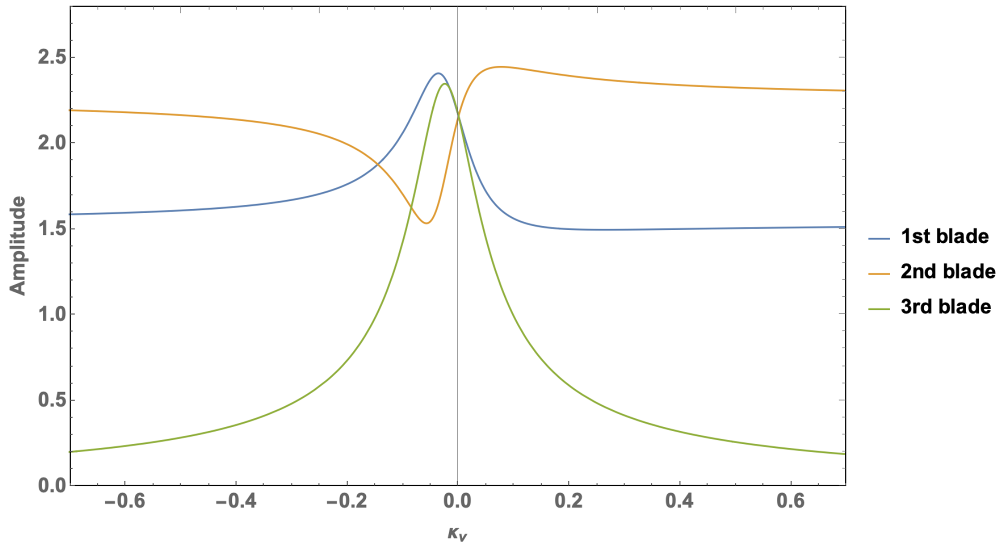

Figure 2.4: Steady-state superharmonic resonance blade response amplitudes versus elastic stiffness mistuning parameter κ_v for $\tilde{e} = 0.2$, $\sigma = -0.0064$, $\kappa = 0.1$, $|B| = 1$, $\hat{\zeta} = 0.0445$. The third blade is the mistuned blade.

Real part:

$$Y_j' = -\sigma X_j - \frac{\hat{\zeta}}{2} Y_j + \frac{\kappa_{v_j}}{2} X_j + \frac{\tilde{e}^2}{2} \sum_{k=1}^{3} \left[X_k \cos\left(\frac{2\pi}{3}(k-j)\right) - Y_k \sin\left(\frac{2\pi}{3}(k-j)\right) \right], \tag{2.17}$$

Imaginary part:

$$X_j' = \sigma Y_j - \frac{\hat{\zeta}}{2} X_j - \frac{\kappa_{v_j}}{2} Y_j - \frac{B\kappa}{4} - \frac{\tilde{e}^2}{2} \sum_{k=1}^{3} \left[X_k \sin\left(\frac{2\pi}{3}(k-j)\right) + Y_k \cos\left(\frac{2\pi}{3}(k-j)\right) \right]. \tag{2.18}$$

The steady-state response amplitude is $A_j = \sqrt{X_j^2 + Y_j^2}$, and so using X_j and Y_j we can determine A_j. Figure 2.4 shows the amplitudes of each blade as the mistuning parameter κ_v is varied, for the case when $\sigma = -0.0064$, $\tilde{e} = 0.2$, $\kappa = 0.1$, $\hat{\zeta} = 0.0445$ and $|B| = 1$. When $\kappa_v = 0$, each blade has the same amplitude, consistent with [43]. This amplitude matches with the amplitudes of the blades at resonance for the symmetric case ($\kappa_v = 0$) for same set of parameters. For both small negative and positive mistunings shown in Figure 2.4, the blade amplitudes go through variations. For larger magnitude mistuning, the mistuned blade (third blade) amplitude is decreased. Very small mistunings are the worst in the sense that one blade undergoes larger vibration amplitudes than in the symmetric case. Since Figure 2.5 stands for tuned case, Figure 2.6, Figure 2.7 and Figure 2.8

show the superharmonic resonance amplitudes as functions of the detuning parameter (excitation order or frequency), for various mistunings. The mistunings cause the single resonance peak of the symmetric case [43] to split up, thereby broadening the bandwidth of the system resonance. In these figures, two of the three peaks can be identified as superharmonic resonances of modal frequencies ω_{n2} and ω_{n3}.

In comparison to the symmetric case in Figure 2.5, the example in Figure 2.6 shows that the mistuning can also cause an increased vibration amplitude in one of the blades depending on the value of κ_v. Additionally, amplitude versus frequency plots are shown in Figure 2.9 and Figure 2.10 for each blade with a specific set of parameters. When $\hat{\zeta}$ decreases, the resonance amplitude gets sharpened and when $B\kappa$ increases the amplitude curve is raised as well. In all figures, the parameter $\hat{\zeta}$ relates to the damping factor ζ through $\epsilon\hat{\zeta} = 2\zeta$.

The solution in the ϕ domain is reorganized as

$$s_j = F_{j0} + 2B\sin(\phi + \frac{2\pi}{3}j) + a_j\cos(p_1\phi + \beta_j + \frac{4\pi}{3}j) \tag{2.19}$$

where $a_j = 2\sqrt{X_j{}^2 + Y_j{}^2}$ and $\beta_j = \tan^{-1}(\frac{Y_j}{X_j})$. To analyze the rotor dynamics, the s_j are inserted into Equation (2.6) to obtain

$$\begin{aligned} \tfrac{d\nu_1}{d\phi} = \hat{Q}_\phi - \hat{c}_r - \textstyle\sum_{k=1}^{3} \Big[& \epsilon\hat{d}\cos\phi\big[F_{k0} + 2B\sin(\phi + \tfrac{2\pi}{3}k) + a_k\cos(p_1\phi + \beta_k + \tfrac{4\pi}{3}k)\big] \\ & -\tilde{e}\big[2B\sin(\phi + \tfrac{2\pi}{3}k) + a_k p_1^2\cos(p_1\phi + \beta_k + \tfrac{4\pi}{3}k)\big]\Big] \end{aligned} \tag{2.20}$$

For all k, the nondimensionalized mean aerodynamic force terms $F_{k0} = Q_{k0}/\hat{k}_0$ are the same.

By letting $\Omega \approx \frac{d\phi}{dt}$ and using $\nu = 1 + \epsilon\nu_1$, the rotor acceleration is $\frac{d\nu}{dt} = \epsilon\Omega\frac{d\nu_1}{d\phi}$. Using $\phi \approx \Omega t$ and $p_1\phi \approx \omega_{n2}t$, we can therefore express $\frac{d\nu}{dt}$ in the time domain as

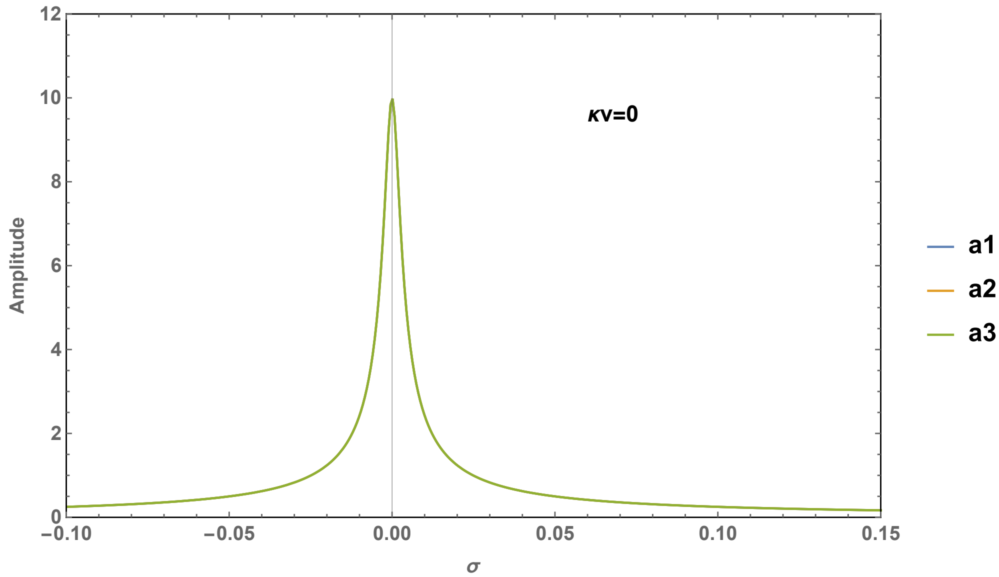

Figure 2.5: Steady state superharmonic resonance response amplitudes versus detuning parameter for $\kappa = 0.1$, $\tilde{e} = 0.2$, $\kappa_v = 0$, $|B| = 1$, $\hat{\zeta} = 0.005$ (a1: first blade, a2: second blade, a3: 3rd blade)

$$\frac{dv}{dt} = \epsilon\Omega\Bigg[\hat{Q}_\phi - \hat{c}_r - \textstyle\sum_{k=1}^{3}\Bigg(\epsilon\hat{d}\cos\Omega t\big[F_{k0} + 2B\sin(\Omega t + \frac{2\pi}{3}k) + a_k\cos(\omega_{n2}t + \beta_k + \frac{4\pi}{3}k)\big]$$
$$-\tilde{e}\big[2B\sin(\Omega t + \tfrac{2\pi}{3}k) + a_k(\tfrac{\omega_{n2}}{\Omega})^2\cos(\omega_{n2}t + \beta_k + \tfrac{4\pi}{3}k)\big]\Bigg)\Bigg] \tag{2.21}$$

Equation (2.21) has $\cos(\Omega t)\sin(\Omega t + \frac{2\pi}{3}k)$, $\cos(\Omega t)\cos(\omega_{n2}t + \beta_k + \frac{4\pi}{3}k)$, $\sin(\Omega t + \frac{2\pi}{3}k)$ and $\cos(\omega_{n2}t + \beta_k + \frac{4\pi}{3}k)$ terms, and therefore the rotor has terms of frequencies Ω, 2Ω, and 3Ω.

The blade response can be approximated in the time domain. Assuming $s_j = s_{j0}$ and plugging Equation (2.12) into the $q_j = \epsilon s_j$, we have

$$q_j = \epsilon(F_{j0} + 2B\sin(\Omega t + \frac{2\pi}{3}j) + a_j\cos(\omega_{n2}t + \beta_j + \frac{4\pi}{3}j)) + O(\epsilon^4). \tag{2.22}$$

2.3.3 Primary Resonance ($\omega_1 \approx 1$ or $\Omega \approx \omega_{n2}$)

$\omega_1 = 1 + \epsilon\sigma$

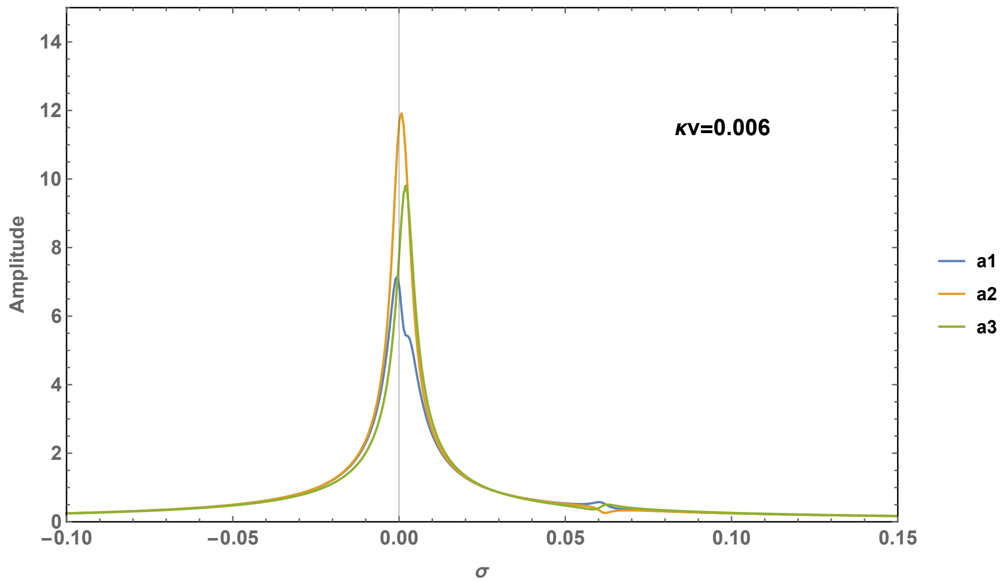

Figure 2.6: Steady state superharmonic resonance response amplitudes versus detuning parameter for $\kappa = 0.1$, $\tilde{e} = 0.2$, $\kappa_v = 0.006$, $|B| = 1$, $\hat{\zeta} = 0.005$ (a1: first blade, a2: second blade, a3: 3rd blade)

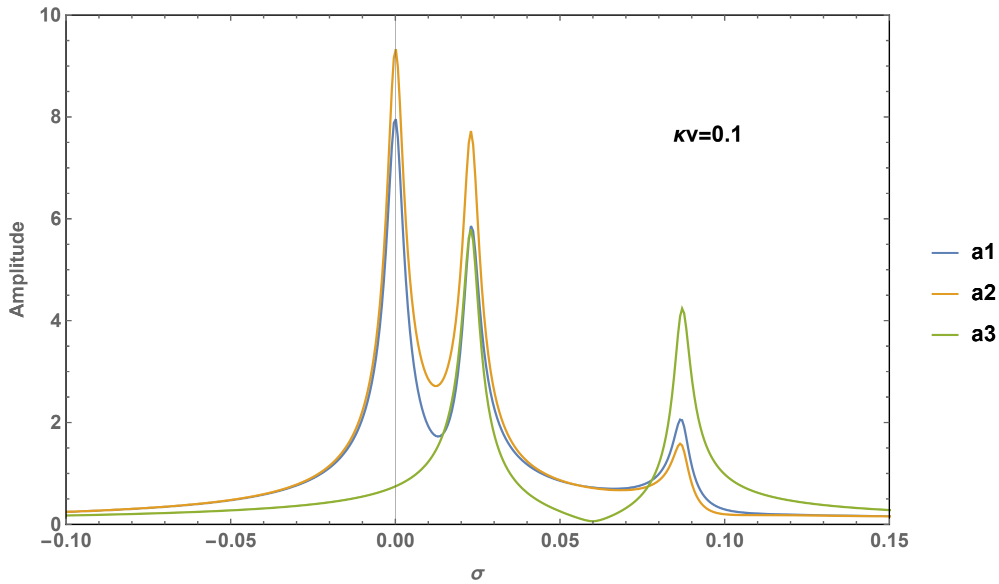

Figure 2.7: Steady state superharmonic resonance response amplitudes versus detuning parameter for $\kappa = 0.1$, $\tilde{e} = 0.2$, $\kappa_v = 0.1$, $|B| = 1$, $\hat{\zeta} = 0.005$ (a1: first blade, a2: second blade, a3: 3rd blade)

Primary resonance is far from the designed operation frequencies of wind turbines, and is not likely to happen unless there is a runaway situation. However, it is of interest to study the dynamical phenomenon. The harmonic forcing is modeled as “weak forcing" in [43] to examine the primary resonance response. Thus we let $\delta = \epsilon\hat{\delta}$. Corresponding to the scaling of δ is the scaling of $\hat{d} = \epsilon\hat{\hat{d}}$

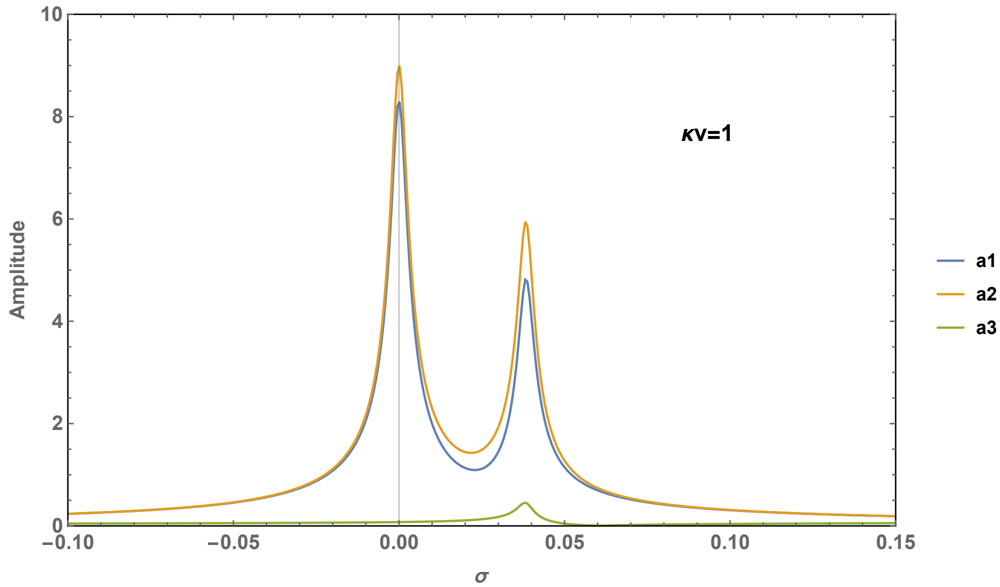

Figure 2.8: Steady state superharmonic resonance response amplitudes versus detuning parameter for $\kappa = 0.1$, $\tilde{e} = 0.2$, $\kappa_v = 1$, $|B| = 1$, $\hat{\zeta} = 0.005$ (a1: first blade, a2: second blade, a3: 3rd blade)

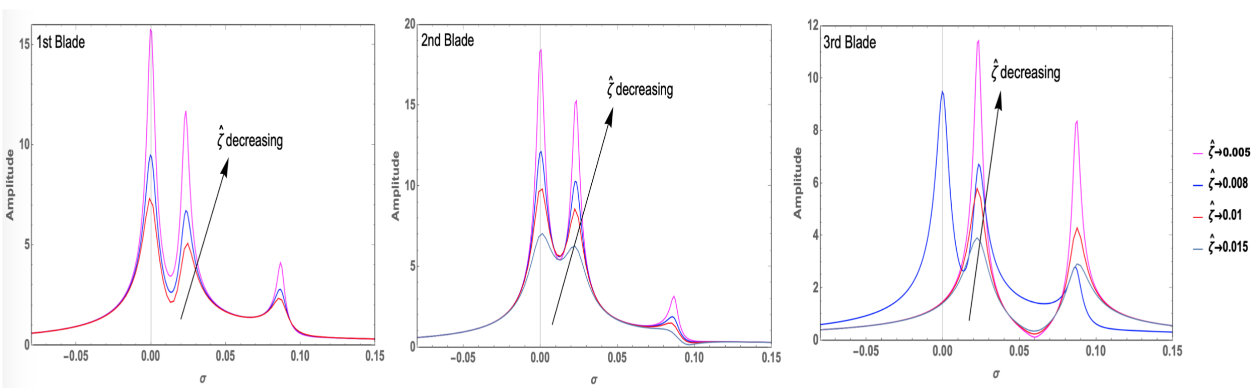

Figure 2.9: Steady-state superharmonic resonance blade response amplitudes versus frequency for $\kappa = 0.1$, $\tilde{e} = 0.2$, $\kappa_v = 0.1$, $|B| = 1$, $\hat{\zeta} = 0.005, 0.008, 0.01, 0.015$

in Equation (2.6).

Plugging expression $\left[\epsilon\hat{\delta}\sin\left(\omega_1\psi_0 + \frac{2\pi}{3}j\right)\right]$ in place of $\left[\delta\sin\left(\omega_1\psi_0 + \frac{2\pi}{3}j\right)\right]$ into the Equation (2.9), we obtain

$$s_{j0} = \frac{F_j}{2} + A_j e^{i\psi_0} + c.c. \tag{2.23}$$

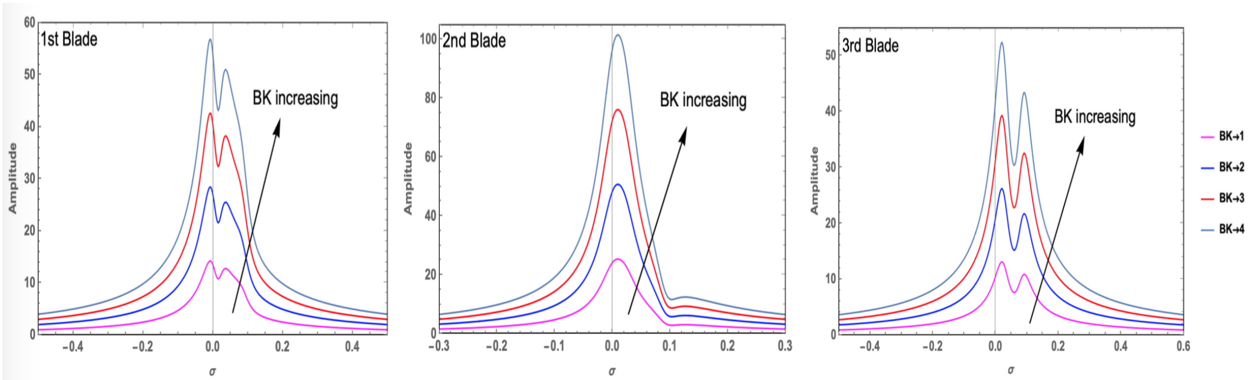

Figure 2.10: Steady-state superharmonic resonance blade response amplitudes versus frequency for $\kappa = 0.1$, $\tilde{e} = 0.2$, $\kappa_v = 0.1$, $|B\kappa| = 1, 2, 3, 4$, $\hat{\zeta} = 0.05$

and

$$2D_0D_1s_{j0} + D_0^2 s_{j1} + s_{j1} = F_{j1}\cos\left(\omega_1\psi_0 + \tfrac{2\pi}{3}j\right) - \hat{\delta}\sin\left(\omega_1\psi_0 + \tfrac{2\pi}{3}j\right) + f - \hat{\zeta}D_0s_{j0} + \kappa_{v_j}s_{j0}$$

$$-\kappa\cos\left(\omega_1\psi_0 + \tfrac{2\pi}{3}j\right)s_{j0} + \tilde{e}^2\textstyle\sum_{k=1}^{3} D_0^2 s_{k0}. \tag{2.24}$$

We equate the coefficients of secular terms to zero and find the solvability condition for $\omega_1 \approx 1$ as

$$-2\mathrm{i}A_j' - \mathrm{i}\hat{\zeta}A_j - \kappa_{v_j}A_j + \left(\mathrm{i}B\kappa_{v_j} + \frac{F_{j1}}{2} - \frac{F_j}{2}\kappa + \mathrm{i}\frac{\hat{\delta}}{2}\right)\mathrm{e}^{\mathrm{i}(\sigma\psi_1 + \frac{2\pi}{3}j)} - \tilde{e}^2\sum_{k=1}^{3}A_k = 0.$$

Plugging $A_j = \Lambda_j \mathrm{e}^{\mathrm{i}(\sigma\psi_1 + \frac{2\pi}{3}j)}$ with $\Lambda_j = X_j + \mathrm{i}Y_j$ into above equation, we then separate real and imaginary parts.

Real part:

$$Y_j' = (-\sigma + \frac{\kappa_{v_j}}{2})X_j - \frac{\hat{\zeta}}{2}Y_j - c_1 + \frac{\tilde{e}^2}{2}\sum_{k=1}^{3}\left[X_k\cos\left(\frac{2\pi}{3}(k-j)\right) - Y_k\sin\left(\frac{2\pi}{3}(k-j)\right)\right], \tag{2.25}$$

Imaginary part:

$$X_j' = (\sigma - \frac{\kappa_{v_j}}{2})Y_j - \frac{\hat{\zeta}}{2}X_j + \frac{\kappa_{v_j}}{2}B + \frac{\hat{\delta}}{4} - \frac{\tilde{e}^2}{2}\sum_{k=1}^{3}\left[X_k\sin\left(\frac{2\pi}{3}(k-j)\right) + Y_k\cos\left(\frac{2\pi}{3}(k-j)\right)\right], \tag{2.26}$$

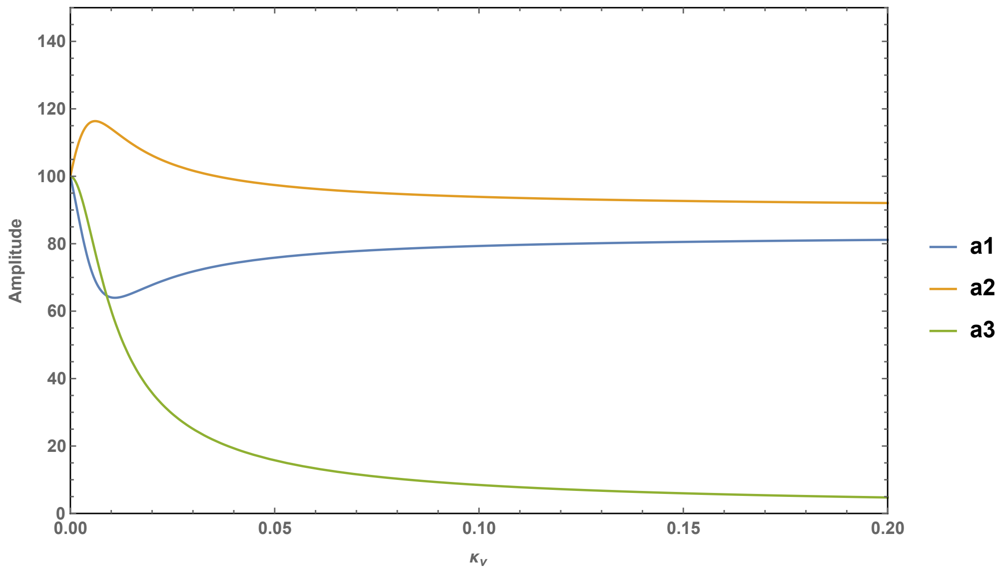

Figure 2.11: Steady state primary resonance response amplitudes versus elastic stiffness mistuning parameter (κ_v) for $\kappa = 0.1$, $\sigma = 0$, $\tilde{e} = 0.2$, $F_{j_0} = 0$, $F_{j_1} = 0.001$, $\hat{\zeta} = 0.005$, $\delta_t = 1$, $|B| = 1$ (a1: first blade, a2: second blade, a3: 3rd blade)

where $c_1 = \dfrac{F_{j1}}{4} - \dfrac{F_j}{4}\kappa$.

Similar to superharmonic resonance case, we have complicated equations for X_j, Y_j and amplitude A_j as functions of all its parameters. The coefficient matrix has the same eigenvalues as the superharmonic case. Figure 2.11 shows a numerical plot of the variation of amplitude with respect to mistuning stiffness parameter. The relation between steady state primary resonance response amplitude and frequency is shown in Figure 2.12 for $\kappa_v = 0.005$ which refers to the peak amplitude value in Figure 2.11. Like the superharmonic case, the primary resonance amplitude of unison responses of the symmetric system matches the value at $\kappa_v = 0$ in Figure 2.11.

Additionally, Figure 2.13 and Figure 2.14 present the changing response amplitude with respect to frequency which is the corresponds to $\kappa_v = 0.1$ and $\kappa_v = 1$. Observed phenomena are very similar to superharmonic case.

We analyze the rotor dynamics by rewriting the solution the in ϕ domain as
$s_j = F_j + 2B\sin(\phi + \dfrac{2\pi}{3}j) + a_j\cos(p_1\phi + \beta_j + \dfrac{4\pi}{3}j)$ and plugged into Equation (2.6), where

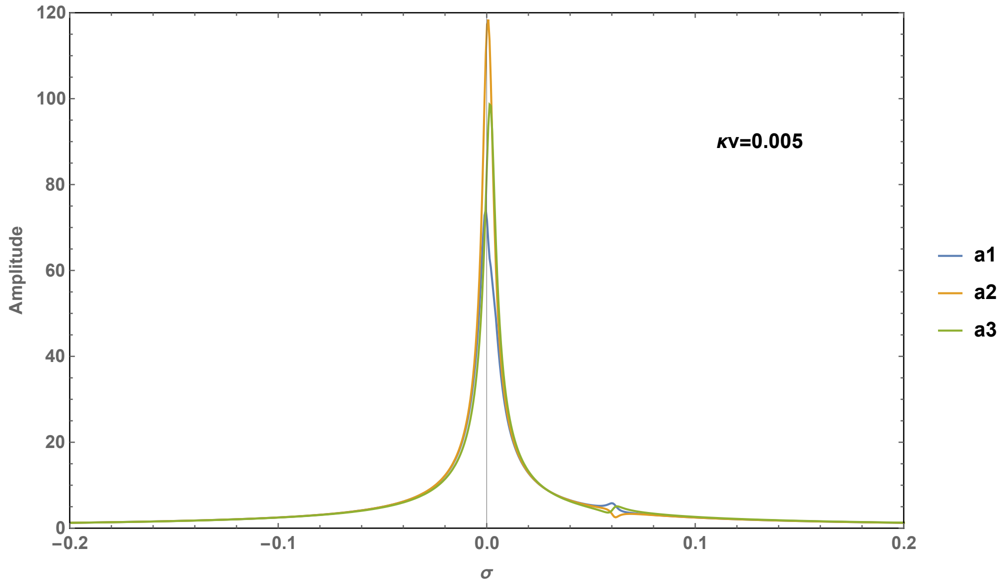

Figure 2.12: Steady state primary resonance response amplitudes versus detuning parameter for $\kappa = 0.1$, $\kappa_v = 0.005$, $\tilde{e} = 0.2$, $F_j = 0$, $F_{j_1} = 0.001$, $\hat{\zeta} = 0.005$, $\delta_t = 1$, $|B| = 1$, (a1: first blade, a2: second blade, a3: 3rd blade)

$a_j = 2\sqrt{X_j^2 + Y_j^2}$ and $\beta_j = \tan^{-1}(\dfrac{Y_j}{X_j})$.

This gives

$$\frac{d\nu_1}{d\phi} = \hat{Q}_\phi - \hat{c}_r - \sum_{k=1}^{3}\Bigg[\epsilon\hat{d}\cos\phi\big[F_{k0} + 2B\sin(\phi + \tfrac{2\pi}{3}k) + a_k\cos(p_1\phi + \beta_k + \tfrac{4\pi}{3}k)\big]$$
$$-\tilde{e}\big[2B\sin(\phi + \tfrac{2\pi}{3}k) + a_k p_1^2\cos(p_1\phi + \beta_k + \tfrac{4\pi}{3}k)\big]\Bigg] \tag{2.27}$$

2.3.4 Subharmonic Resonance ($\omega_1 \approx 2$ or $\Omega \approx 2\omega_{n2}$)

$\omega_1 = 2 + \epsilon\sigma$

Subharmonic resonance is not likely in wind turbines since wind turbines usually perform at low speeds (i. e. $\Omega < \omega_{n2}$).

As we can see from the Campbell diagrams Figure 2.15 and Figure 2.16, depending on parameters, there may or may not be a root at $\Omega/2 = \omega_{n2}$. For dynamical interest, we analyze subharmonic

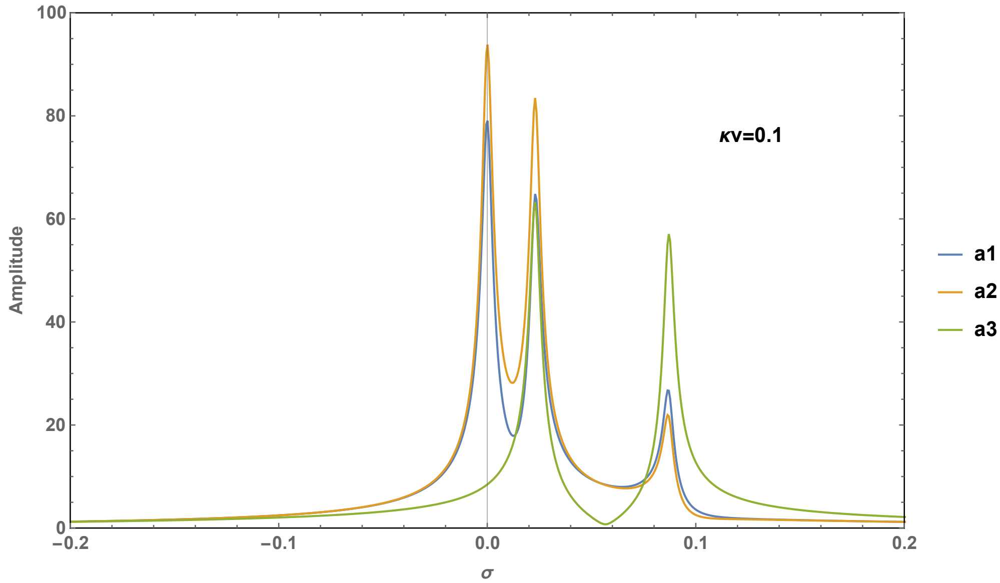

Figure 2.13: Steady state primary resonance response amplitudes versus detuning parameter for $\kappa = 0.1$, $\kappa_v = 0.1$, $\tilde{e} = 0.2$, $F_j = 0$, $F_{j_1} = 0.001$, $\hat{\zeta} = 0.005$, $\delta_t = 1$, $|B| = 1$, (a1: first blade, a2: second blade, a3: 3rd blade)

resonance on a system with parameters that have been adjusted for its existence.

We equate the coefficients of secular terms to zero and find the solvability condition for $\omega_1 \approx 2$ as

$$-2A_j'\mathrm{i} - \mathrm{i}\hat{\zeta}A_j + \kappa_{v_j}A_j - \kappa\frac{\bar{A}_j}{2}e^{\mathrm{i}(\sigma\psi_1 + \frac{2\pi}{3}j)} - \tilde{e}^2\sum_{k=1}^{3}A_k = 0$$

Putting $A_j = \Lambda_j \mathrm{e}^{\mathrm{i}(\frac{\sigma\psi_1}{2} + \frac{\pi}{3}j)}$ with $\Lambda_j = X_j + \mathrm{i}Y_j$ into the above equation, we then divide into separate parts as real and imaginary.

Real part:

$$Y_j' = -\frac{\sigma}{2}X_j - \frac{\hat{\zeta}}{2}Y_j + (\frac{\kappa}{4} - \frac{\kappa_{v_j}}{2})X_j + \frac{\tilde{e}^2}{2}\sum_{k=1}^{3}\left[X_k\cos\left(\frac{\pi}{3}(k-j)\right) - Y_k\sin\left(\frac{\pi}{3}(k-j)\right)\right], \quad (2.28)$$

Imaginary part:

$$X_j' = \frac{\sigma}{2}Y_j - \frac{\hat{\zeta}}{2}X_j + (\frac{\kappa}{4} + \frac{\kappa_{v_j}}{2})Y_j - \frac{\tilde{e}^2}{2}\sum_{k=1}^{3}\left[X_k\sin\left(\frac{\pi}{3}(k-j)\right) + Y_k\cos\left(\frac{\pi}{3}(k-j)\right)\right]. \quad (2.29)$$

Equations (2.28) and (2.29) are autonomous. The solution is $X_j = 0$, $Y_j = 0$ at steady state. Equations (2.28) and (2.29) are linear first-order homogenous differential equations in terms of X_js

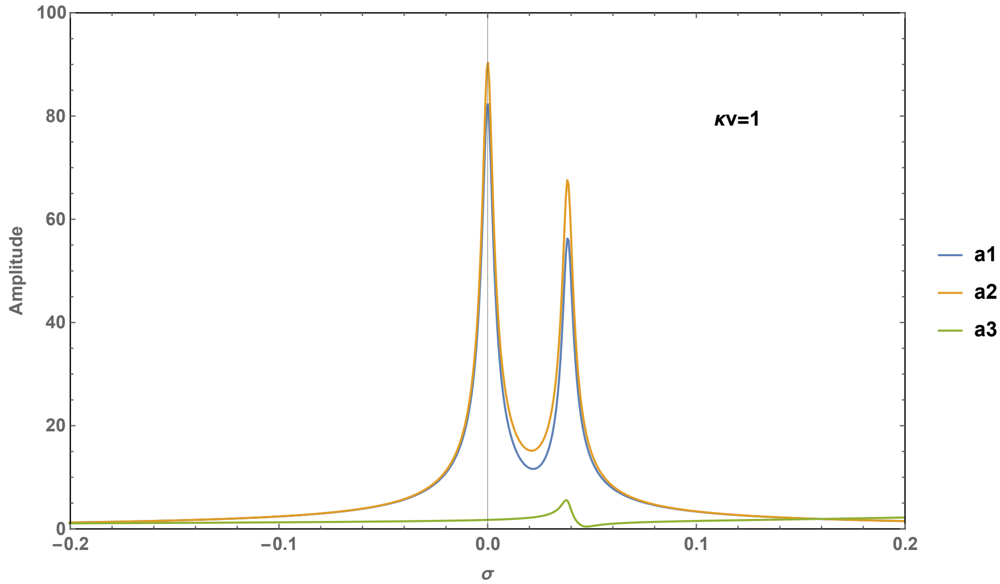

Figure 2.14: Steady state primary resonance response amplitudes versus detuning parameter for $\kappa = 0.1$, $\kappa_v = 1$, $\tilde{e} = 0.2$, $F_j = 0$, $F_{j_1} = 0.001$, $\hat{\zeta} = 0.005$, $\delta_t = 1$, $|B| = 1$, (a1: first blade, a2: second blade, a3: 3rd blade)

and Y_js. We seek an exponential solution with an exponent λ. This leads us to eigenvalue problem where λ_k, $k = 1, ..., 6$ are the eigenvalues. Eigenvalues of the system are complicated. The solution is stable when $Re(\lambda) \leq 0$ for all λ, and unstable when $Re(\lambda) > 0$, for at least one λ. Figure 2.17 shows the relationship between real part of the eigenvalues of steady state system versus elastic stiffness variation κ_v.

Figure 2.18 and Figure 2.19 demonstrate the connection between the frequency and real part of eigenvalues.

2.3.5 Existence of Resonance Conditions

The resonance conditions $\omega_{n2} \approx \Omega/2, \Omega, 2\Omega$, are obtained from Equation (2.13) where $\omega_{n2} = \sqrt{\dfrac{k_0 + k_1\Omega^2}{m_b}}$. The parameters involved in the modal frequency affects the existence of the resonance condition. When $\alpha = 2$ superharmonic, $\alpha = 1$ primary, and $\alpha = \frac{1}{2}$ subharmonic resonances occur with respect to $\omega_{n2} = \alpha\Omega$,

$$\frac{k_0 + k_1\Omega^2}{m_b} = \alpha^2\Omega^2, \tag{2.30}$$

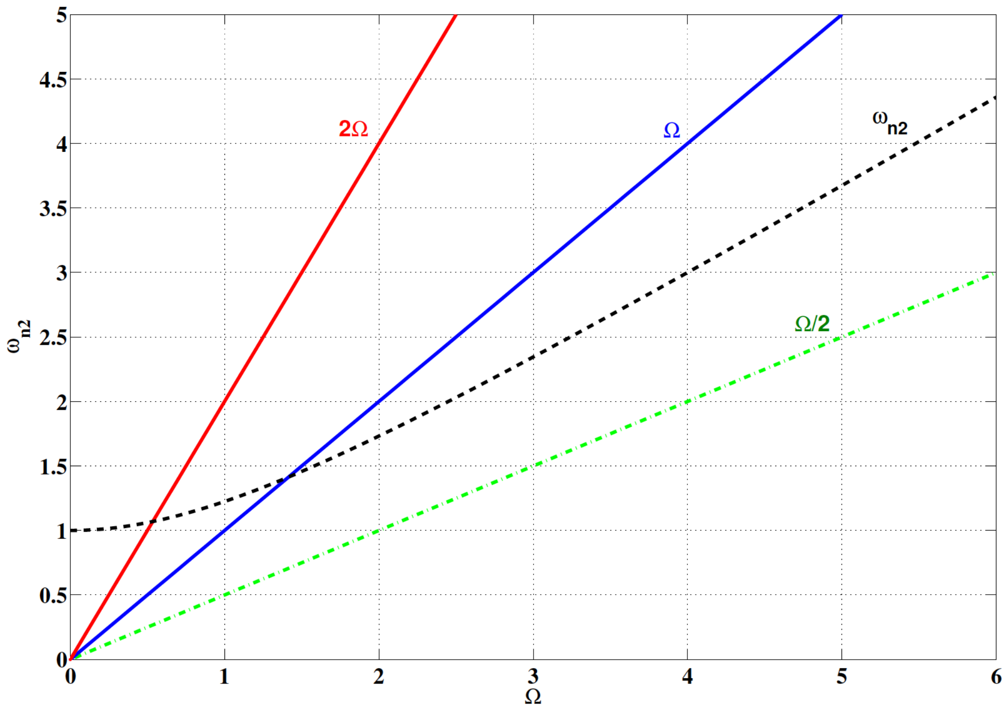

Figure 2.15: Campbell diagram showing ω_{n2} as a function of Ω, for $k_0 = 1$, $k_1 = 0.5$, $m_b = 1$. Intersection with the 2Ω, Ω and $\frac{\Omega}{2}$ lines indicate possible resonances.

which bring out the excitation frequency condition

$$\Omega = \sqrt{\frac{k_0}{m_b\alpha^2 - k_1}}. \tag{2.31}$$

In Figure 2.15, an example Campbell diagram can be seen for specific parameters that were used to find system eigenvalues. It indicates that ω_{n2} as a function of Ω. The intersection points of $\alpha\Omega$ lines and ω_{n2} plot gives us the resonance frequencies. Although primary and superharmonic resonances conditions appear in Figure 2.15, the $\frac{\Omega}{2}$ line does not intersect with the ω_{n2} curve, meaning that basically, the subharmonic resonance will not occur in the system with similar parameter scaling. The systems parameters in time domain were calculated for four different wind turbine models. Turbines structural properties were obtained from the technical report of National Renewable Energy Laboratory [58]. These parameters can be found in Appendix B. Based on the result from the parameters in [58], ω_{n2} versus Ω is nearly flat and so Figure 2.16

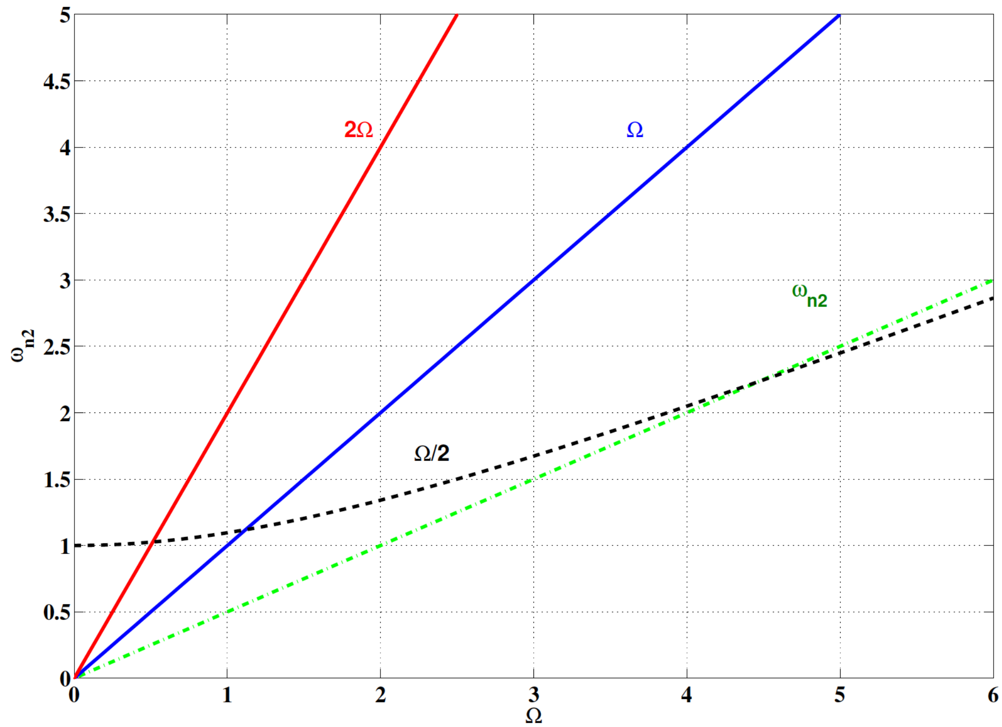

Figure 2.16: Campbell diagram showing ω_{n2} as a function of Ω, for $k_0 = 1$, $k_1 = 0.1$, $m_b = 1$. Intersection with the 2Ω, Ω and $\frac{\Omega}{2}$ lines indicate possible resonances.

qualitatively represents the expected resonance conditions. For the NREL 5MW 64 meter blade, campbell diagram is drawn with parameters $k_0 = 603670$, $k_1 = 4479.3$, $mb = 14441$ as shown in Figure 2.20.

2.4 Numerical Simulation

We would like to perform numerical simulations to validate the analytical results on the superharmonic resonances. The system equations of motion (3.1) and (2.2) in the time domain are simulated with MATLAB's ODE solver "ode45". Then, the fast Fourier transform (FFT) of the sampled analytical solution and the simulation were compared, for q_1, q_2 and q_3, as shown in Figures. 2.22, 2.23 and 2.24 for a specific set of parameters. The constant rotor load, $Q_{\phi 0}$, and rotor damping values, c_r, were chosen to result in a mean rotor speed (Ω) equal to $\omega_{n2}/2$ for the parameter set. A selected value of $Q_{\phi 0}$, given the other parameters, results in a steady-state rotor speed, Ω. The second modal frequency, ω_{n2} depends on Ω via centrifugal stiffening. A

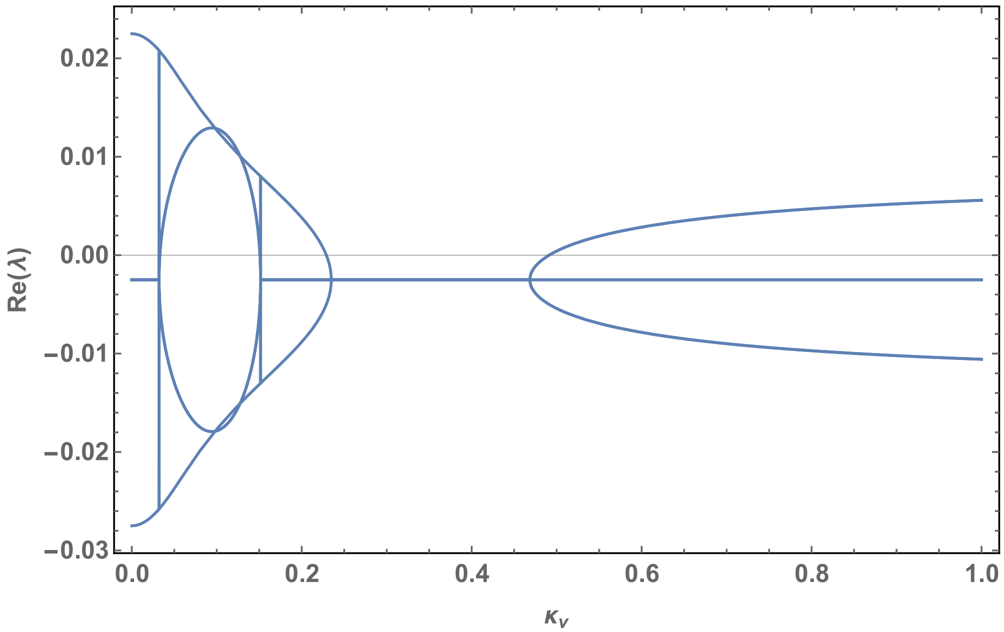

Figure 2.17: Real part of eigenvalues of X and Y equation system versus elastic stiffness mistuning for subharmonic case for $\kappa = 0.1$, $\tilde{e} = 0.2$, $\hat{\zeta} = 0.005$, $\sigma = 0.0005$,

plot of ω_{n2} versus the achieved Ω_{actual} in our simulations is shown in Figure 2.21. There is a gap in the achieved values of Ω_{actual}, to be discussed shortly. As we see from the components of Equation (2.22), vibration amplitudes at frequencies Ω and ω_{n2} predicted by the perturbation analysis can be obtained. Moreover, the expressions of method of multiple scales solutions at the mean speed achieved are evaluated during simulation to compare predicted response amplitudes. When $\Omega_{actual} \approx \omega_{n2}/2$, there is a potential for a superharmonic resonance. The system excitation frequency $\Omega = 1.1225$ rad/sec causes a superharmonic resonance, as shown in Figures 2.22, 2.23 and 2.24 for the first, second and third wind turbine blades respectively for the selected parameters.

The frequency of the simulated rotor acceleration is compared to the analytical solution of Equation (2.21), as shown in Figure 2.25. The analytical rotor solution in Equation (2.21) near superharmonic resonance indicates frequency components of $\Omega, 2\Omega$, and 3Ω. The FFT peaks of the rotor simulation also occur at these frequencies. The analytical solutions show good agreement with the simulations for all three blade and the rotor responses.

If we seek to validate Figures 2.7, 2.9 and 2.10, we would want to aim for desired values in the parameter, $\sigma_{desired}$. In simulation, we achieve a mean speed Ω, from which we obtain the

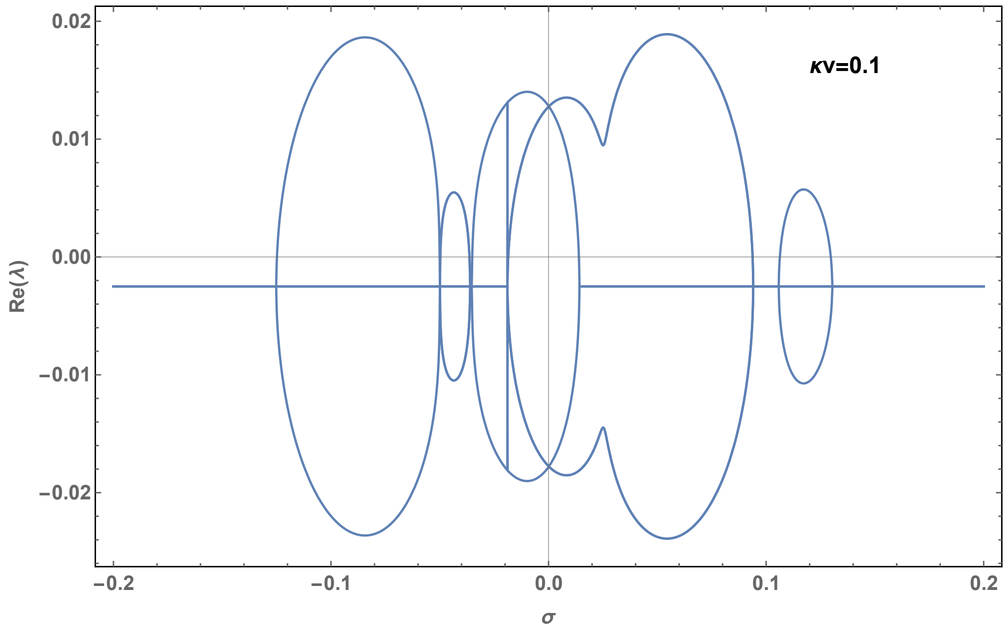

Figure 2.18: Real part of eigenvalues of X and Y equation system versus detuning parameter (rotor frequency) for subharmonic case for $\kappa = 0.1$, $\tilde{e} = 0.2$, $\hat{\zeta} = 0.005$, $\kappa_v = 0.1$,

actual σ. While the rotor load rises, the actual rotor speed increases as well in Figure 2.26 and Figure 2.27. As the rotor force grows, there is an interval in which rotor speed stays the same. This is illustrated in terms of σ and Ω in the figures. This interval is larger in negative mistuning than positive mistuning. At some point, the speed has a sudden jump, then it continues to rise. If the initial condition for the rotor speed is higher than rotor frequency for the superharmonic case, there is no jump. The effect of mistuning on the relationship between the desired detuning parameter $\sigma_{desired}$ and the actual detuning frequency σ_{actual} is shown in Figure 2.28. The initial condition affects also can be seen in Figure 2.29.

While we increase the rotor loading $Q_{\phi 0}$ in Figure 2.30, which uses the rotor initial condition of $\Omega_{supH}/2$, all three blade amplitudes increase until a point. Then, there is a jump in the amplitudes and amplitude values decrease dramatically. This happens as a consequence of the jump phenomena in Figure 2.26 and Figure 2.28 coordinated with the resonance features in Figures 2.7, 2.9, 2.10 and 2.22.

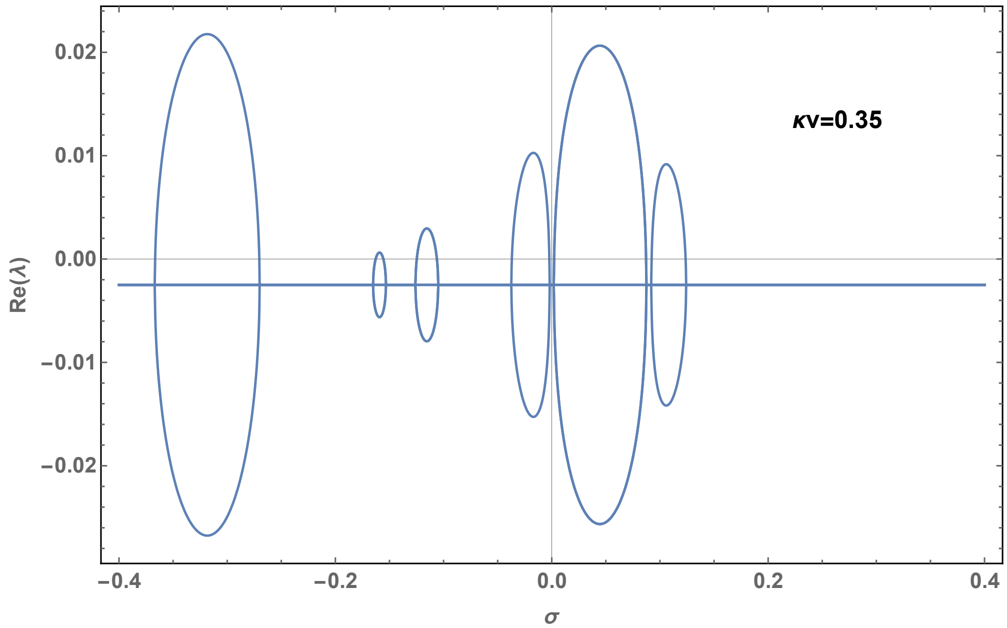

Figure 2.19: Real part of eigenvalues of X and Y equation system versus detuning parameter (rotor frequency) for subharmonic case for $\kappa = 0.1$, $\tilde{e} = 0.2$, $\hat{\zeta} = 0.005$, $\kappa_v = 0.35$,

2.5 Speed Locking Analysis for HAWTs with Tuned Blades

In the previous work, the blade-rotor system with parametric excitation [22, 59, 60] was analyzed by multiple scales method to describe primary and superharmonic resonances. While primary resonance was less relevant to wind turbines, it was noted that the features of both resonances were similar.

In section 2.4 and reference [61], the blade-rotor system equations of motion in the time domain were simulated with MATLAB's ODE solver "ode45" to observe the superharmonic resonances. A speed-locking phenomenon was also observed, in which the superharmonic speed was locked in for an interval of applied mean loads. In the simulations, we achieved a mean speed Ω by setting the mean rotor load. The mean speed increased with increasing rotor load, as shown in Figure (2.26). However, as the rotor moment grew through a range which produced rotor speeds causing a superharmonic resonance in the blades, there was an interval in which rotor speed stayed the same. This interval was larger in the presence of negative or positive mistuning. At a critical point, the speed jumped back to the rising trend. If the initial condition for the rotor speed was

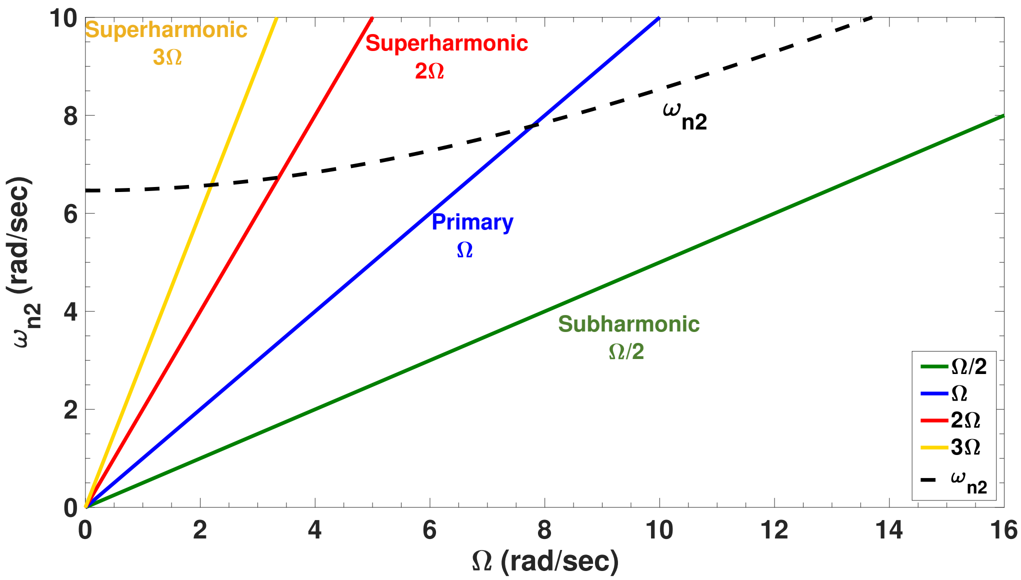

Figure 2.20: Campbell diagram for NREL 5MW 64 meter blade showing ω_{n2} as a function of Ω, with parameters $k_0 = 603670\ N.m$, $k_1 = 4479.3\ kg.m^2$, $mb = 14441\ kg.m^2$. Intersection with the 2Ω, 3Ω, Ω and $\frac{\Omega}{2}$ lines indicate possible resonances at the corresponding Ω.

higher than rotor frequency for the superharmonic case, the jump was greatly reduced.

In this section, we seek to explain the mechanism of this phenomenon on a single blade-rotor system (for which the rotor system is balanced). Although primary resonance is less relevant in the motivational wind-turbine system, it is simpler to analyze, and there is hope that, since the blade resonances are similar to the superharmonic resonances, the primary speed locking might occur with a similar mechanism as the observed superharmonic speed locking. Also, primary resonance provides insight for analyzing the more complicated superharmonic case.

Below, we analyze the speed locking using the harmonic-balance method.

2.5.1 Primary Resonance Case

The approximate (small-deflection) equations of motion of a balanced single blade and rotor system are

$$\ddot{q} + 2\epsilon\mu\dot{q} + ({\omega_n}^2 + \epsilon\gamma\cos\phi)q + \epsilon\hat{d}\sin\phi + \epsilon\tilde{e}\ddot{\phi} \quad = \quad Q \tag{2.32}$$

$$\ddot{\phi} + 2\epsilon\mu_2\dot{\phi} + \epsilon^2\hat{d}\cos\phi q + \epsilon^2 e\ddot{q} \quad = \quad \epsilon Q_\phi \tag{2.33}$$

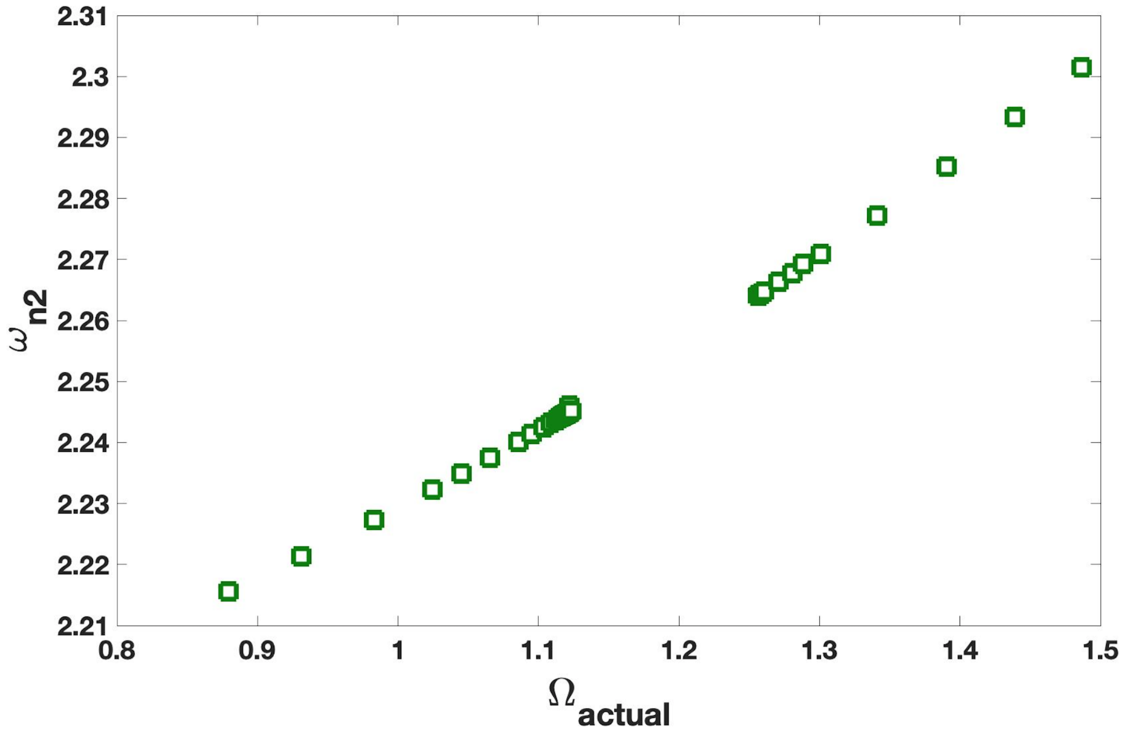

Figure 2.21: ω_{n2} versus Ω_{actual} graph with $IC = 0.5\Omega_{supH}$, $m_b = 1$, $e = 0.2$, $J_r = 10$, $c_b = 0.01$, $c_r = 0.01$, $k_{0_{1,2}} = 4.7$, $k_{0_3} = 4.75$, $d = 0.2$, $k_v = 0.5$, $k_1 = 0.27$, $k_2 = 0.05$

where $\tilde{e} = \epsilon e$. Here, q is the single-mode blade displacement, ϕ is the rotor angle, ω_n is the blade-only modal frequency, ϵ is a small parameter, μ pertains to blade damping, $\epsilon\gamma$ is the strength of parametric excitation (specifically here the ($q \cos \phi$) term), $\epsilon\hat{d}$ is the strength of direct excitation on the blades, and pertains to the parametric excitation of the rotor, μ_2 is the rotor damping, $\tilde{e}$ is an inertial coupling term, and Q and ϵQ_ϕ are the mean loads on the blades and rotor set. Bookkeeping with ϵ is not needed for harmonic balance, ϵ is retained here for insight.

Harmonic balance method will be applied Equation (2.32) and Equation (2.33). We assume a steady-state solution of the form

$$
\begin{aligned}
q &= D + A\cos\Omega t + B\sin\Omega t \\
\phi &= \Omega t
\end{aligned}
\tag{2.34}
$$

After we insert these equations into Equation (2.32) and Equation (2.33) and the constant,

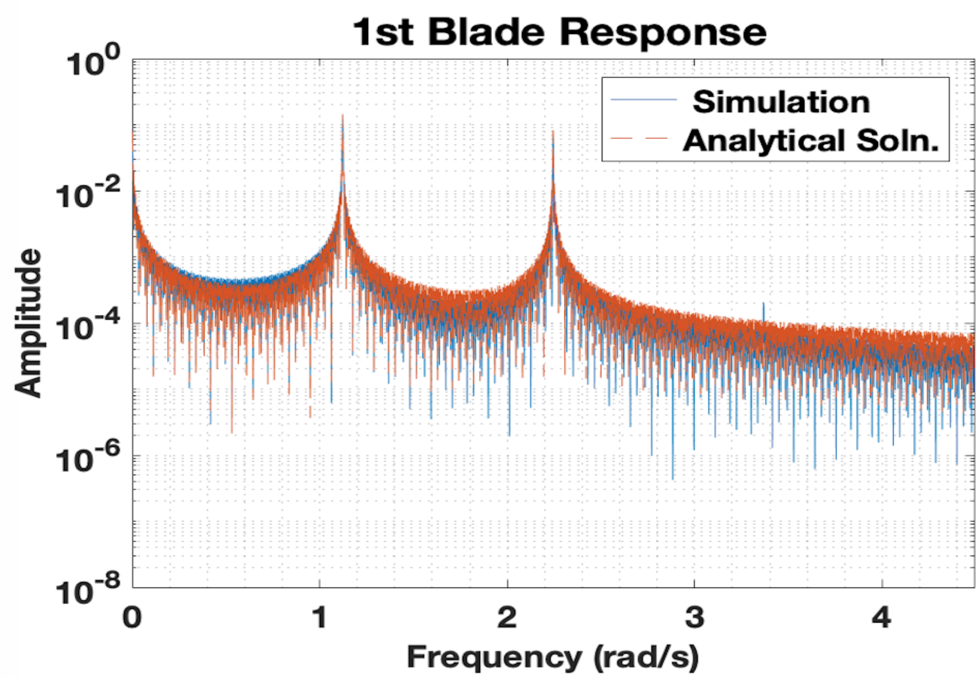

Figure 2.22: FFT plot of q_1 for the analytical solution and simulation for $m_b = 1$, $J_r = 10$, $c_b = 0.01$, $c_r = 0.01$, $k_{0_{1,2}} = 4.7$, $k_{0_3} = 4.75$, $k_v = 0.5$, $k_1 = 0.27$, $k_2 = 0.05$, $d = 0.2$, $e = 0.2$, $Q_{\phi 0} \approx 0.0198$, $\Omega = 1.225$, $\omega_{n2} = 2.2451$

$\cos \Omega t$ and $\sin \Omega t$ terms are balanced to zero. Here are the coefficients from Equation (2.32):

$$\begin{aligned}
Constant: \quad & D{\omega_n}^2 + \epsilon\gamma\frac{A}{2} &=& \quad Q \\
\cos\Omega t: \quad & -A\Omega^2 + 2\epsilon B\Omega + {\omega_n}^2 + \epsilon\gamma D &=& \quad 0 \\
\sin\Omega t: \quad & -B\Omega^2 - 2\epsilon\mu(A\Omega) + {\omega_n}^2 B + \epsilon\hat{d} &=& \quad 0
\end{aligned} \tag{2.35}$$

where we define $\epsilon\gamma \approx \gamma$, $\epsilon\mu \approx \mu$ and $\epsilon\hat{d} \approx d$,

The constant coefficient from Equation (2.33):

$$Constant: \quad 2\epsilon\mu_2\Omega + \epsilon^2\hat{d}\frac{A}{2} = \epsilon Q_\phi \tag{2.36}$$

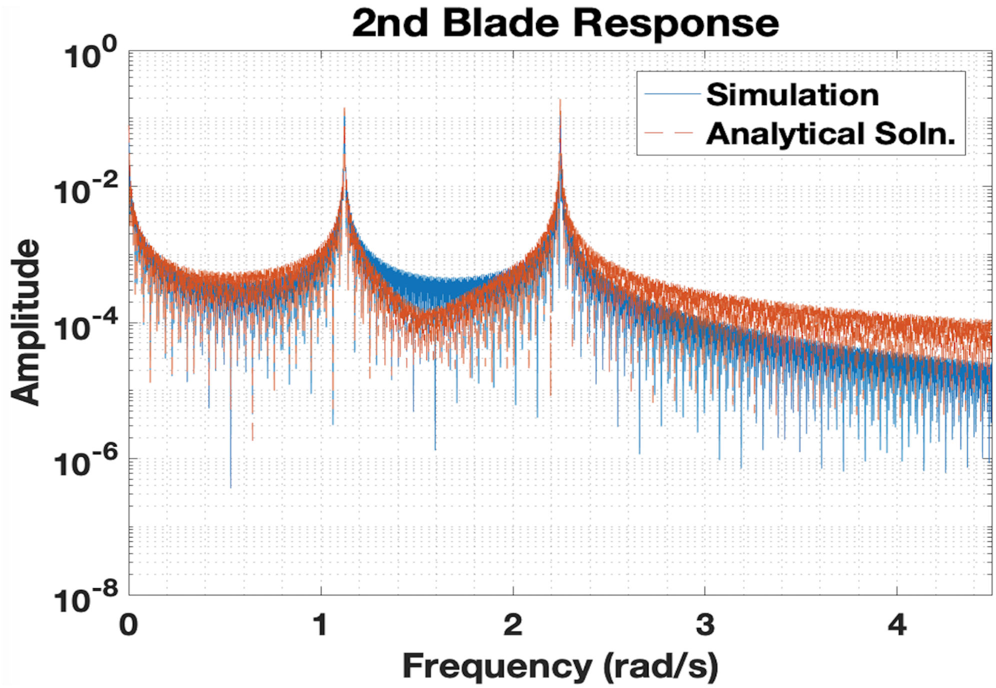

Figure 2.23: FFT plot of q_2 for the analytical solution and simulation for $m_b = 1$, $J_r = 10$, $c_b = 0.01$, $c_r = 0.01$, $k_{0_{1,2}} = 4.7$, $k_{0_3} = 4.75$, $k_v = 0.5$, $k_1 = 0.27$, $k_2 = 0.05$, $d = 0.2$, $e = 0.2$, $Q_{\phi 0} \approx 0.0198$, $\Omega = 1.225$, $\omega_{n2} = 2.2451$

After Equation (2.35) and Equation (2.36) are reorganized, we have

$$D{\omega_n}^2 + \epsilon\gamma\frac{A}{2} = Q \tag{2.37}$$

$$A({\omega_n}^2 - \Omega^2) + 2\mu B\Omega + \gamma D = 0 \tag{2.38}$$

$$-2\mu\Omega A + ({\omega_n}^2 - \Omega^2)B = d \tag{2.39}$$

$$d\frac{A}{2} + 2\mu_2\Omega = Q_\phi \tag{2.40}$$

Equation (2.38) is multipled by A and Equation (2.39) is multiple by B, then they are added up.

$$({\omega_n}^2 - \Omega^2)R^2 + \gamma DA = dB \tag{2.41}$$

where R^2 is defined as $R^2 = (A^2 + B^2)$. Similarly, Equation (2.38) is multiplied by B and Equation (2.39) is multiple by A, then they are subtracted, resulting in

$$2\Omega\mu R^2 + \gamma DB = dA \tag{2.42}$$

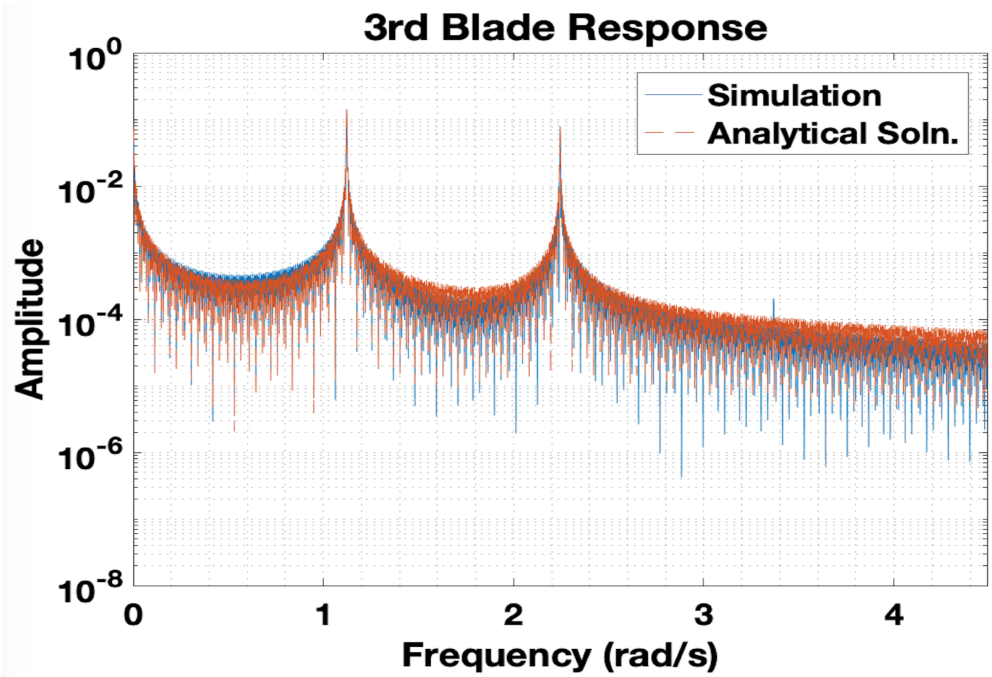

Figure 2.24: FFT plot of q_3 for the analytical solution and simulation for $m_b = 1$, $J_r = 10$, $c_b = 0.01$, $c_r = 0.01$, $k_{0_{1,2}} = 4.7$, $k_{0_3} = 4.75$, $k_v = 0.5$, $k_1 = 0.27$, $k_2 = 0.05$, $d = 0.2$, $e = 0.2$, $Q_{\phi 0} \approx 0.0198$, $\Omega = 1.225$, $\omega_{n2} = 2.2451$

We assumed $D \approx 0$ and Equation (2.41) and Equation (2.42) are solved together to obtain R. Equations are manipulated as Eqn. $(2.41)^2$ + Equation $(2.42)^2$ and R^2 is obtained as

$$R^2((\omega_n^2 - \Omega^2)^2 + (2\mu\Omega)^2) = d^2$$

$$R = \frac{d}{\sqrt{(\omega_n^2 - \Omega^2)^2 + (2\mu\Omega)^2}} \tag{2.43}$$

After Equation (2.40) and Equation (2.42) are combined, we have found

$$-2\mu_2\Omega + Q_\phi = \mu\Omega R^2 \tag{2.44}$$

R is inserted into Equation (2.44), then Q_ϕ is achieved as

$$Q_\phi = 2\mu_2\Omega + \frac{\mu\Omega d^2}{(\omega_n^2 - \Omega^2)^2 - (2\mu\Omega)^2} \tag{2.45}$$

Equation (2.45) is plotted as rotor forcing versus rotor speed and then inverted in Figure 2.31. In

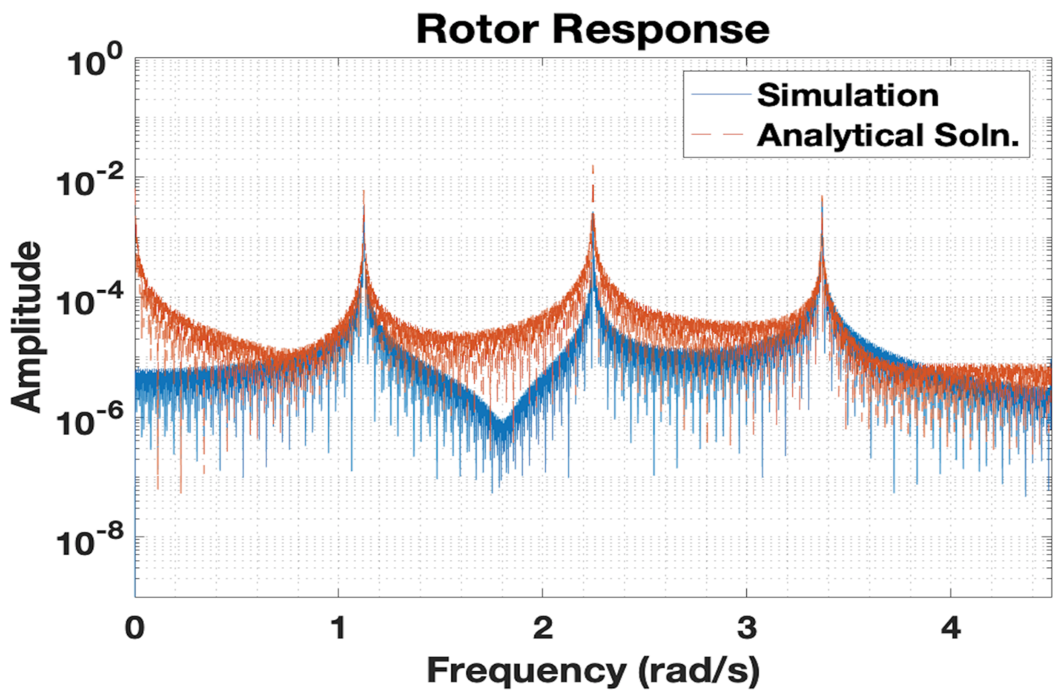

Figure 2.25: FFT plot of $\dot{\phi}$ for the analytical solution and simulation for $m_b = 1$, $J_r = 10$, $c_b = 0.01$, $c_r = 0.01$, $k_{0_{1,2}} = 4.7$, $k_{0_3} = 4.75$, $k_v = 0.5$, $k_1 = 0.27$, $k_2 = 0.05$, $d = 0.2$, $e = 0.2$, $Q_{\phi 0} \approx 0.0198$, $\Omega = 1.225$, $\omega_{n2} = 2.2451$

comparison with Figure 2.26, the speed locking trend can be seen, however greatly exaggerated. We note that it is primary resonance instead of superharmonic resonance.

Referring back to Equations (2.32) and (2.33), it is apparent that the inertial coupling is not needed to produce speed locking, nor are the mean blade load Q and mean blade response D. The rotor parametric term $\epsilon\hat{d}$ and mean rotor load Q_ϕ are important contributors. The parameters in Figure 2.31 are generic, and are meant to show the phenomenon.

2.5.2 Superharmonic Resonance Case at $2\Omega \approx \omega_{n2}$

Secondary resonances show essentially the same speed-locking phenomenon as primary resonance although at a smaller scale, not surprisingly. The equations of motion scaled for secondary resonances are

$$\ddot{q} + 2\epsilon\mu\dot{q} + ({\omega_n}^2 + \epsilon\gamma\cos\phi)q + d\sin\phi + \epsilon\tilde{e}\ddot{\phi} = Q \tag{2.46}$$

$$\ddot{\phi} + 2\epsilon\mu_2\dot{\phi} + \epsilon d\cos\phi q + \epsilon^2 e\ddot{q} = \epsilon Q_\phi \tag{2.47}$$

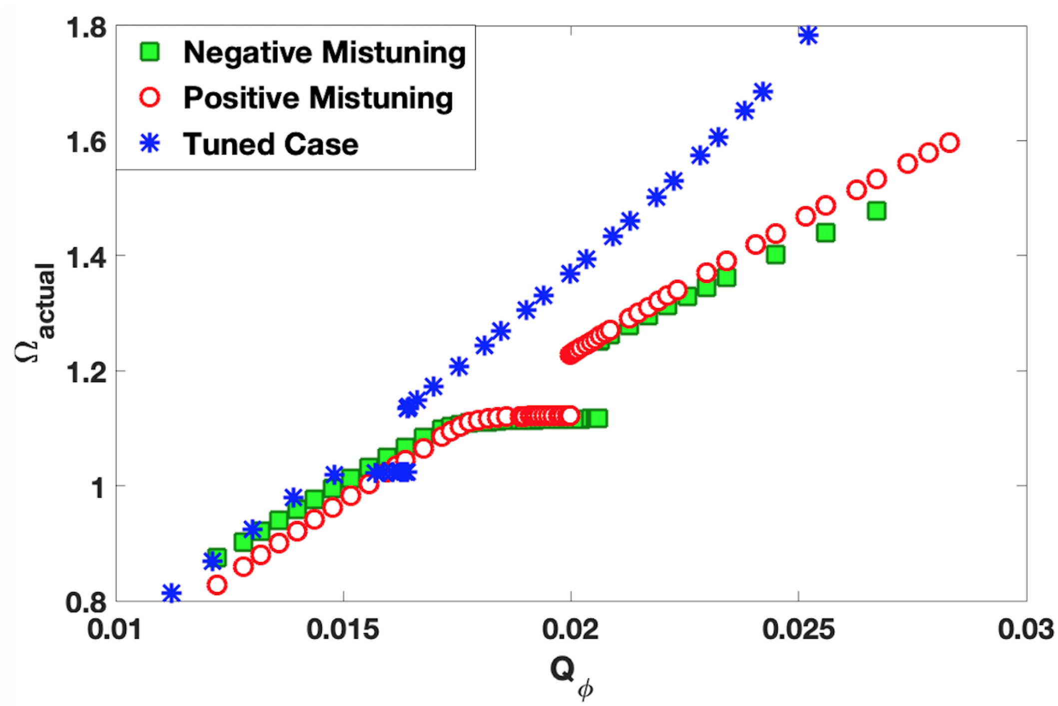

Figure 2.26: Ω_{actual} versus Q_ϕ Graph with negative and positive mistuning cases and tuned case for $m_b = 1$, $J_r = 10$, $c_b = 0.01$, $c_r = 0.01$, $k_{0_{1,2}} = 4.7$, $k_{0_3} = 4.75$, $k_v = 0.5$, $k_1 = 0.27$, $k_2 = 0.05$, $d = 0.2$, $e = 0.2$

The harmonic-balance method is applied to Equations (2.46) and (2.47). For superharmonic responses, we assume

$$\begin{aligned} q &= D + A\cos 2\Omega t + B\sin 2\Omega t + C\cos\Omega t + E\sin\Omega t \\ \phi &= \Omega t + f\cos\Omega t + g\sin\Omega t \end{aligned} \tag{2.48}$$

Calculations away from primary resonance show that C is smaller than E. We assume that C, D and Q are negligible in Equations (2.46) and (2.47), and treat f and g as small.

After we insert Equation (2.48) into Equation (2.46) and Equation (2.47), we have balanced the constant, $\sin\Omega t$, $\cos\Omega t$ $\cos 2\Omega t$, $\sin 2\Omega t$ terms to zero. After many manipulations of the balance equations, finally we found superharmonic resonance amplitude at order two, where $2\Omega \approx \omega_n$, is

$$R_2^2 = \frac{(\epsilon\gamma)^2(\frac{4d}{3\omega_n{}^2})^2}{4[((\omega_n{}^2 - 4\Omega^2) + \frac{1}{2}\epsilon g\gamma\Omega)^2 + (4\mu\epsilon\Omega)^2] - 4(\frac{d^2\Omega\epsilon}{\omega_n{}^2})^2} \tag{2.49}$$

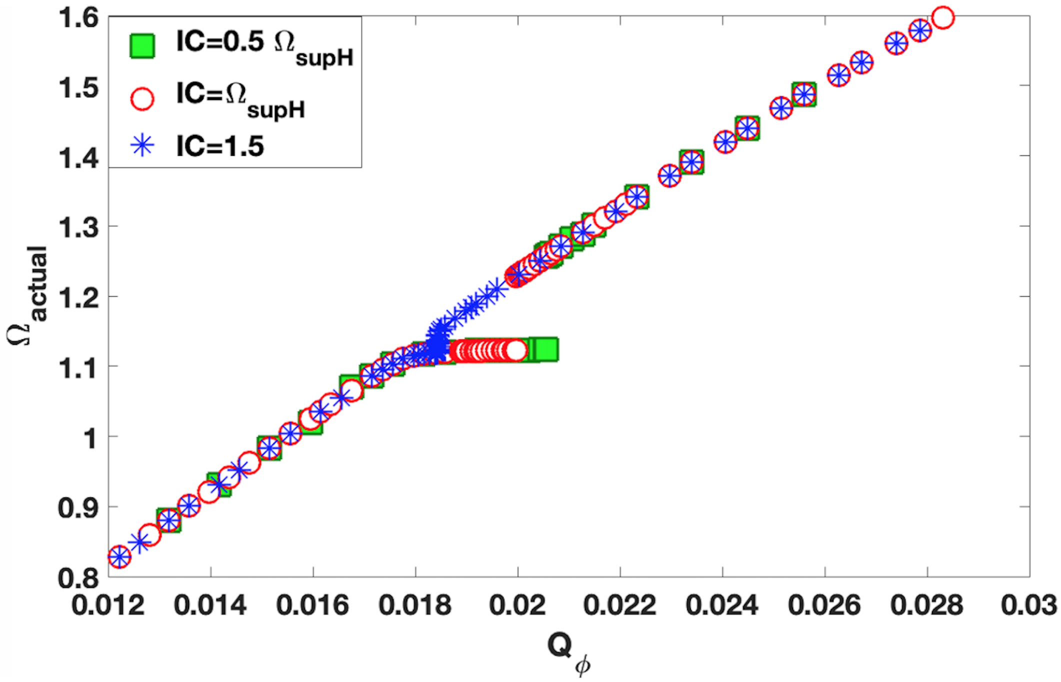

Figure 2.27: Ω_{actual} versus Q_ϕ graph for different initial condition for $m_b = 1$, $J_r = 10$, $c_b = 0.01$, $c_r = 0.01$, $k_{0_{1,2}} = 4.7$, $k_{0_3} = 4.75$, $k_v = 0.5$, $k_1 = 0.27$, $k_2 = 0.05$, $d = 0.2$, $e = 0.2$

where $R_2^2 = A^2 + B^2$.

By using Equation (2.49), and the constant balance from Equation (2.47), we have found the rotor force equation as

$$Q_\phi = 2\mu_2\Omega + \frac{2\mu_2(\epsilon d)^2\Omega^2 R_2^2}{\Gamma} \tag{2.50}$$

where $\Gamma = 4[\Omega^4 + (2\epsilon\mu_2\Omega)^2]$. Notice that R_2^2 shows a resonance peak at the superharmonic frequency, $2\Omega \approx \omega_n$, but scaled by ϵ^2, and thus Q_ϕ should have a small peak when plotted versus Ω. Inverting this plot suggests a possible Q_ϕ interval of speed locking.

We found the peak value of forcing level at $\Omega \approx \omega_{peak}$ where

$((\omega_n^2 - 4\Omega^2) + \frac{1}{2}\epsilon g\gamma\Omega)^2 = 0$ as

$$Q_{\phi_{peak}} = 2\mu_2\Omega + \frac{8\mu_2\epsilon^2(\frac{d^2\gamma}{3\omega_n})^2}{(4\mu)^4\epsilon^2\Omega^2 + (\epsilon\frac{d^2}{\omega_n})^2} \tag{2.51}$$

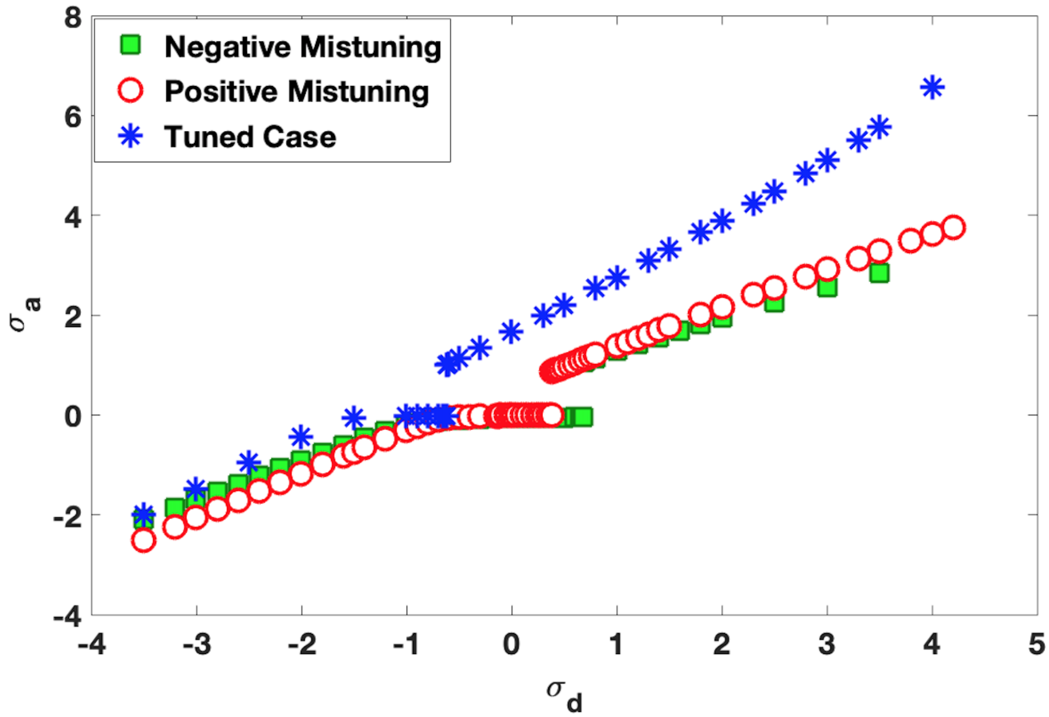

Figure 2.28: $\sigma_{desired}$ versus σ_{actual} with negative and positive mistuning cases and tuned case for $m_b = 1$, $J_r = 10$, $c_b = 0.01$, $c_r = 0.01$, $k_{0_{1,2}} = 4.7$, $k_{0_3} = 4.75$, $k_v = 0.5$, $k_1 = 0.27$, $k_2 = 0.05$, $d = 0.2$, $e = 0.2$

Similarly, in Figure 2.32 the speed locking trend can be seen with superharmonic case at order two in comparison with Figure 2.26. The parameters that used to create Figure 2.32 are generic to show the speed locking phenomenon.

2.6 Conclusions

In-plane vibrations of a mistuned three-blade wind turbine were studied. By using a simplified model, in-plane vibrations were taken into consideration. The blades and rotor equations were written in the ϕ domain to decouple the blade equations from the rotor equation.

After decoupling, the differential blade equations contained parametric and direct excitation. We looked at resonances due to cyclic gravitational and aerodynamic loading. It was observed that slight mistuning in a single blade could cause the single resonance peak of the tuned case to split into two or three resonance peaks, in both the superharmonic and primary resonances and

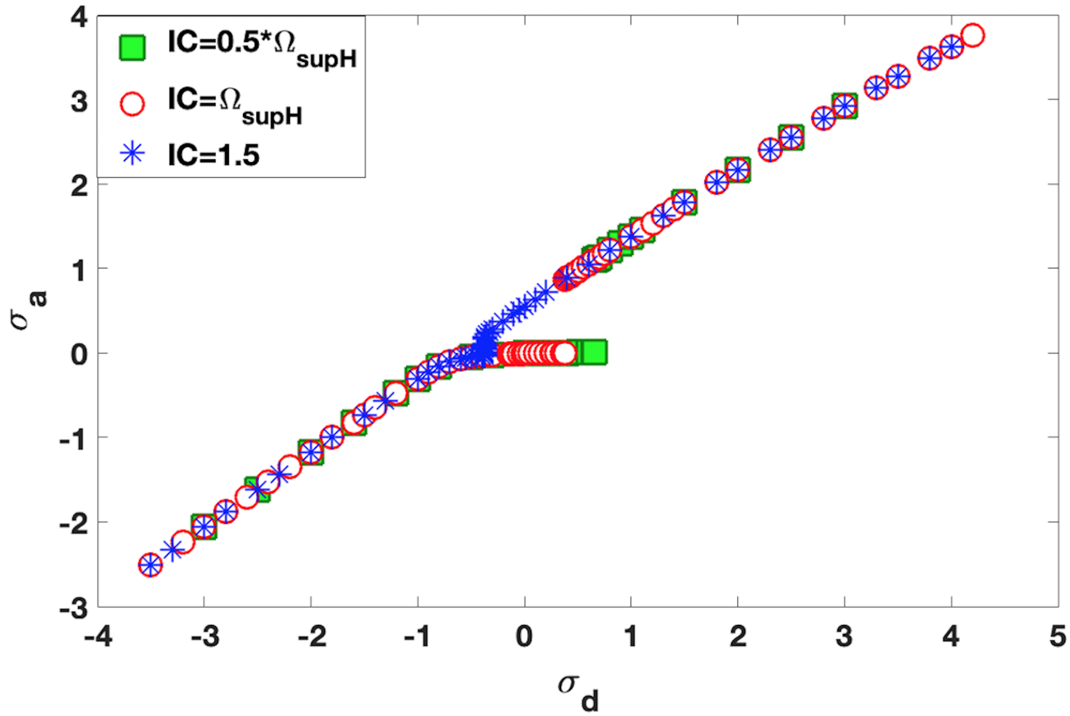

Figure 2.29: $\sigma_{desired}$ versus σ_{actual} graph for different initial condition for $m_b = 1$, $J_r = 10$, $c_b = 0.01$, $c_r = 0.01$, $k_{0_{1,2}} = 4.7$, $k_{0_3} = 4.75$, $k_v = 0.5$, $k_1 = 0.27$, $k_2 = 0.05$, $d = 0.2$, $e = 0.2$

the blades take on different steady state amplitudes. The resonant amplitude of at least one of the blades is larger than in the perfectly tuned case. On the other hand, subharmonic resonance will not occur in a rotating system with similar parameter scaling. Subharmonic resonances may or may not be possible in this dynamical system, depending on parameters, and at rotor speeds well outside the expected operating conditions of wind turbines. Subharmonic resonances involve instabilities similar to those of the Mathieu equation, but more complicated.

Specifically, superharmonic resonances is focused on, since they are more likely to be problematic in the low-frequency operating ranges of wind turbines. The effects of parameters on the superharmonic resonances are examined, and a numerical study is conducted aimed at verifying the analytical results. We also looked at the rotor dynamics during resonance.

At the superharmonic resonant frequency, positive mistuning leads to an increased resonant amplitude of one of the blades. However, very slight negative mistuning can lead to a slight amplitude increase in two of the blades, while more negative mistunings lead to a decreased

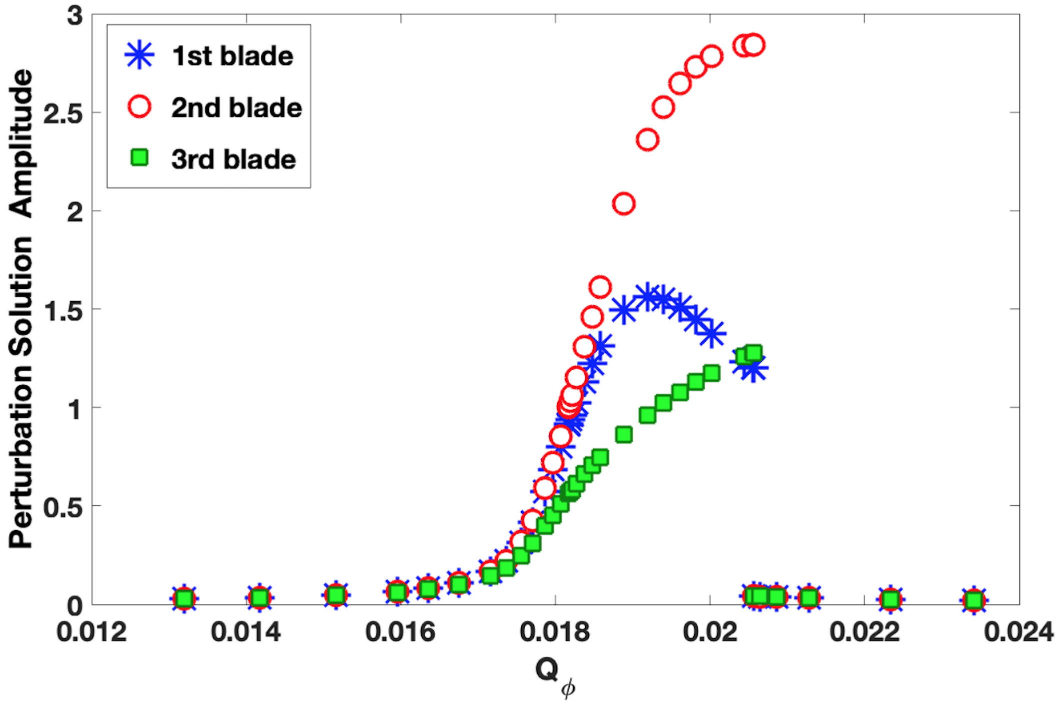

Figure 2.30: Q_ϕ versus perturbation solution amplitude graph for $m_b = 1$, $J_r = 10$, $c_b = 0.01$, $c_r = 0.01$, $k_{0_{1,2}} = 4.7$, $k_{0_3} = 4.75$, $k_v = 0.5$, $k_1 = 0.27$, $k_2 = 0.05$, $d = 0.2$, $e = 0.2$

amplitude in two of the blades. The effect of damping is similar to that of linear oscillators, in which the resonances peaks sharpen with decreased damping. Increased damping was observed to quench one of the three superharmonic peaks in the mistuned blade. Increasing the forcing level increases the resonance profile uniformly.

The FFTs of numerical simulations of blades at a fixed set of parameters in superharmonic resonance agreed very well with those of the sampled analytical responses. The rotor dynamics were also expressed analytically. In the superharmonic resonance, the analytical rotor response was shown to have three frequencies, Ω, 2Ω, and 3Ω, due to nonlinear effects. The numerical solutions captured these three frequency components and each agreed very well in amplitude.

We aimed to numerically confirm the blade response amplitudes at various rotor speeds near resonance. The rotor speed is determined by the input load to the rotor. Simulations showed that the mean rotor speed can lock into the superharmonic speed over a range of mean rotor loads, and, with further increase of the rotor load, experience a jump out of the superharmonic speed. Thus, it

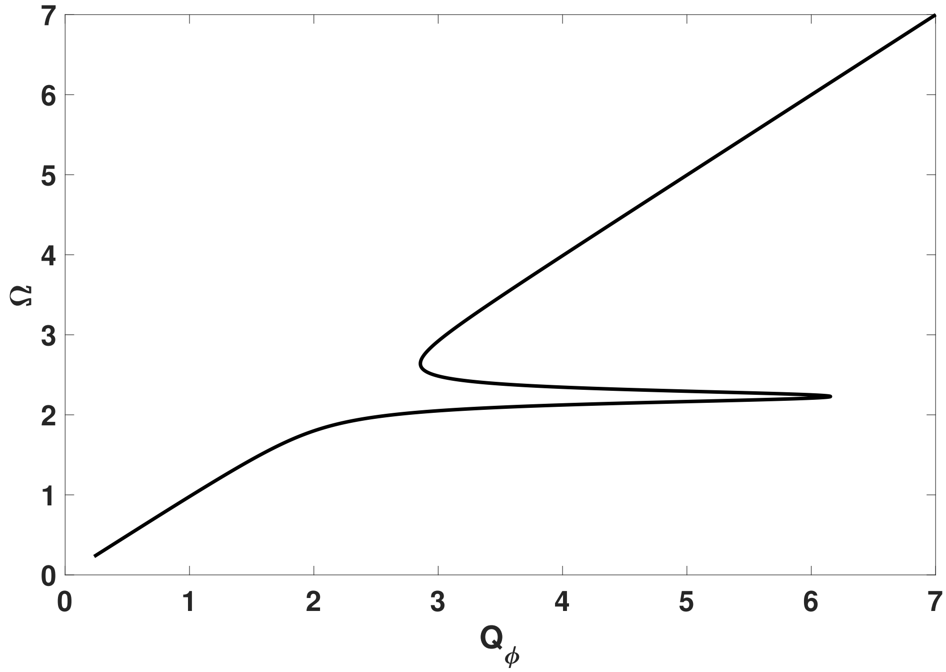

Figure 2.31: Speed-locking graph Ω versus Q_ϕ for primary resonance for $\mu = 0.1, \mu_2 = 0.5, \omega_{n2} = 2.23, d = 1.871$

is possible that some detuning parameters in Figures 2.7, 2.9 and 2.10 cannot be achieved, as well as resonant blade responses in such ranges of detuning parameters. We investigated the effects of mistuning level and initial conditions on the relationship between the rotor load and mean speed. In addition, we looked into the relationship between rotor load and the blade amplitudes. We observed all three blade amplitudes jumped down suddenly at a certain value of the increasing rotor load.

Lastly, our purpose was to analytically confirm the blade response amplitudes at various rotor speeds near resonance and verify speed locking phenomenon. We found that speed-locking is due to the average interaction between the blade vibration and rotor motion in the rotor equation, and its balance against the mean rotor moment. The phenomenon was examined for an effective (balanced) single blade-rotor system by applying harmonic balance method.

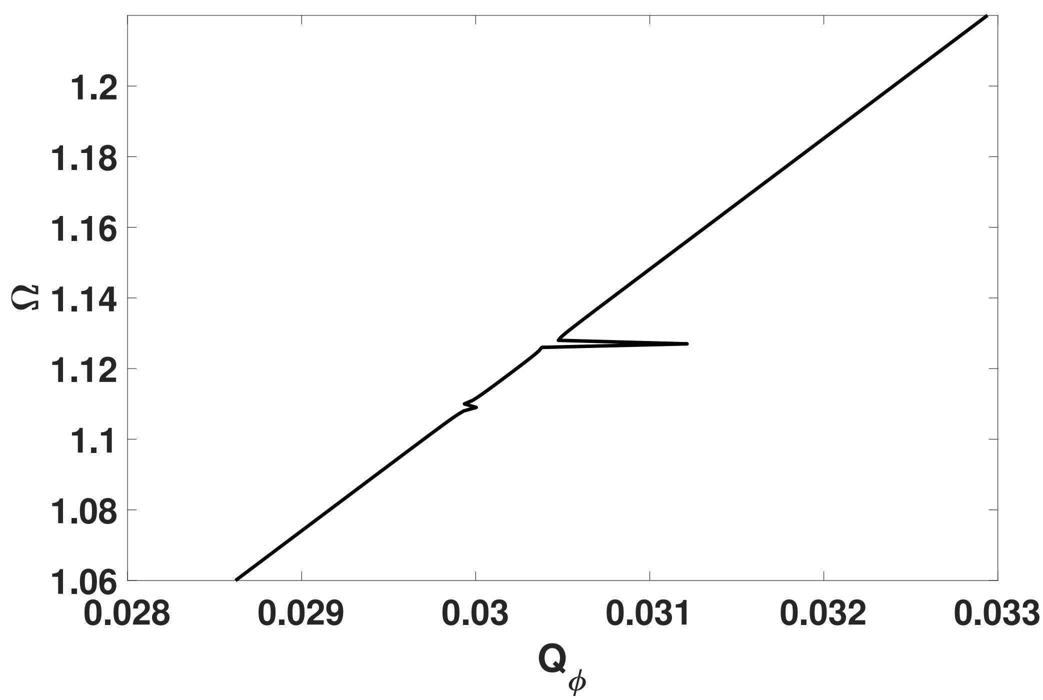

Figure 2.32: Speed-locking graph Ω versus Q_ϕ for superharmonic resonance order two for $g = 1, \mu = 0.01, \mu_2 = 0.0135, \omega_{n2} = 2.23, d = 1.871, \gamma = 0.5$

CHAPTER 3

SECOND-ORDER PERTURBATION ANALYSIS OF IN-PLANE BLADE-HUB DYNAMICS OF HORIZONTAL-AXIS WIND TURBINES

3.1 Introduction

This work takes interest in the coupled blade-rotor dynamics with and without mistuning. More general mistuned rotational systems have been analyzed by many researchers [47–50]. The effects of mistuning on the turbine blades with mechanical coupling was analyzed by Whitehead [51]. Ewins [52] and Cha and Sinha [53] worked on broken symmetry in bladed disk. Also, the effects of mistuning on four-degree-of-freedom systems with parametric stiffness was studied [55]. Mistuning on Sinha and Griffin [45] and Dick *et al.* [46] worked on nonlinearity in rotors to show the deviation from the symmetric response. The wind-turbine rotor-blades system with tuned [43] and weakly mistuned blades [60] were analyzed to find steady state dynamics by using a first-order perturbation method. The analysis showed that direct and parametric excitation combine to cause a superharmonic resonance at half the first modal frequency, a primary resonance, and subharmonic resonance at twice the natural frequency of the system. In the tuned case, each blade had the same amplitude because the system was symmetric and linear, while in the mistuned case vibration localization could occur.

In this study, we apply a second-order method of multiple scales to the equations of motion for in-plane tuned and weakly mistuned blades of horizontal axis wind turbine to determine the steady state dynamics, with focus on the superharmonic resonance of order three for the linear system with hard forcing.

3.2 Three Blade Turbine Equations

In this chapter, we analyze blades Equation (2.1) and rotor Equation (2.2) as studied in Section 2.2. Rewritting the rotor and j^{th} blade linearized equations of motion in the time domain for

$j = 1, 2$ and 3:

$$m_b\ddot{q}_j + c_b\dot{q}_j + (k_{0_j} + k_1\dot{\phi}^2 + k_2\cos\phi_j)q_j + d\sin\phi_j + e\ddot{\phi} = Q_j, \tag{3.1}$$

$$J_r\ddot{\phi} + c_r\dot{\phi} + \sum_{k=1}^{3}(d\cos\phi_k q_k + e\ddot{q}_k) = Q_\phi, \tag{3.2}$$

where $k_{0_1} = k_{0_2} = k_0$, $k_{0_3} = k_0 + \epsilon k_v$ where k_0 is blade's modal elastic stiffness, ϵ is a small parameter and k_v is the elastic stiffness variation of the mistuned blade, m_b is the inertia of a single blade, J_r is the total inertia of blade-hub system, e is the coupling term, q_j is the assumed modal coordinate for j^{th} blade, ϕ is the rotor angle, $\phi_j = \phi + \frac{2\pi}{3}j$ is the blade angle, k_1 and k_2 are stiffness contributions of centrifugal and gravitational effects, respectively, Q_j and Q_ϕ are generalized forcing terms due to aeroealstic loading and c_b and c_r are generic damping coefficients [60]. Definitions of these parameters can be found in the Appendix A.1. Tower motion is neglected and only in-plane vibration is taken into consideration by using simplified model as shown in Figure 2.1. For the zero gravity system, Figure 3.1 shows the how natural frequencies change with respect to mistuning stiffness parameter. In the symmetric case, $k_v = 0$, the second and third natural frequencies are equal, $\omega_{n3} = \omega_{n2}$.

Following [60] as in Chapter 2, the indepedent variable time was changed to rotor angle ϕ and Equations (3.1) and (3.2) are transformed to a new form

$$\nu^2 q_j'' + \nu\nu' q_j' + \tilde{c}_b\nu q_j' + (\tilde{k}_{0_j} + \tilde{k}_1\nu^2 + \tilde{k}_2\cos\phi_j)q_j + \tilde{d}\sin\phi_j + \tilde{e}\nu\nu' = \tilde{Q}_j, \tag{3.3}$$

$$\nu\nu' + \tilde{c}_r\nu + \chi\sum_{k=1}^{3}\left[\tilde{d}\cos\phi_k q_k + \tilde{e}(\nu^2 q_k'' + \nu\nu' q_k')\right] = \tilde{Q}_\phi, \tag{3.4}$$

where $()' = \dfrac{d()}{d\phi}$, and $\tilde{k}_{0_1} = \tilde{k}_{0_2} = \tilde{k}_0$ and $\tilde{k}_{0_3} = \tilde{k}_0 + \epsilon\tilde{k}_v$ and where $\tilde{c}_b = \frac{c_b}{m_b\Omega}$, $\tilde{k}_0 = \dfrac{k_0}{m_b\Omega^2}$,

$\tilde{k}_v = \frac{k_v}{m_b\Omega^2}$, $\tilde{k}_1 = \frac{k_1}{m_b}$, $\tilde{k}_2 = \frac{k_2}{m_b\Omega^2}$, $\tilde{d} = \frac{d}{m_b\Omega^2}$, $\chi = \frac{m_b}{J_r}$, $\tilde{Q}_j = \frac{Q_j}{m_b\Omega^2}$, $\tilde{e} = \frac{e}{m_b}$,

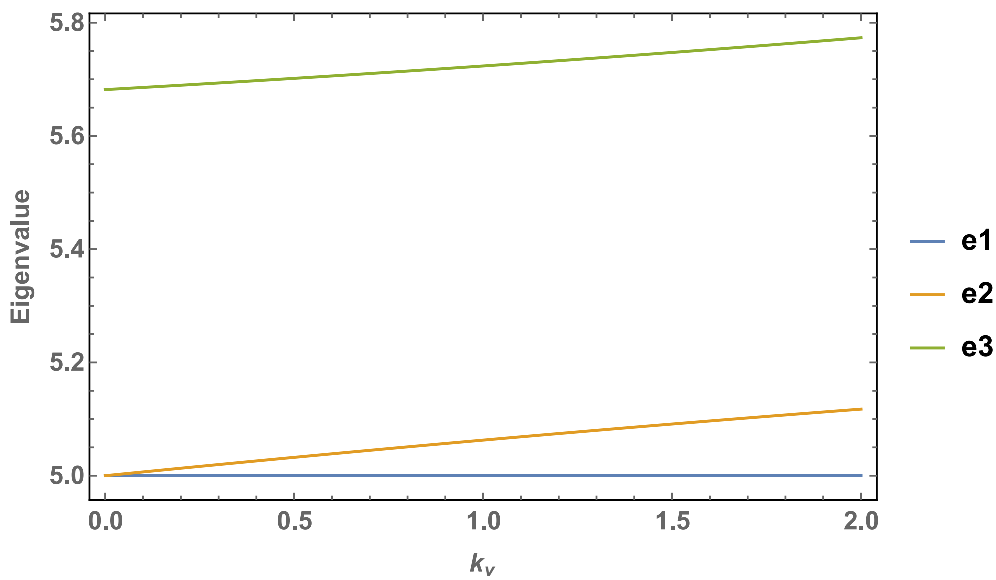

Figure 3.1: Eigenvalues versus elastic stiffness mistuning parameter (k_v) plot for $k_0 = 5$, $k_1 = 0.5$, $\dot{\Phi} = 0$, $m = 1$, $J = 1$, $e = 0.2$, $\epsilon = 0.1$ (e1: first blade, e2: second blade, e3: third blade)

$\tilde{c}_r = \frac{c_r}{J_r \Omega}$, $\quad \tilde{Q}_\phi = \frac{Q_\phi}{J_r \Omega^2}$

The small parameter was defined as $\epsilon = m_b/J_r$ since J_r is much larger than m_b. To decouple the rotor equation from the leading-order blade equations, a nondimensionalization was applied and new scaling was done on Equations (3.3) and (3.4):

$\nu = 1 + \epsilon^2 \nu_1$, $\quad \tilde{c}_b = \epsilon \hat{c}_b$, $\quad \tilde{k}_2 = \epsilon \hat{k}_2$, $\quad \tilde{d} = \epsilon \hat{d}$, $\quad \tilde{c}_r = \epsilon^2 \hat{c}_r, \chi = \epsilon$, $\quad q_j = \epsilon s_j$, $\quad \tilde{Q}_j = \epsilon \hat{Q}_j$, $\tilde{Q}_\phi = \epsilon^2 \hat{Q}_\phi$.

The equations are rewritten in terms of new scaled blade coordinates s_j and hub coordinate ν_1 as

$$s_j'' + \epsilon \hat{c}_b s_j' + (\tilde{k}_{0_j} + \tilde{k}_1 + \epsilon \hat{k}_2 \cos \phi_j) s_j + \hat{d} \sin \phi_j + \epsilon \tilde{e} \nu_1' = \hat{Q}_j + H.O.T., \tag{3.5}$$

$$\nu_1' + \hat{c}_r + \sum_{k=1}^{3} (\epsilon \hat{d} \cos \phi_k s_k + \tilde{e} s_k'') = \hat{Q}_\phi + H.O.T. \tag{3.6}$$

where H.O.T. means higher-order terms.

Detailed steps and assumptions are not given here and can be found in [60]. After rearranging the terms, the decoupled blade equations were obtained as

$$s_j'' + \hat{k}_0 s_j = Q_{j0} - \hat{d}\sin\left(\phi + \frac{2\pi}{3}j\right) + \epsilon\left[Q_{j1}\cos\left(\phi + \frac{2\pi}{3}j\right) - \tilde{e}Q_{\phi 0} + \tilde{e}\hat{c}_r - \hat{c}_b s_j' - \tilde{k}_{v_j} s_j \right.$$
$$\left. -\hat{k}_2\cos\left(\phi + \frac{2\pi}{3}j\right)s_j + \tilde{e}^2\sum_{k=1}^{3} s_k''\right], \tag{3.7}$$

3.3 Second-Order Method of Multiple Scales

We reorganize Equation (3.7) on the basis of new independent variable $\psi = p_1\phi$, where $p_1 = \sqrt{\hat{k}_0} = \sqrt{\frac{k_0/\Omega^2 + k_1}{m_b}}$. The equation of motion in the ψ domain becomes

$$s_j'' + s_j = F_j - F_{j0}\sin\left(\omega_1\psi + \frac{2\pi}{3}j\right) + \epsilon\left[F_{j1}\cos\left(\omega_1\psi + \frac{2\pi}{3}j\right) + f - \zeta s_j' - \kappa_{v_j} s_j + \tilde{e}^2\sum_{k=1}^{3} s_k'' \right.$$
$$\left. -\kappa\cos\left(\omega_1\psi + \frac{2\pi}{3}j\right)s_j\right], \tag{3.8}$$

where now $()' = \frac{d}{d\psi}$ and $F_j = \frac{Q_{j0}}{\hat{k}_0}, \quad F_{j0} = \frac{\hat{d}}{\hat{k}_0}, \quad \omega_1 = \frac{1}{p_1}, \quad F_{j1} = \frac{Q_{j1}}{\hat{k}_0}, \quad f = \frac{\tilde{e}(\hat{c}_r - Q_{\phi 0})}{\hat{k}_0},$
$\zeta = \frac{\hat{c}_b}{p_1}, \quad \kappa = \frac{\hat{k}_2}{\hat{k}_0}, \quad \kappa_{v_j} = \frac{\tilde{k}_{v_j}}{\hat{k}_0}$

According to the first-order perturbation analysis on linear tuned and mistuned 3-blade horizantal axis wind turbine, superharmonic resonance exists at order two at the system natural frequency [60]. By applying the second-order perturbation analysis [26] to Equation (3.8) we include three scales (ψ_0, ψ_1, ψ_2) and s_j is separated into dominant solution s_{j0} and small variations s_{j1} and s_{j2} such that

$$s_j = s_{j0}(\psi_0, \psi_1, \psi_2) + \epsilon s_{j1}(\psi_0, \psi_1, \psi_2) + \epsilon^2 s_{j2}(\psi_0, \psi_1, \psi_2) \tag{3.9}$$

where $\psi_i = \epsilon^i \psi_0$.

Then $\dfrac{d}{d\psi} = D_0 + \epsilon D_1 + \epsilon^2 D_2$, $\quad \dfrac{d^2}{d\psi^2} = D_0^2 + \epsilon(2D_0D_1) + \epsilon^2(D_1^2 + 2D_0D_2)$, where $D_i = \dfrac{\partial}{\partial \psi_i}$

These formulations are plugged into Equation (3.8) and then we balance the coefficients of ϵ^0, ϵ^1 and ϵ^2:

$$O(1) : D_0^2 s_{j0} + s_{j0} = F_j - \tilde{F}_{j0} \sin\left(\omega_1\psi_0 + \frac{2\pi}{3}j\right) \tag{3.10}$$

where $\tilde{F}_{j0} \sin\left(\omega_1\psi_0 + \dfrac{2\pi}{3}j\right) = F_{j0} \sin\left(\omega_1\psi_0 + \dfrac{2\pi}{3}j\right) + \epsilon f$.

$O(\epsilon)$:

$D_0^2 s_{j1} + s_{j1} = -2D_0D_1 s_{j0} - \zeta D_0 s_{j0} - \kappa_{v_j} s_{j0} + \tilde{e}^2 \sum_{k=1}^3 D_0^2 s_{k0} - \kappa \cos\left(\omega_1\psi_0 + \frac{2\pi}{3}j\right) s_{j0}$

$+F_{j1} \cos\left(\omega_1\psi_0 + \frac{2\pi}{3}j\right)$

$O(\epsilon^2)$:

$D_0^2 s_{j2} + s_{j2} = -2D_0D_1 s_{j1} - 2D_0D_2 s_{j0} - D_1^2 s_{j0} - \zeta D_0 s_{j1} - \zeta D_1 s_{j0} - \kappa_{v_j} s_{j1}$

$-\kappa cos(\omega_1\psi_0 + \phi_j) s_{j1} + \tilde{e}^2 \sum_{k=1}^3 (2D_0D_1 s_{k0} + D_0^2 s_{k1})$

(3.11)

Solving the $O(1)$ Equation (3.10), s_{j0} is determined as

$$s_{j0} = \frac{F_j}{2} + A_j e^{i\psi_0} - i\Lambda_j e^{i(\omega_1\psi_0)} + \text{c.c.} \tag{3.12}$$

where $A_j = (X_j + iY_j)e^{i\sigma\epsilon\psi_0}$ and $\Lambda_j = \frac{F_{j0}}{2(1-\omega_1^2)}e^{i\phi_j}$ and $c.c$ refers to complex conjugate. X and Y are functions of ψ_1 and ψ_2. The s_{j0} Equation (3.12) is plugged into the $O(\epsilon)$ Equation (3.11), and then we rewrite $O(\epsilon)$ equation

$$
\begin{aligned}
&D_0^2 s_{j1} + s_{j1} = -2iD_1 A_j e^{i\psi_0} - \zeta\left(\Lambda_j\omega_1 e^{i\omega_1\psi_0} + iA_j e^{i\psi_0}\right) + c.c. \\
&-\tfrac{1}{2}\left(\kappa e^{i\phi_j} e^{i\psi_0\omega_1} + c.c.\right)\left(F_j - i\Lambda_j e^{i\psi_0\omega_1} + A_j e^{i\psi_0} + i\bar{\Lambda}_j e^{-i\psi_0\omega_1} + \bar{A}_j e^{-i\psi_0}\right) \\
&+\tfrac{1}{2}\left(F_{j1} e^{i\phi_j} e^{i\psi_0\omega_1} + F_{j1} e^{-i\phi_j} e^{-i\psi_0\omega_1}\right) - \kappa_{v_j}\left(\frac{F_j}{2} + A_j e^{i\psi_0} - i\Lambda_j e^{i\omega_1\psi_0} + c.c.\right) \\
&+\tilde{e}^2 \textstyle\sum_{k=1}^{3}\left(i\omega_1^2 A_k e^{i\omega_1\psi_0} - A_k e^{i\psi_0} + \text{c.c}\right)
\end{aligned}
\tag{3.13}
$$

Four different resonance conditions can be identified from Equation (3.13):

1. No specific relation between ω_1 and the natural order=1
2. $\omega_1 \approx 1$
3. $\omega_1 \approx 2$
4. $\omega_1 \approx 1/2$

The case of $\omega_1 \approx 1$ is properly treated with soft excitation. $\omega_1 \approx 2$ and $\omega_1 \approx 1/2$ were studied in [60].

3.3.1 Nonresonant Case at $O(\epsilon)$

We concentrate on the first case where there is no specific relationship between forcing frequency and natural frequency. The nonresonant solvability condition for Equation (3.13) is found by eliminating the coefficient of secular terms $e^{i\psi_0}$:

$$-2iD_1A_j - \zeta iA_j - \tilde{e}^2\sum_{k=1}^{3}A_k - \kappa_{v_j}A_j = 0 \tag{3.14}$$

We solve the rest of Equation (3.13) which corresponds to nonresonant terms to obtain the particular solution. Since A_j is not a function of independent variable ψ_0, we treat A_j as constant. Then

$$s_{j1} = \frac{Q_j}{2} + U_je^{i\omega_1\psi_0} + V_je^{i(\omega_1-1)\psi_0} + W_je^{i(\omega_1+1)\psi_0} + L_je^{i2\omega_1\psi_0} + \text{c.c.} \tag{3.15}$$

where

$$Q_j = -i\kappa e^{i\phi_j}\bar{\Lambda}_j + i\kappa e^{-i\phi_j}\Lambda_j, \quad U_j = \frac{1}{1-\omega_1^2}\left(\frac{1}{2}F_{j1}e^{i\phi_j} - \zeta\Lambda_j\omega_1 - \frac{\kappa}{2}e^{i\phi_j}F_j + \tilde{e}^2\textstyle\sum_{k=1}^{3}i\omega_1^2\Lambda_j\right),$$

$$V_j = -\frac{1}{1-(\omega_1-1)^2}\left(\frac{\kappa}{2}e^{i\phi_j}\bar{A}_j\right), \quad W_j = -\frac{1}{1-(\omega_1+1)^2}\left(\frac{\kappa}{2}e^{i\phi_j}A_j\right), \quad L_j = \frac{i\kappa\Lambda_j}{2(1-4\omega_1^2)}$$

Then, we plug s_{j0} and s_{j1} from Equation (3.12) and Equation (3.15) into Equation (3.11). After we reorganize the $O(\epsilon^2)$ equation, we have

$$
\begin{aligned}
D_0^2 s_{j2} + s_{j2} = & -D_1^2(A_j)e^{i\psi_0} - 2iD_2(A_j)e^{i\psi_0} - \zeta D_1(A_j)e^{i\psi_0} + \kappa_{v_j}\Bigg(\frac{Q_j}{2} + U_j e^{i\omega_1\psi_0} \\
& + V_j e^{i(\omega_1-1)\psi_0} + W_j e^{i(\omega_1+1)\psi_0}\Bigg) - \zeta\Bigg(i(\omega_1-1)V_j e^{i(\omega_1-1)\psi_0} + i(\omega_1+1)W_j e^{i(\omega_1+1)\psi_0} \\
& + i\omega_1 U_j e^{i\omega_1\psi_0} + 2i\omega_1 L_j e^{2i\omega_1\psi_0}\Bigg) - \frac{1}{2}\left(\kappa e^{i\phi_j} e^{i\psi_0\omega_1} + c.c\right)\left(\frac{Q_j}{2} + U_j e^{i\omega_1\psi_0} + V_j e^{i(\omega_1-1)\psi_0}\right. \\
& \left. + W_j e^{i(\omega_1+1)\psi_0} + L_j e^{i2\omega_1\psi_0} + \text{c.c.}\right) + \tilde{\epsilon}^2 \textstyle\sum_{k=1}^{3}\Bigg(-(\omega_1+1)^2 W_k e^{i(\omega_1+1)\psi_0} - 4\omega_1^2 L_k e^{2i\omega_1\psi_0} \\
& -\omega_1^2 U_k e^{i\omega_1\psi_0} - (\omega_1-1)^2 V_k e^{i(\omega_1-1)\psi_0} + 2iD_1 A_k e^{i\psi_0}\Bigg) - 2\Bigg(\frac{i\kappa(\omega_1-1)e^{i\phi_j} D_1\bar{A}_j}{2(1-(\omega_1-1)^2)} e^{i(\omega_1-1)\phi_j} \\
& -\frac{i\kappa(\omega_1+1)e^{i\phi_j} D_1 A_j}{2(1-(\omega_1+1)^2)} e^{i(\omega_1+1)\phi_j}\Bigg) + c.c
\end{aligned}
\tag{3.16}
$$

By examining the Equation (3.16), we observe the resonance conditions as follows.

1. No specific relation between ω_1 and the natural order=1
2. $\omega_1 \approx 1$
3. $\omega_1 \approx 2$
4. $\omega_1 \approx 1/2$
5. $\omega_1 \approx 1/3$

The cases $\omega_1 \approx 1$, $\omega_1 \approx 2$ and $\omega_1 \approx 1/2$, if properly treated, would have added a secular term to the Equation (3.14), removed a secular term from Equation (3.15), and hence Equation (3.16) would need to be adjusted.

3.3.2 Superharmonic Case at Order 3 at $O(\epsilon^2)$

In our paper, we specifically focus on the superharmonic resonance case at $\omega_1 \approx 1/3$. In the time domain, this means that $\Omega \approx \omega_n/3$, where ω_n is the lowest oscillatory modal frequency. As we follow the same steps in [26] and [29], we obtain the solvability condition for superharmanic case from Equation (3.16), using $3\omega_1 = 1 + \epsilon\sigma$, as

$$-2iD_2(A_j) - \zeta D_1(A_j) - D_1^2 A_j - \frac{\kappa}{2} L_j e^{i\phi_j} e^{i\sigma\epsilon\psi_0} + 2i\tilde{e}^2 \sum_{k=1}^{3} D_1(A_k) = 0 \tag{3.17}$$

From the Equation (3.14),

$$D_1 A_j = -\frac{\zeta}{2} A_j + \frac{1}{2} i\tilde{e}^2 \sum_{k=1}^{3} A_k + \frac{1}{2} i\kappa_{v_j} A_j$$

We computed the $D_1^2 A_j$ equation by differentiating the expression of $D_1 A_j$. Inserting the undifferentiated $D_1 A_j$ equation into it, to obtain

$$D_1^2 A_j = \left(\frac{\zeta^2}{4} - \frac{i\kappa_{v_j}\zeta}{2} - \frac{1}{4}\kappa_{v_j}^2\right) A_j + \tilde{e}^2 \sum_{k=1}^{3} A_k \left(-\frac{3\tilde{e}^2}{4} - \frac{i\zeta}{2} - \frac{\kappa_{v_j}}{2}\right)$$

Inserting the equation above into the Equation (3.17), we end up with the $D_2 A_j$ equation as

$$D_2 A_j = \left(-\frac{1}{8} i\zeta^2 - \frac{1}{8} i\kappa_{v_j}^2\right) A_j - \frac{1}{4} i\kappa L_j e^{(\phi_j + \sigma\epsilon\psi_0)i} + \left(\frac{9}{8} i\tilde{e}^4 + \frac{1}{4} i\kappa_{v_j}\tilde{e}^2 - \frac{1}{2}\zeta\tilde{e}^2\right) \sum_{k=1}^{3} A_k \tag{3.18}$$

For the purpose of obtaining an expression for A_j, solvability condition equations $D_1 A_j$ and $D_2 A_j$ need to be solved together. We recombine the ψ and ψ_1, ψ_2 scales in a process. This process is called as "reconstitution" [26] and [29]. The reconstitution equation is

$$\frac{dA_j}{d\psi} = \epsilon D_1 A_j + \epsilon^2 D_2 A_j \tag{3.19}$$

After $D_1 A_j$ and $D_2 A_j$ equations are inserted into the Equation (3.19), we obtain the reconstituted differential equation as

$$\frac{dA_j}{d\psi} = \epsilon\left(\frac{-\zeta A_j}{2} + \frac{i\tilde{e}^2}{2}\sum_{k=1}^3 A_k + \frac{i\kappa v_j}{2}A_j\right) + \epsilon^2\left(-\frac{i\zeta^2}{8} - \frac{i\kappa_{v_j}^2}{8}\right)A_j - \epsilon^2\left(\frac{\kappa^2\Lambda_j}{8(1-4\omega_1^2)}e^{(\phi_j+\sigma\epsilon\psi_0)i}\right)$$

$$+\epsilon^2\tilde{e}^2\left(\frac{9}{8}i\tilde{e}^2 - \frac{\zeta}{2} + \frac{\mathrm{i}\kappa \mathrm{v_j}}{4}\right)\sum_{k=1}^3 A_k \tag{3.20}$$

We look for a solution in the Cartesian coordinate form $A = (X + iY)e^{(i\sigma\epsilon\psi_0)}$.
A_j and $\Lambda_j = \dfrac{F_{j0}}{2(1-\omega_1^2)}e^{i\phi_j}$ equations are inserted into the Equation (3.20), and each side of equation divided by $e^{(i\sigma\epsilon\psi_0)}$. Then we split the equation into real and imaginary parts. After simplification, we obtain

Real part:

$$\dot{X}_j = z_1X_j + z_2\sum_{k=1}^{3}X_k + z_3Y_j + z_4\sum_{k=1}^{3}Y_k + z_5\cos(2\phi_j) \tag{3.21}$$

Imaginary part:

$$\dot{Y}_j = -z_3X_j - z_4\sum_{k=1}^{3}X_k + z_1Y_j + z_2\sum_{k=1}^{3}Y_k + z_5\sin(2\phi_j) \tag{3.22}$$

where z_1, z_2, z_3, z_4, z_5 can be found in the Appendix C.1. For steady state behavior, $\dot{X}_j = 0$ and $\dot{Y}_j = 0$. We can find a polar form $A_j = \frac{1}{2}\mathrm{a}_j e^{i\beta}$ by using X_j and Y_j. Then the response amplitude is given as $a_j = 2\sqrt{X_j^2 + Y_j^2}$.

3.4 Results

In this section, we analyze the second-order superharmonic resonance behavior for tuned and mistuned blades. Table 3.1 lists the frequency ratios at which resonances have been identified by first or second-order method of multiple scales expansion. As seen in Table 3.1, second-order perturbation analysis reveals the superharmonic resonances at order 3 for tuned and mistuned case.

Table 3.1: Resonance Chart. R_1: Resonance identified at first-order of MMS expansion. R_2: Resonance identified at second-order of MMS expansion. $-$: Known resonance case/ Instability not uncovered up to two orders of expansion

Forcing (ω_1)	Tuned	Mistuned
1	R_1	R_1
2	R_1	R_1
2/3	-	-
1/2	R_1	R_1
1/3	R_2	R_2

3.4.1 Tuned Blade Case ($\kappa_v = 0$)

Here, we assume that there is no mistuning on the turbine blades ($\kappa_{v_j} = 0$). Then the magnitude of steady state response amplitude a is the same for each blade, and is given as

$$a = \left| \frac{\epsilon^2 E_j}{\sqrt{\frac{\epsilon^2\zeta^2}{4} + \left(\epsilon\sigma + \frac{\epsilon^2\zeta^2}{8}\right)^2}} \right| = \frac{\epsilon E}{\sqrt{\frac{\zeta^2}{4} + \left(\sigma + \frac{\epsilon\zeta^2}{8}\right)^2}} \tag{3.23}$$

where $E = |E_j| = \left|\frac{\kappa^2 \Lambda_j}{8(1-4\omega_1^2)}\right|$, noting Λ_j are equal for all j.

For convenience, we defined $\lambda_j = \frac{\Lambda_j}{8(1-4\omega_1^2)}$ so E_j and λ become as

$$E = |E_j| = \kappa^2 \lambda \qquad\qquad \lambda = \frac{F_{j0}}{16(1-\omega_1^2)(1-4\omega_1^2)} \tag{3.24}$$

From Equation (3.23), we obtain a_{max} and σ_{max} as

$$a_{max} = \frac{2\epsilon E_j}{\zeta} \qquad\qquad \sigma_{max} = -\frac{\epsilon\zeta^2}{8} \tag{3.25}$$

Figure 3.2 demonstrates a numerical plot for all three blade amplitudes with respect to detuning parameter. It states that three of the blade amplitudes are same because of the symmetry. For same

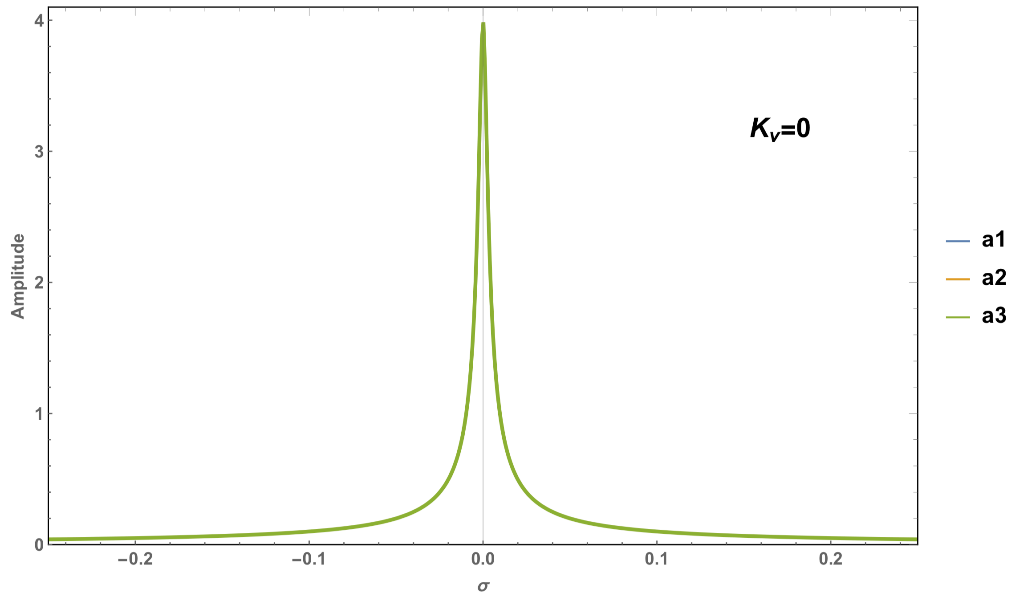

Figure 3.2: Steady state superharmonic resonance response amplitudes versus detuning parameter for $\tilde{e} = 0.2$, $\kappa = 0.1$, $|\lambda| = 10$, $\phi = 0$, $\epsilon = 0.1$, $\zeta = 0.005$ (a1: first blade, a2: second blade, a3: third blade)

set of parameters that are used for plot give $a_{max} = 4$ at $\sigma = 0.000375$ from the Equation (3.25). These values are consistent with the maximum value in Figure 3.2.

Amplitude versus frequency plots are shown in Figure 3.3 and Figure 3.4. When ζ decreases the resonance amplitude get sharpened and when $|\lambda\kappa|$ increases amplitude increases as well, where λ is defined in the Appendix C.1. In all figures, damping factor act as $\hat{\zeta}$ which is $\hat{\zeta} = \frac{\epsilon\zeta}{2}$.

3.4.2 Mistuned Blade Case ($\kappa_v \neq 0$)

In this section we apply mistuning κ_v to a single blade and observe its effect on the amplitudes of the three blades. Figure 3.5 presents the amplitudes of each blade for a specific set of parameters as κ_v varies.

For the symmetric case when $\kappa_v = 0$, all blades have the same amplitude. When κ_v is very small, amplitudes are significantly affected. As seen from the plot, when mistuning grows, the third blade (mistuned blade) amplitude decreases. The second blade's amplitude, with very small mistuning, gets larger than in the symmetric case. For various values of mistuning parameter κ_v, the

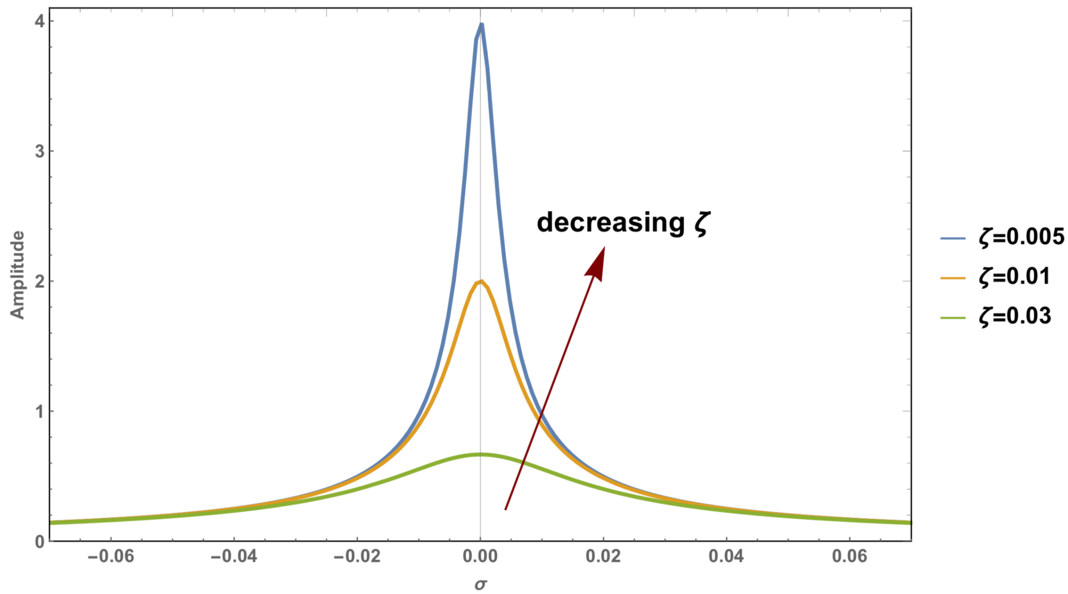

Figure 3.3: Steady state superharmonic resonance response amplitudes versus frequency for $\tilde{e} = 0.2$, $\kappa = 0.1$, $|\lambda| = 10$, $\phi = 0$, $\epsilon = 0.1$, $\zeta = 0.005, 0.01, 0.03$

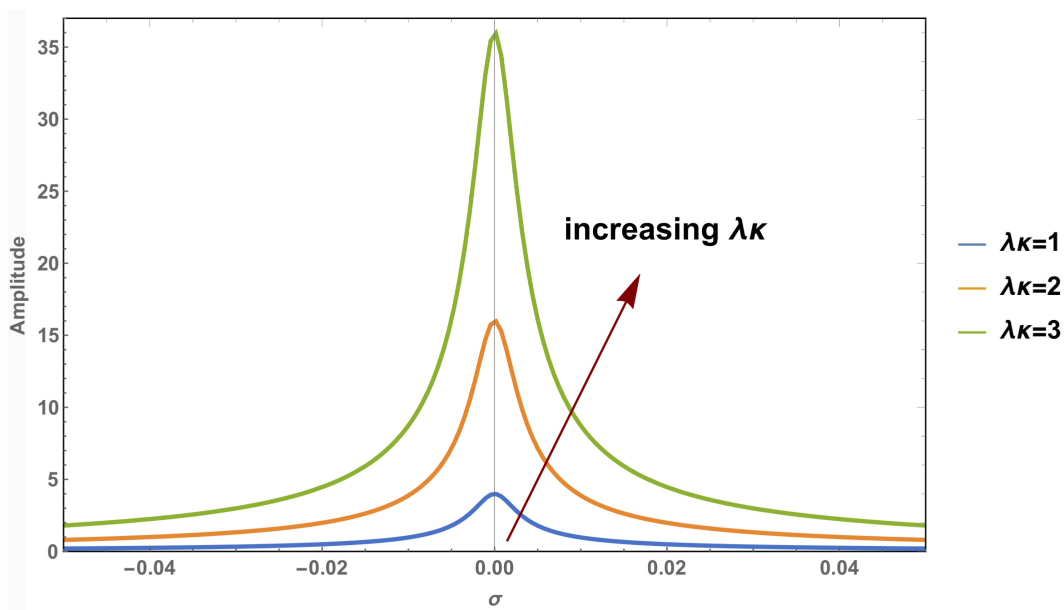

Figure 3.4: Steady state superharmonic resonance response amplitudes versus frequency for $\tilde{e} = 0.2$, $\phi = 0$, $\epsilon = 0.1$, $\zeta = 0.005$, $\lambda\kappa = 1, 2, 3$

superharmonic resonance amplitude changes with respect to detuning parameter σ, as illustrated in Figure 3.6, Figure 3.7, Figure 3.8 and Figure 3.9. The single resonance peak which is seen in Figure 3.2 is split up by mistuning which can be seen on mistuned case plots. Comparing to the symmetric case amplitude in Figure 3.2 and mistuned case amplitude for $\kappa_v = 0.006$ in Figure 3.6, the resonance amplitude for one blade is increased for the same set of parameters, while the other blade amplitudes have decreased. This points to the possibility of vibration localization.

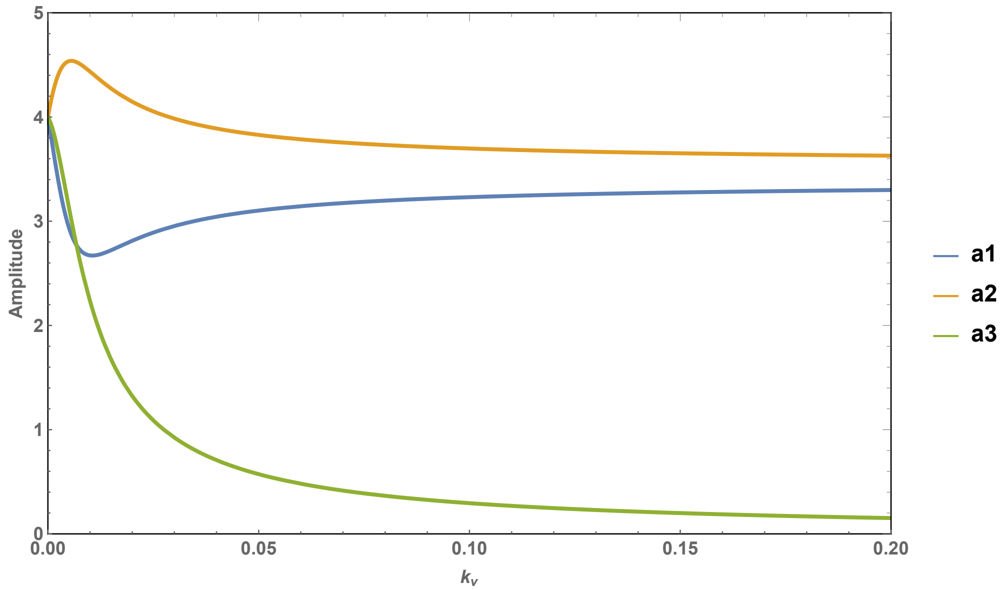

Figure 3.5: Steady state superharmonic resonance response amplitudes versus elastic stiffness mistuning parameter κ_v for $\tilde{e} = 0.2$, $\kappa = 0.1$, $|\lambda| = 1$, $\phi = 0$, $\epsilon = 0.1$, $\zeta = 0.005$, $\sigma = 0$ (a1: first blade, a2: second blade, a3: third blade)

3.5 Remaining Task

We expect that constant load can cause superharmonic resonance which was not revealed on first-order perturbation analysis. Here, we apply second-order perturbation analysis focusing on constant loading.

3.5.1 Superharmonic Case at Order 2 at $O(\epsilon)$

As a second case where $\omega_1 \approx 1/2$ is studied at order of $O(\epsilon)$. The superharmonic solvability condition at order 2 for Equation (3.13) is obtained by cancelling the coefficient of secular terms $e^{i\psi_0}$ and $e^{i2\omega_1\psi_0}$ out.

$$-2iD_1A_j - \zeta iA_j - \tilde{e}^2\sum_{k=1}^{3}A_k - \kappa_{v_j}A_j + \frac{1}{2}i\kappa\Lambda_j e^{i\phi_j}e^{i\sigma\epsilon\psi_0} = 0 \tag{3.26}$$

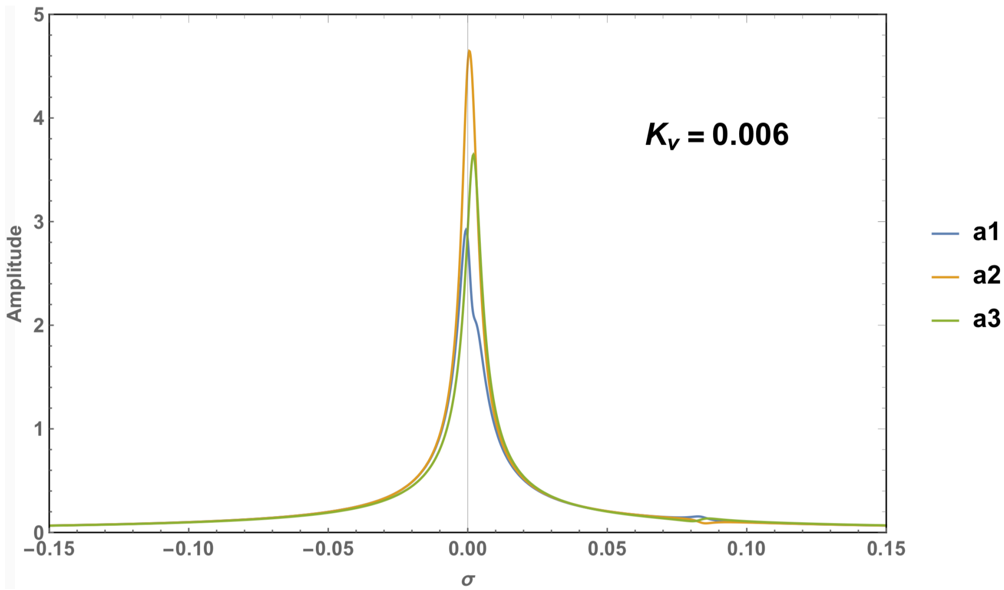

Figure 3.6: Steady state superharmonic resonance response amplitudes versus detuning parameter for $\tilde{e} = 0.2$, $\kappa = 0.1$, $|\lambda| = 10$, $\phi = 0$, $\epsilon = 0.1$, $\zeta = 0.005$ (a1: first blade, a2: second blade, a3: third blade)

After we remove the terms that Equation (3.26) have from Equation (3.13), rest of the equation is solved to get the particular solution. Equation (3.13) becomes

$$D_0^2 s_{j1} + s_{j1} = \frac{Q_j}{2} + P_j e^{i\omega_1 \psi_0} + R_j e^{i(\omega_1 - 1)\psi_0} + S_j e^{i(\omega_1 + 1)\psi_0} + \text{c.c.} \tag{3.27}$$

where $Q_j = -i\kappa e^{i\phi_j}\bar{\Lambda}_j + i\kappa e^{-i\phi_j}\Lambda_j - \kappa_{v_j} F_j$, $\quad P_j = \frac{1}{2} F_{j1} e^{i\phi_j} - \zeta \Lambda_j \omega - \frac{\kappa}{2} e^{i\phi_j} F_j + \tilde{e}^2 \sum_{k=1}^{3} i\omega^2 A_k$,

$R_j = -\frac{\kappa}{2} e^{i\phi_j} \bar{A}_j$, $\quad S_j = -\frac{\kappa}{2} e^{i\phi_j} A_j$

Solving the Equation (3.27) to find the s_{j1}

$$s_{j1} = \frac{Q_j}{2} + U_j e^{i\omega_1 \psi_0} + V_j e^{i(\omega_1 - 1)\psi_0} + W_j e^{i(\omega_1 + 1)\psi_0} + \text{c.c.} \tag{3.28}$$

where $\quad U_j = \frac{P_j}{1 - \omega_1^2}, \quad V_j = -\frac{R_j}{1 - (\omega_1 - 1)^2}, \quad W_j = -\frac{S_j}{1 - (\omega_1 + 1)^2}$

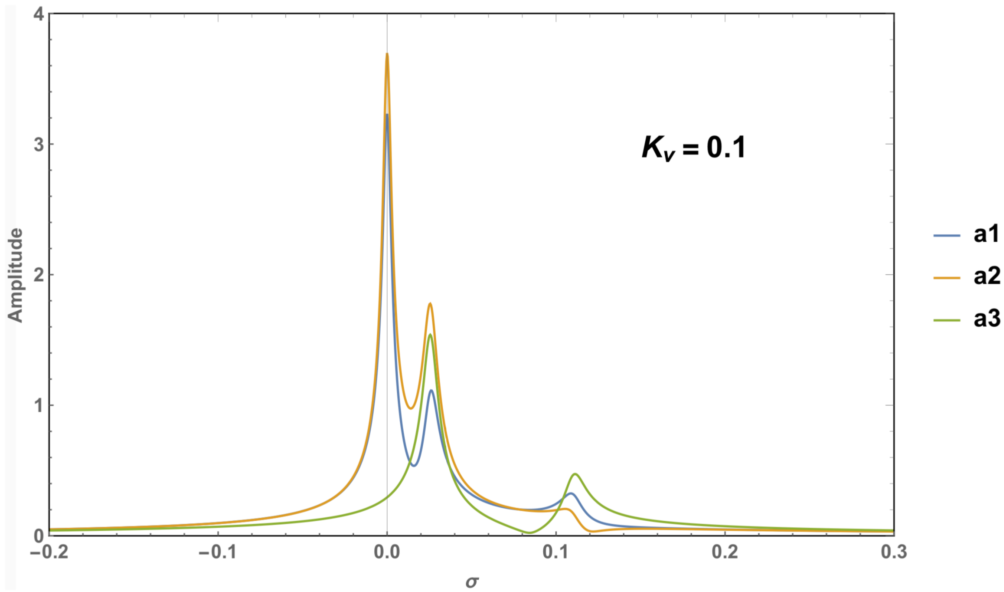

Figure 3.7: Steady state superharmonic resonance response amplitudes versus detuning parameter for $\tilde{e} = 0.2$, $\kappa = 0.1$, $|\lambda| = 10$, $\phi = 0$, $\epsilon = 0.1$, $\zeta = 0.005$ (a1: first blade, a2: second blade, a3: third blade)

Inserting the Equations (3.12) and (3.28) into Equation (3.11) gives us

$$
\begin{aligned}
&D_0^2 s_{j2} + s_{j2} = -D_1^2(A_j)e^{i\psi_0} - 2iD_2(A_j)e^{i\psi_0} - \zeta D_1(A_j)e^{i\psi_0} + \kappa_{v_j}\left(\frac{Q_j}{2} + U_j e^{i\omega_1\psi_0} + V_j e^{i(\omega_1-1)\psi_0}\right.\\
&\left.+W_j e^{i(\omega_1+1)\psi_0} + \text{c.c}\right) - \zeta\left(i\omega_1 U_j e^{i\omega_1\psi_0} + i(\omega_1-1)V_j e^{i(\omega_1-1)\psi_0} + i(\omega_1+1)W_j e^{i(\omega_1+1)\psi_0} + \text{c.c.}\right)\\
&-\frac{1}{2}\left(\kappa e^{i\phi_j} e^{i\psi_0\omega_1} + c.c\right)\left(\frac{Q_j}{2} + U_j e^{i\omega_1\psi_0} + V_j e^{i(\omega_1-1)\psi_0} + W_j e^{i(\omega_1+1)\psi_0} + \text{c.c.}\right)\\
&+\tilde{e}^2\sum_{k=1}^{3}\left(-(\omega_1-1)^2 V_k e^{i(\omega_1-1)\psi_0} - (\omega_1+1)^2 W_k e^{i(\omega_1+1)\psi_0} - \omega_1^2 U_k e^{i\omega_1\psi_0} + 2iD_1 A_k e^{i\psi_0}\right)\\
&-2\left(\frac{i\kappa(\omega_1-1)e^{i\phi_j}D_1\bar{A}_j}{2(1-(\omega_1-1)^2)}e^{i(\omega_1-1)\phi_j} - \frac{i\kappa(\omega_1+1)e^{i\phi_j}D_1 A_j}{2(1-(\omega_1+1)^2)}e^{i(\omega_1+1)\phi_j}\right) + c.c
\end{aligned}
\tag{3.29}
$$

Examining the Equation (3.29) for the superharmonic case at order 2, we arrive at the following resonance cases:

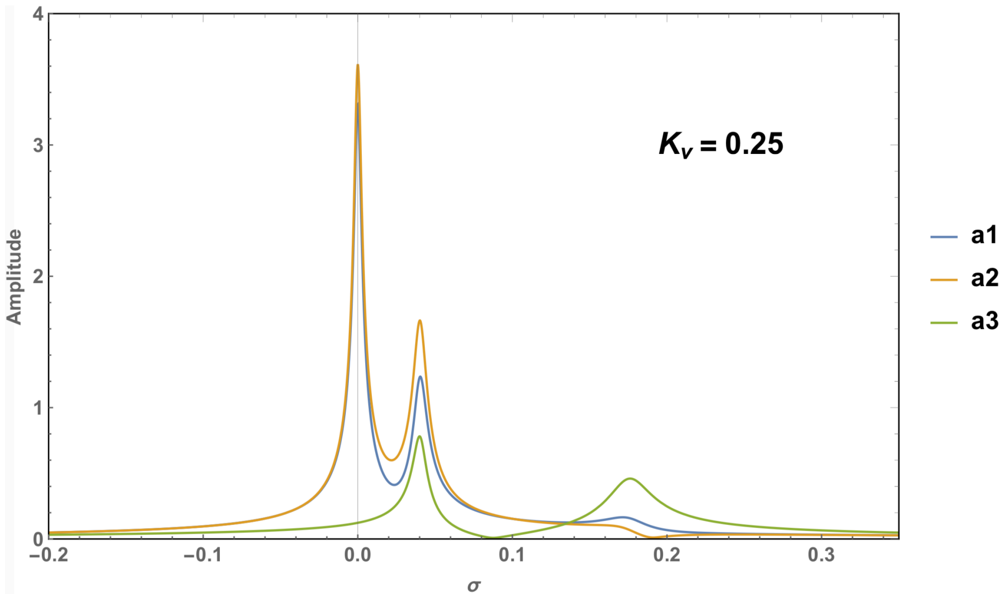

Figure 3.8: Steady state superharmonic resonance response amplitudes versus detuning parameter for $\tilde{e} = 0.2$, $\kappa = 0.1$, $|\lambda| = 10$, $\phi = 0$, $\epsilon = 0.1$, $\zeta = 0.005$ (a1: first blade, a2: second blade, a3: third blade)

1. No specific relation between ω_1 and the natural order=1

2. $\omega_1 \approx 1$

3. $\omega_1 \approx 2$

4. $\omega_1 \approx 1/2$

If we redo the analyses for $\omega_1 \approx 1$ and $\omega_1 \approx 2$ cases properly, Equation (3.29) will need to be adjusted.

3.5.2 Superharmonic Case at Order 2 at $O(\epsilon^2)$

We will focus on specifically superharmonic resonance case at order 2 for second expansion. As we follow the same steps in Section 3.3.2, we receive the solvability condition for superharmonic case from Equation (3.29), using $2\omega_1 = 1 + \epsilon\sigma$, as

$$-2iD_2A_j - \zeta D_1A_j - D_1^2A_j - \frac{\kappa}{2}U_je^{i\phi_j}e^{i\sigma\epsilon\psi_0} + 2i\tilde{e}^2\sum_{k=1}^{3}D_1(A_k) \tag{3.30}$$

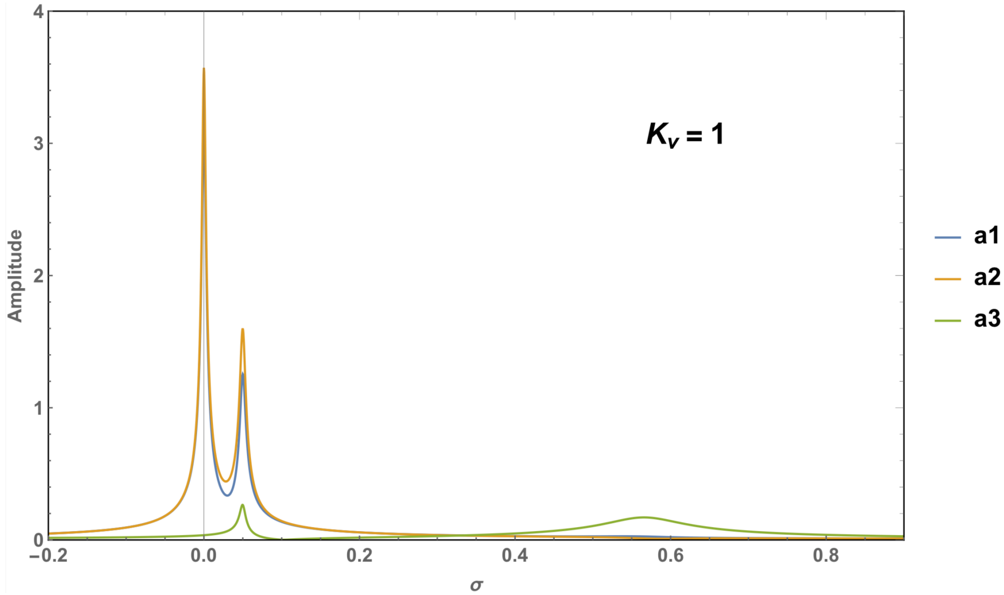

Figure 3.9: Steady state superharmonic resonance response amplitudes versus detuning parameter for $\tilde{e} = 0.2$, $\kappa = 0.1$, $|\lambda| = 10$, $\phi = 0$, $\epsilon = 0.1$, $\zeta = 0.005$ (a1: first blade, a2: second blade, a3: third blade)

From the Equation (3.26),

$$D_1 A_j = -\frac{\zeta}{2} A_j + \frac{1}{2} i\tilde{e}^2 \sum_{k=1}^{3} A_k + \frac{1}{2} i\kappa_{v_j} A_j + \frac{1}{4}\kappa \Lambda_j e^{i\phi_j} e^{i\sigma\epsilon\psi_0} \tag{3.31}$$

Using Equation (3.31), $D_1^2 A_j$ is derived as

$$D_1^2 A_j = \frac{\zeta}{2} D_1 A_j + \frac{i\tilde{e}^2}{2} \sum_{k=1}^{3} D_1 A_k + \frac{i\kappa_{v_j}}{2} D_1 A_j$$

Inserting the $D_1^2 A_j$ and $D_1 A_j$ expressions into the Equation (3.30), then we obtain the $D_2 A_j$ equation as

$$D_2 A_j = \left(-\frac{1}{8} i\zeta^2 - \frac{1}{8} i\kappa_{v_j}^2\right) A_j + \left(\frac{9}{8} i\tilde{e}^4 + \frac{1}{4} i\kappa_{v_j}\tilde{e}^2 - \frac{1}{2}\zeta\tilde{e}^2\right) \sum_{k=1}^{3} A_k + \frac{\kappa\Lambda_j}{16}(i\zeta - \kappa_{v_j}) e^{i\phi_j} e^{i\sigma\epsilon\psi_0}$$

$$+ \frac{3\tilde{e}^2\kappa}{16} \sum_{k=1}^{3} \Lambda_k e^{(i\phi_k)} e^{(i\sigma\epsilon\psi_0)} + \left(\frac{i\kappa F_{j1} e^{i2\phi_j}}{8(1-\omega_1^2)} - \frac{\zeta i\kappa\Lambda_j\omega_1 e^{i\phi_j}}{8(1-\omega_1^2)} - \frac{i\kappa^2 F_j e^{i2\phi_j}}{16(1-\omega_1^2)} - \frac{\kappa\tilde{e}^2\omega_1^2 e^{i\phi_j}}{8(1-\omega_1^2)} \sum_{k=1}^{3} A_k\right) e^{i\sigma\epsilon\psi_0} \tag{3.32}$$

Solvability conditions D_1A_j and D_2A_j will be solved together to determine the A_j equation. Recombining the time scales (ψ_1, ψ_2, ψ_3) in process allow us to determine the reconstitution.

$$\frac{dA_j}{d\psi} = \epsilon D_1 A_j + \epsilon^2 D_2 A_j \tag{3.33}$$

Equations D_1A_j and D_2A_j are inserted into the Equation (3.33) to get the reconstituted differential equation as

$$\begin{aligned}\frac{dA_j}{d\psi} &= \epsilon\left(-\frac{\zeta}{2}A_j + \frac{1}{2}i\tilde{e}^2\sum_{k=1}^{3}A_k + \frac{1}{2}i\kappa_{v_j}A_j + \frac{1}{4}\kappa\Lambda_j e^{i\phi_j}e^{i\sigma\epsilon\psi_0}\right) + \epsilon^2\Bigg[\left(-\frac{1}{8}i\zeta^2 - \frac{1}{8}i\kappa_{v_j}^2\right)A_j \\ &+\left(\tfrac{9}{8}i\tilde{e}^4 + \tfrac{1}{4}i\kappa_{v_j}\tilde{e}^2 - \tfrac{1}{2}\zeta\tilde{e}^2\right)\textstyle\sum_{k=1}^{3}A_k + \frac{\kappa\Lambda_j}{16}(i\zeta - \kappa_{v_j})e^{i\phi_j}e^{i\sigma\epsilon\psi_0} + \frac{3\tilde{e}^2\kappa}{16}\sum_{k=1}^{3}\Lambda_k e^{(i\phi_k)}e^{i\sigma\epsilon\psi_0} \\ &+\left(\frac{i\kappa F_{j1}e^{i2\phi_j}}{8(1-\omega_1^2)} - \frac{\zeta i\kappa\Lambda_j\omega_1 e^{i\phi_j}}{8(1-\omega_1^2)} - \frac{i\kappa^2 F_j e^{i2\phi_j}}{16(1-\omega_1^2)} - \frac{\kappa\tilde{e}^2\omega_1^2 e^{i\phi_j}}{8(1-\omega_1^2)}\textstyle\sum_{k=1}^{3}A_k\right)e^{i\sigma\epsilon\psi_0}\Bigg]\end{aligned} \tag{3.34}$$

$A = (X + iY)e^{(i\sigma\epsilon\psi_0)}$ and $\Lambda_j = \dfrac{F_{j0}}{2(1-\omega_1^2)}e^{i\phi_j}$ terms are inserted into Equation (3.34) and later $\dfrac{dA_j}{d\psi}$ equation is divided by $e^{i\sigma\epsilon\psi_0}$. Subsequently, we find out real and imaginary parts as

Real part:

$$\begin{aligned}\dot{X}_j = C_1X_j + C_2\sum_{k=1}^{3}X_k + C_3Y_j + C_4\sum_{k=1}^{3}Y_k + C_5\cos(\phi_j)\sum_{k=1}^{3}X_k + C_6\sin(2\phi_j) + C_7\cos(2\phi_j) \\ + C_8\sum_{k=1}^{3}\cos(2\phi_k)\end{aligned} \tag{3.35}$$

Imaginary part:

$$\begin{aligned}\dot{Y}_j = -C_3X_j - C_4\sum_{k=1}^{3}X_k + C_1Y_j + C_2\sum_{k=1}^{3}Y_k + C_5\sin(\phi_j)\sum_{k=1}^{3}X_k - C_6\cos(2\phi_j) + C_7\sin(2\phi_j) \\ + C_8\sum_{k=1}^{3}\sin(2\phi_k)\end{aligned} \tag{3.36}$$

where $C_1, C_2, C_3, C_4, C_5, C_6, C_7, C_8$ can be found in the Appendix C.2.1.

$\dot{X}_j$ and $\dot{Y}_j$ are expressed in matrix form as

$$\begin{bmatrix} \dot{X}_j \\ \dot{Y}_j \end{bmatrix} = \begin{bmatrix} C_1 & C_3 \\ -C_3 & C_1 \end{bmatrix} \begin{bmatrix} X_j \\ Y_j \end{bmatrix} + \begin{bmatrix} C_2 + C_5\cos(2\phi_j) & C_4 \\ -C_4 & C_2 + C_5\cos(2\phi_j) \end{bmatrix} \begin{bmatrix} \sum_{k=1}^{3} X_k \\ \sum_{k=1}^{3} Y_k \end{bmatrix}$$
$$+ \begin{bmatrix} C_6\sin(2\phi_j) + C_7\cos(2\phi_j) + C_8\sum_{k=1}^{3}\cos(2\phi_k) \\ -C_6\cos(2\phi_j) + C_7\sin(2\phi_j) + C_8\sum_{k=1}^{3}\sin(2\phi_k). \end{bmatrix}$$

Specifically for the tuned case, letting $\kappa_{v_j} = 0$, Equations (3.35) and (3.35) becomes

Real part:

$$\dot{X}_j = T_1X_j + T_2\sum_{k=1}^{3} X_k + T_3Y_j + T_4\sum_{k=1}^{3} Y_k + T_5\cos(\phi_j)\sum_{k=1}^{3} X_k + T_6\sin(2\phi_j) + T_7\cos(2\phi_j) + T_8\sum_{k=1}^{3}\cos(2\phi_k) \quad (3.37)$$

Imaginary part:

$$\dot{Y}_j = -T_3X_j - T_4\sum_{k=1}^{3} X_k + T_1Y_j + T_2\sum_{k=1}^{3} Y_k + T_5\sin(\phi_j)\sum_{k=1}^{3} X_k - T_6\cos(2\phi_j) + T_7\sin(2\phi_j) + T_8\sum_{k=1}^{3}\sin(2\phi_k) \quad (3.38)$$

where $T_1, T_2, T_3, T_4, T_5, T_6, T_7, T_8$ can be found in the Appendix C.2.2

$\dot{X}_j$ and $\dot{Y}_j$ are represented in matrix form as

$$\begin{bmatrix} \dot{X}_j \\ \dot{Y}_j \end{bmatrix} = \begin{bmatrix} T_1 & T_3 \\ -T_3 & T_1 \end{bmatrix} \begin{bmatrix} X_j \\ Y_j \end{bmatrix} + \begin{bmatrix} T_2 + T_5\cos(2\phi_j) & T_4 \\ -T_4 & T_2 + T_5\cos(2\phi_j) \end{bmatrix} \begin{bmatrix} \sum_{k=1}^{3} X_k \\ \sum_{k=1}^{3} Y_k \end{bmatrix}$$

$$+ \begin{bmatrix} T_6\sin(2\phi_j) + T_7\cos(2\phi_j) + T_8\sum_{k=1}^{3}(\cos 2\phi_k) \\ -T_6\cos(2\phi_j) + T_7\sin(2\phi_j) + Z_8\sum_{k=1}^{3}(\sin 2\phi_k) \end{bmatrix}$$

Magnitude of steady state response amplitude will be found and amplitude versus frequency plots will be obtained for superharmonic resonance case at order 2. Moreover, we would like to perform numerical simulations to validate the analytical results on the both superharmonic resonances at order 2 and 3.

3.6 Conclusions

In-plane vibration of a coupled three-blade wind turbines were studied. Equations of motion were derived previously. After decoupling the blade equations, a second-order pertubation analysis was applied on both tuned and mistuned three-blade wind turbines.

The analysis brought out the superharmanic resonances at one-third natural frequency. This resonance case could not captured with a first-order method of multiple scales analysis. With mistuning, the superharmonic resonance splits a single resonance peak on the tuned case into multiple resonance peaks. For steady-state superharmonic resonance response, amplitude inceases while damping factor ζ decreases. On the other hand, the response amplitude gets larger when $|\lambda\kappa|$ grows. Observation of mistuning indicates that amplitude of one blade increases compared to the tuned system for $0 < \kappa_v < 0.03$.

Ongoing and future work will address a formulation of the resulting dynamics of the rotor, and the effects of constant loading. Steady state response amplitude will be determenined for superharmonic case at order two and will do numerical simulation to confirm analytical solutions at order two and three. For dynamical interest, we can study the primary and subharmonic resonances as well. The effect of nonlinearity on the resonances is also of interest.

CHAPTER 4

APPROXIMATE GENERAL RESPONSES OF TUNED AND MISTUNED 4-DEGREE-OF-FREEDOM SYSTEMS WITH PARAMETRIC STIFFNESS

4.1 Introduction

We have studied systems with cyclic stiffness and direct excitation. When linearized, these systems have transient and steady-state solutions. We have focused on steady-state behavior with the perturbation analyses. We can consider the transient behavior as the response to the system with cyclic stiffness, but without the direct forcing. To this end, we consider a Floquet-based approach to multi-degree-of-freedom linear systems with cyclic stiffness.

In this work, general solutions to Mathieu-type multi-degree-of-freedom systems of the form

$$\boldsymbol{M}\ddot{\boldsymbol{x}} + \boldsymbol{K}(t)\boldsymbol{x} = \boldsymbol{0}, \tag{4.1}$$

are examined in detail, where $\boldsymbol{x}$ is a $d \times 1$ vector of coordinate displacements, where d is the number of degrees of freedom, and $\boldsymbol{M}$ and $\boldsymbol{K}(t)$ are the mass and time-varying stiffness matrices.

A general initial condition response as well as the stability characteristics of the system is sought. Intending to produce that result, in place of assuming a periodic solution, a Floquet-type solution is assumed as

$$\boldsymbol{x}_j^{(r)} = e^{i\mu_r t} \sum_{k=-n}^{n} \boldsymbol{c}_{j,k}^{(r)} e^{ik\omega t}, \tag{4.2}$$

where the index r distinguishes between $2d$ independent Floquet solution terms for a d-degree-of-freedom system, j presents coordinates and k refers harmonics. As following up the work on approximate general response of symmetric two and three DOF sytems with parametric stiffness, the assumed solution is plugged into the equations of motion, and by applying harmonic balance, the characteristic exponents, μ_r and associated Fourier coefficients, $\boldsymbol{c}^{(r)}$, are determined. Then, by using a procedure that is similar to the one used in [32], the response to an arbitrary initial condition can be determined by considering a linear combination of the $\boldsymbol{x}_r$.

4.2 Analysis

The response analysis procedure can be explained by studying on example MDOF systems, namely tuned and mistuned 4DOF systems. So as to achieve the goal, a mass-spring chain as shown in Figure 4.1, with periodic stiffness is studied.

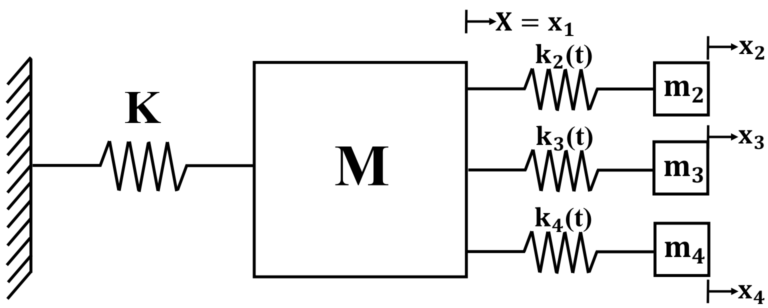

Figure 4.1: A four DOF spring-mass chain.

The equations of motion are

$$\begin{aligned}
\beta\ddot{X} + (3+\gamma+\epsilon)X - (1+\delta\cos[\omega t + \frac{2\pi}{3}])x_2 - (1+\delta\cos[\omega t + \frac{4\pi}{3}])x_3 - (1+\epsilon+\delta\cos[\omega t])x_4 = 0 \\
\ddot{x_2} + (1+\delta\cos[\omega t + \frac{2\pi}{3}])(x_2 - X) = 0 \\
\ddot{x_3} + (1+\delta\cos[\omega t + \frac{4\pi}{3}])(x_3 - X) = 0 \\
\ddot{x_4} + (1+\epsilon+\delta\cos[\omega t])(x_4 - X) = 0.
\end{aligned} \tag{4.3}$$

where $m_2 = m_3 = m_4 = 1$, $M = \beta m_2$, $K = \gamma$ and $k_i(t) = (1 + \epsilon_i + \delta\cos[\omega t + (2\pi/3)(i)])$, where $i = 2, 3, 4$, $\epsilon_2 = \epsilon_3 = 0$ and $\epsilon_4 = \epsilon$. For specific parameter values, the eigenvalues are plotted as a function of stiffness mistuning parameter (ϵ) as shown in Figure 4.2. When $\delta = 0$ and the system is tuned ($\epsilon = 0$) modal frequencies are $\omega_1 = 0.3047$, $\omega_2 = 1$, $\omega_3 = 1$ and $\omega_4 = 2.075$. Figure

4.3 shows both tuned ($\epsilon = 0$) and mistuned systems space ($\epsilon = 1$) mode shapes in same plot to demonstrate the effect of detuning parameter on the mode shapes.

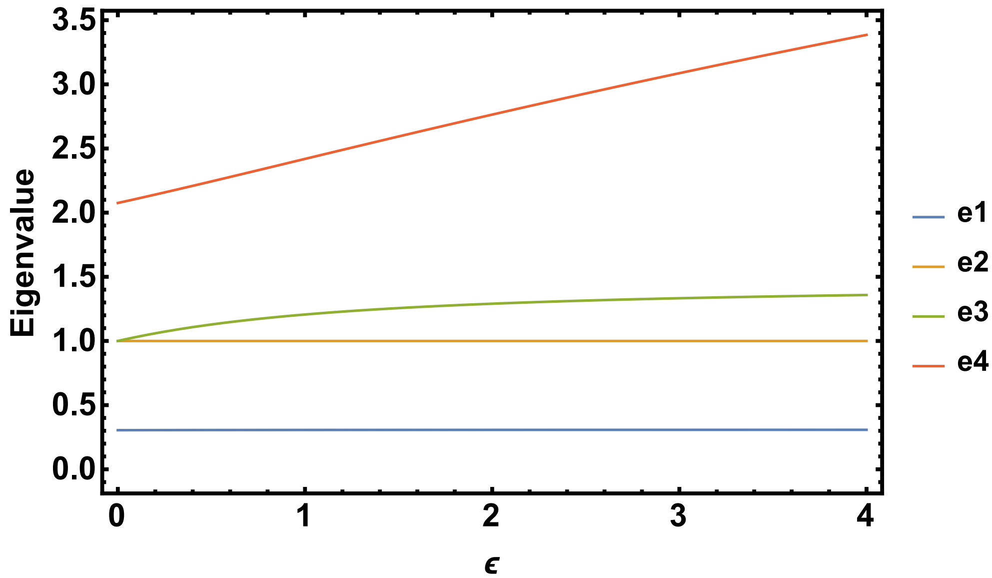

Figure 4.2: Eigenvalues versus stiffness mistuning parameter ϵ for $\delta = 0$, $\omega = 1.6$, $m_2 = m_3 = m_4 = \beta = 1$, $\gamma = 0.4$

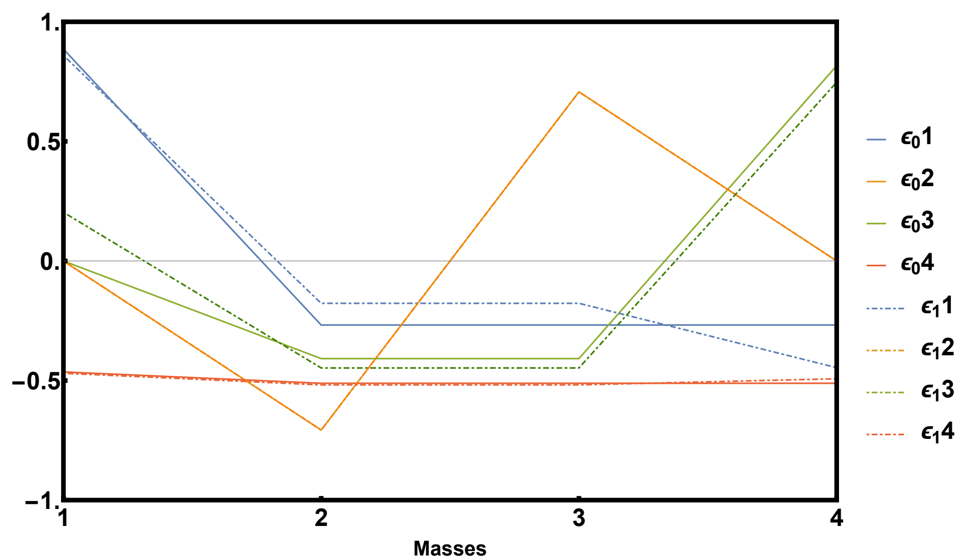

Figure 4.3: Mode shapes of the tuned ($\epsilon = 0$) and mistuned ($\epsilon = 1$) systems

4.2.1 Tuned Four-Degree-of-Freedom Example

Following the reference [32], the response is found by assuming a Floquet type solution with finite harmonics, as given in Equation (4.2) and inserting into the system equations of motion. Particularly, in this model, we seek for

$$
\begin{aligned}
x_1(t) &= e^{i\mu t} \sum_{k=-n}^{n} c_{1,k} e^{ik\omega t} \\
x_2(t) &= e^{i\mu t} \sum_{k=-n}^{n} c_{2,k} e^{ik\omega t} \\
x_3(t) &= e^{i\mu t} \sum_{k=-n}^{n} c_{3,k} e^{ik\omega t} \\
x_4(t) &= e^{i\mu t} \sum_{k=-n}^{n} c_{4,k} e^{ik\omega t}.
\end{aligned}
$$

Governing equations for $c_{j,k}$'s are determined by using harmonic balance and writing the harmonic balance equation in matrix form,

$$
\mathbf{A}\boldsymbol{c} = \begin{bmatrix} \boldsymbol{A}_{11} & \boldsymbol{A}_{12} & \boldsymbol{A}_{13} & \boldsymbol{A}_{14} \\ \boldsymbol{A}_{21} & \boldsymbol{A}_{22} & \boldsymbol{A}_{23} & \boldsymbol{A}_{24} \\ \boldsymbol{A}_{31} & \boldsymbol{A}_{32} & \boldsymbol{A}_{33} & \boldsymbol{A}_{34} \\ \boldsymbol{A}_{41} & \boldsymbol{A}_{42} & \boldsymbol{A}_{43} & \boldsymbol{A}_{44} \end{bmatrix} \begin{pmatrix} \boldsymbol{c}_1 \\ \boldsymbol{c}_2 \\ \boldsymbol{c}_3 \\ \boldsymbol{c}_4 \end{pmatrix} = \begin{pmatrix} \mathbf{0} \\ \mathbf{0} \\ \mathbf{0} \\ \mathbf{0} \end{pmatrix}, \tag{4.4}
$$

where $\boldsymbol{c}_j = [c_{j,-n} \dots c_{j,-1} \quad c_{j,0} \quad c_{j,1} \dots c_{j,n}]^T$, and A_{ij}'s correspond to $(2n+1) \times (2n+1)$ block matrices.

The determinant of the coefficient matrix, $\boldsymbol{A}(\mu)$, must be equal to zero to own a nonzero $\boldsymbol{c}$ solution. We can find the characteristic equation for μ in terms of δ, γ, ω and $m_1 = m_2 = m_3 = \beta$. Then, for each μ, we can obtain the $\boldsymbol{c}$ vector, by solving $\boldsymbol{A}(\mu)\boldsymbol{c} = \mathbf{0}$. The characteristic equation produce roots μ_q, where q is from 1 to $2d(2n+1)$ and d is number of degrees of freedom, n is the number of assumed harmonics. Nevertheless, there are essentially $2d$ principal roots, and the other $\mu's$ are linked to the principal roots by the relation $\hat{\mu}_s = \hat{\mu}_r \pm k\omega i$. Since the corresponding exponential part can be written as $e^{i\mu_r t} e^{ik\omega t}$ and the second part can be inserted into the periodic part, it is observed that these roots do not conduce to extra solutions.

As following up the work on 2-DOF and 3-DOF mass-spring chain examples [32], μ_qs are plugged into the coefficient matrix, then null space of $\boldsymbol{A}(\mu_q)$ provides the solution of $\boldsymbol{c}^{(q)}$'s.

The idea about the stability and the frequency subject of the solution can be obtained by the roots of the characteristic equation. Even if only one of the roots has a negative imaginary part, the solution will grow unstable because of the exponential part. If all roots have a positive imaginary part, the solution is bounded. Particularly, if the roots are real, the solution is either periodic or quasi-periodic. In Figure 4.4, the stability regions for the 4DOF mass-spring chain are drawn by evaluating the imaginary parts of the characteristic roots for $\gamma = 1$, $\beta = 1$.

The frequency values can be determined with combination of the exponential and the periodic parts of the frequencies as $|Re(\mu_r) \pm k\omega|$. In 4DOF system, there are eight principal characteristic roots and the general response solution is written in terms of "modal components" as

$$\boldsymbol{x}(t) = \sum_{r=1}^{8} a_r \boldsymbol{x}^r(t), \tag{4.5}$$

where

$$\boldsymbol{x}^r = \begin{bmatrix} x_1^{(r)} \\ x_2^{(r)} \\ x_3^{(r)} \\ x_4^{(r)} \end{bmatrix} \tag{4.6}$$

a_r's are to be determined from the initial conditions. Arbitrary initial conditions can be defined as a class of linear equations in terms of the constants a_r, as

$$\begin{bmatrix} \boldsymbol{x}_0 \\ \dot{\boldsymbol{x}}_0 \end{bmatrix} = \begin{bmatrix} \boldsymbol{x}^1(0) & \dots & \boldsymbol{x}^8(0) \\ \dot{\boldsymbol{x}}^1(0) & \dots & \dot{\boldsymbol{x}}^8(0) \end{bmatrix} \begin{bmatrix} a_1 \\ \vdots \\ a_8 \end{bmatrix}. \tag{4.7}$$

As stated the in previous study [32], the initial condition $\begin{bmatrix} \boldsymbol{x}_0^T & \dot{\boldsymbol{x}}_0^T \end{bmatrix}^T = \begin{bmatrix} \boldsymbol{x}^s(0)^T & \dot{\boldsymbol{x}}^s(0)^T \end{bmatrix}^T$ results in $a_s = 1$ and $a_{r \neq s} = 0$. Consequently, the different modal functions can be obtained if a scalar multiple of each column can be used as an initial condition. Accordingly, the response can be determined as the same linear combination of the corresponding modal functions by writing an initial condition as a linear combination of $\left[\boldsymbol{x}^s(0)^T \quad \dot{\boldsymbol{x}}^s(0)^T\right]^T$'s.

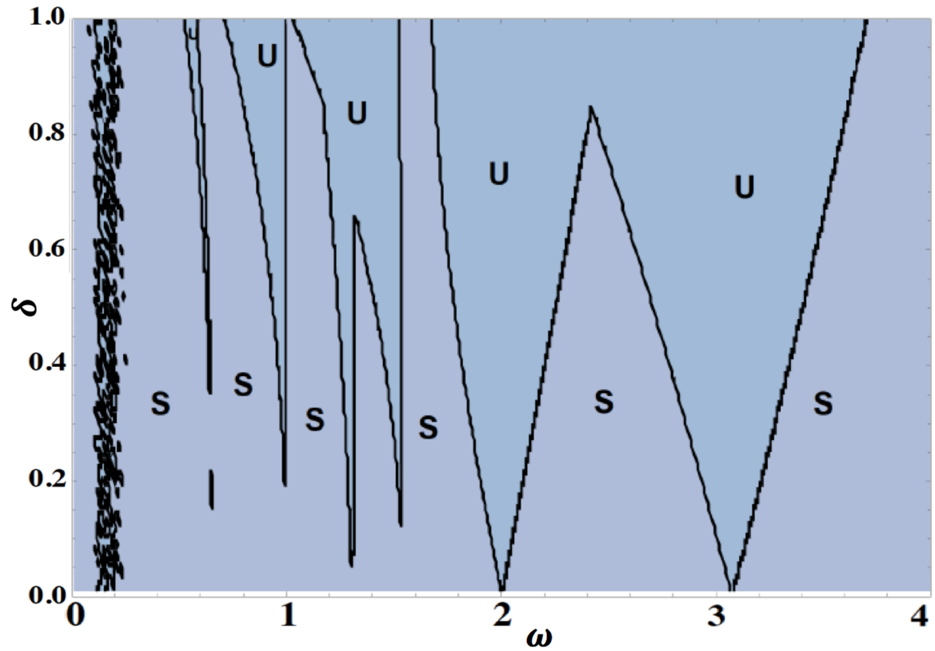

Figure 4.4: Stability regions for the tuned 4 DOF mass-spring chain for $n = 2$, $\beta = 1$ and $\gamma = 0.4$

The response frequency is a combination of frequencies of the exponential and periodic parts as $|\mathrm{Re}(\mu_r) \pm k\omega|$. For a set of parameters, the response frequencies as a function of excitation frequency are given in Figure 4.5 for one harmonic. Two frequency branches collide and constitute one branch with variations in ω. This collisions stand for stability transitions. Also, the branches are overlap because of the repeated frequencies on the tuned case. The top branch does not merge with any branch in Figure 4.5. We can predict to see more branches in response frequencies plot with higher harmonics, thus the top branch can collide.

The 4DOF spring-mass chain was studied with $n = 2$ harmonics, for various sets of parameters and initial conditions. The results were compared to those determined from a numerical work, and the initial condition response and FFT plots were given in Figure 4.6 and Figure 4.7 for $\delta = 0.2$ and in Figure 4.8 and Figure 4.9 for $\delta = 0.6$.

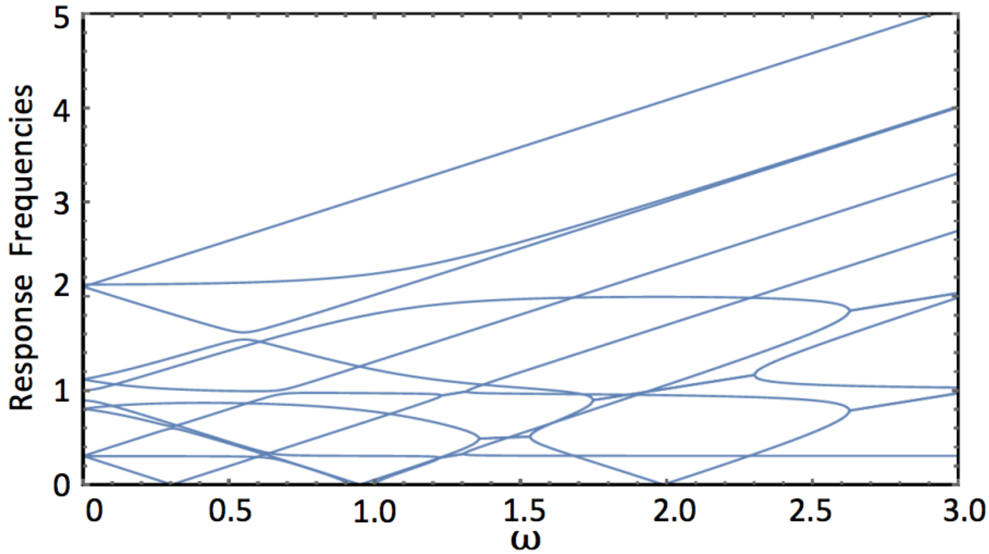

Figure 4.5: Response frequencies plot as a function of excitation frequency with parameters $n = 1$, $\epsilon = 0$, $\gamma = 0.4$, $\beta = 1$ and $\delta = 0.6$.

4.2.2 Mistuned Four-Degree-of-Freedom Example

Instead of assuming a perfectly tuned model, the stiffness term $k_4(t)$ is assumed to have a variation ϵ, such that $k_4(t) = (1 + \epsilon + \delta \cos[\omega t + (2\pi)])$.

Following up the work on tuned system, general solution Equation (4.2) is inserted into Equation (4.3) and same steps are applied. Then, characteristic exponents and corresponding eigenvectors are obtained. The stability wedges of the 4DOF system are plotted by examining the imaginary parts of the characteristic exponents for one harmonic and $\gamma = 0.4$, $\beta = 1$, $\epsilon = 0.2$ in Figure 4.10 and for two harmonics and $\gamma = 0.4$, $\beta = 1$, $\epsilon = 1$ in Figure 4.11.

Figure 4.12 shows the response frequencies as function of ω for mistuned system. Repsonse frequency plots look very similar for tuned and mistuned cases, but we can get some fine details, the places where repeated frequency components are split up little bit. Symmetry breaking seperates repeated frequencies and combination of frequencies get little bit more complicated on detuned case.

FFT plots and the initial condition responses were found assuming $n = 2$ harmonics and detuning term $\epsilon = 0.2$, for different sets of parameters, and were compared to those obtained from a numerical study, as given in Figures 4.13 and 4.14 for $\delta = 0.2$ and Figures 4.15 and 4.16 for

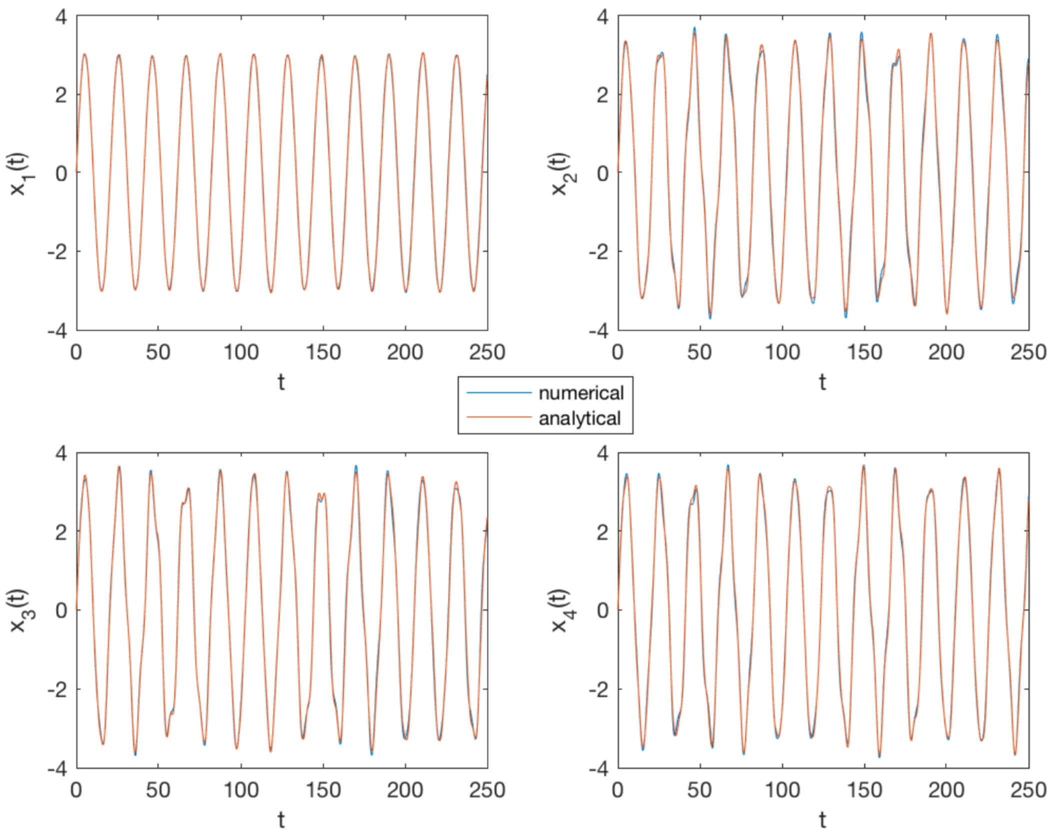

Figure 4.6: Response plots for $n = 2$, $\omega = 0.75$, $\delta = 0.2$, $\epsilon = 0$, $\gamma = 0.4$, $\boldsymbol{x}(0) = [0 \quad 0 \quad 0 \quad 0]^T$ and $\dot{\boldsymbol{x}}(0) = [1 \quad 1 \quad 1 \quad 1]^T$.

$\delta = 0.6$.

4.3 Discussion

The instability wedges in Figure 4.4 may be based at $\omega = (\omega_i + \omega_j)/N$, where N is a positive integer. In the tuned 4DOF system for $\beta = 1$ and $\gamma = 0.4$, the $\delta = 0$ natural frequencies were $\omega_1 = 0.3047$, $\omega_2 = \omega_3 = 1$ and $\omega_4 = 2.075$. We observe the two main subharmonic instability wedges starting at frequencies $\omega \cong \omega_2 + \omega_3 = 2$, $\omega \cong \omega_1 + \omega_{2,3} = 1.305$ and $\omega \cong \omega_{2,3} + \omega_4 = 3.07$. Additionally, if there is a wedge at $2\omega_4 = 4.15$, it is not in the domain of Figure 4.4. Some primary and superharmonic wedges originate at frequencies that fit into the pattern, such as $\omega_2 = \omega_3 = 1$, $(\omega_1 + \omega_2)/2 = (\omega_1 + \omega_3)/2 = 0.65$, $\omega_1 = 0.304$, $(\omega_2 + \omega_4)/2 = (\omega_3 + \omega_4)/2 = 1.537$ and $\omega_4/2 = 1.035$. Simulations were done for different parameter values to confirm the compatibility. For instance, at $\delta = 0.8$ and $\omega = 1.1$ the simulation was unstable, although at $\omega = 1.6$ the simulation

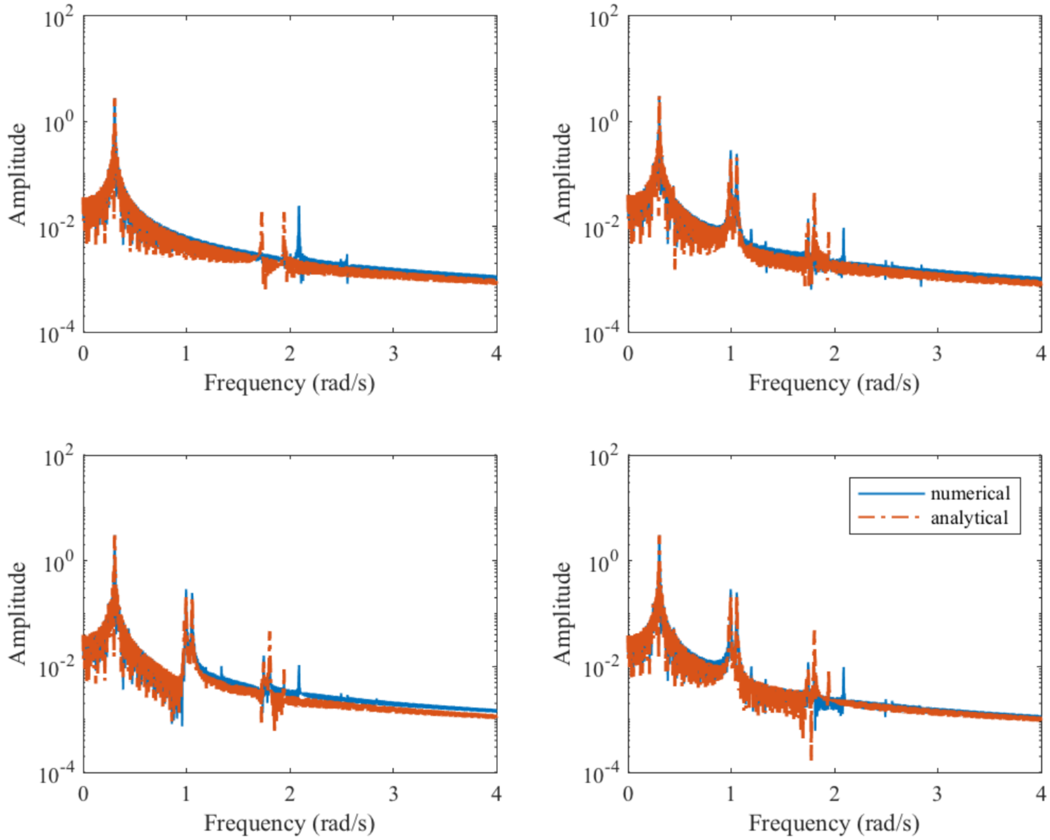

Figure 4.7: FFT plots for $n = 2$, $\omega = 0.75$, $\delta = 0.2$, $\epsilon = 0$, $\gamma = 0.4$, $\boldsymbol{x}(0) = [0 \quad 0 \quad 0 \quad 0]^T$ and $\dot{\boldsymbol{x}}(0) = [1 \quad 1 \quad 1 \quad 1]^T$.

was stable, in agreement with the stability region in Figure 4.4. A spurious instability feature near $\omega = 0.15$ was displayed in Figure 4.4. Similar trends were observed from simulations of the four-DOF system with different values of γ which is not shown here.

The detuned 4DOF system for $\epsilon = 1$, $\beta = 1$ and $\gamma = 0.4$, the natural frequencies were $\omega_1 = 0.3065$, $\omega_2 = 1$ $\omega_3 = 1.206$ and $\omega_4 = 2.4188$. We see the wedges at $2\omega_1 \cong 0.604$, $2\omega_2 \cong 2$, $2\omega_3 \cong 2.41$, $\omega_1 + \omega_2 \cong 1.306$, $\omega_1 + \omega_3 \cong 1.512$, $\omega_2 + \omega_3 \cong 2.206$, $\omega_2 + \omega_4 \cong 3.418$, $\omega_1 + \omega_4 \cong 2.713$, $\omega_3 + \omega_4 \cong 3.616$ and $2\omega_4 \cong 4.84$ showing the subharmonic instabilities of each “mode". Some primary and superharmonic wedges are also based at frequencies which match the pattern, such as $\omega_2 = 1$, $\omega_3 = 1.206$, $\omega_4 = 2.418$, $(\omega_2 + \omega_3)/2 = 1.103$, $(\omega_1 + \omega_2)/2 = 0.605$, $(\omega_1 + \omega_4)/2 = 1.36$, $(\omega_1 + \omega_3)/2 = 0.751$, $(\omega_2 + \omega_4)/2 = 1.712$ and $(\omega_3 + \omega_4)/2 = 1.81$. In Table 4.1, some instability wedges for tuned case with one harmonic and mistuned blade case with

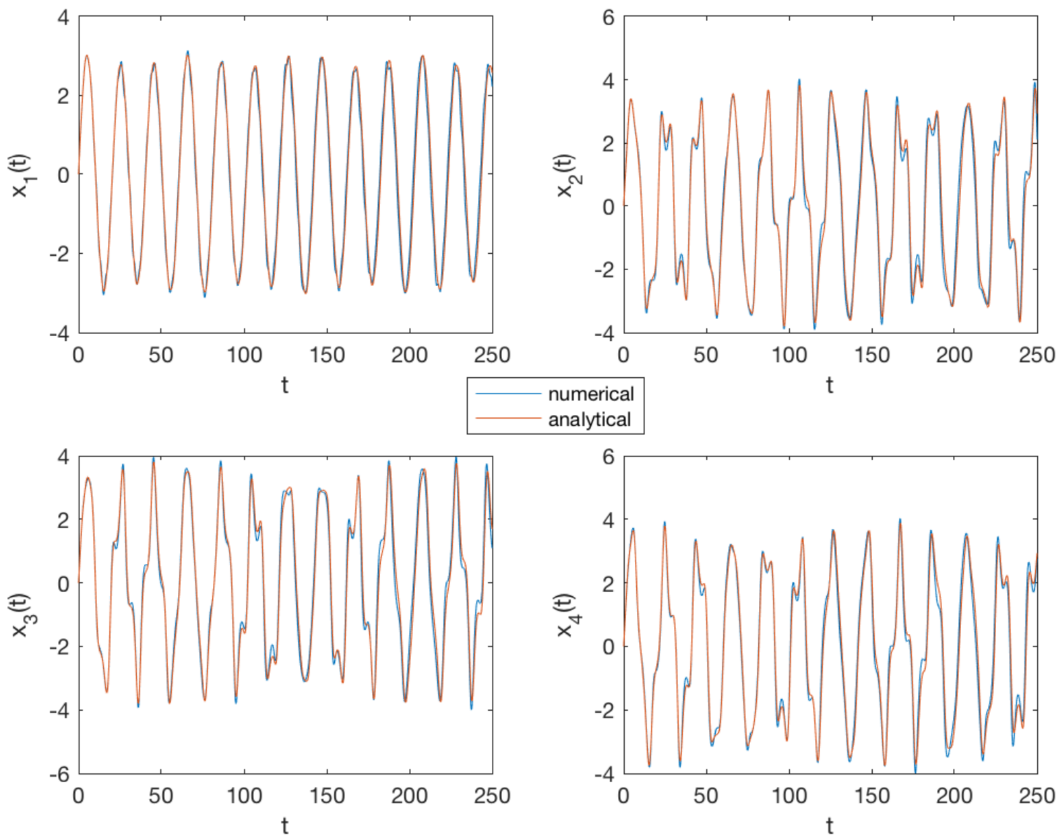

Figure 4.8: Response plots for $n = 2$, $\omega = 0.75$, $\delta = 0.6$, $\epsilon = 0$, $\gamma = 0.4$, $\boldsymbol{x}(0) = [0 \quad 0 \quad 0 \quad 0]^T$ and $\dot{\boldsymbol{x}}(0) = [1 \quad 1 \quad 1 \quad 1]^T$.

one and two harmonics were demonstrated. Comparing the tuned and mistuned stability plots, the mistuned system has many more instability wedges, and generally depicts a greater tendency to destabilize.

According to the Floquet solution, which involves a linear combination of terms $e^{i\mu t}\boldsymbol{p}(t)$, it is clear that initial conditions can be specified such that only one of the these terms is active. In this respect, we name them “modal responses". Analytical and numerical free responses are pointed out in Figures 4.13-4.16, for $n = 2$, for the chosen parameters and initial conditions. The time responses showed good agreement. Around 8-10 response harmonics were predicted, mostly accurately, with a couple instances of low amplitude spurious harmonics. Some higher frequency harmonics were not captured analytically with $n = 2$.

The work shown here involves the solution to a nonstandard eigenvalue problem in the form

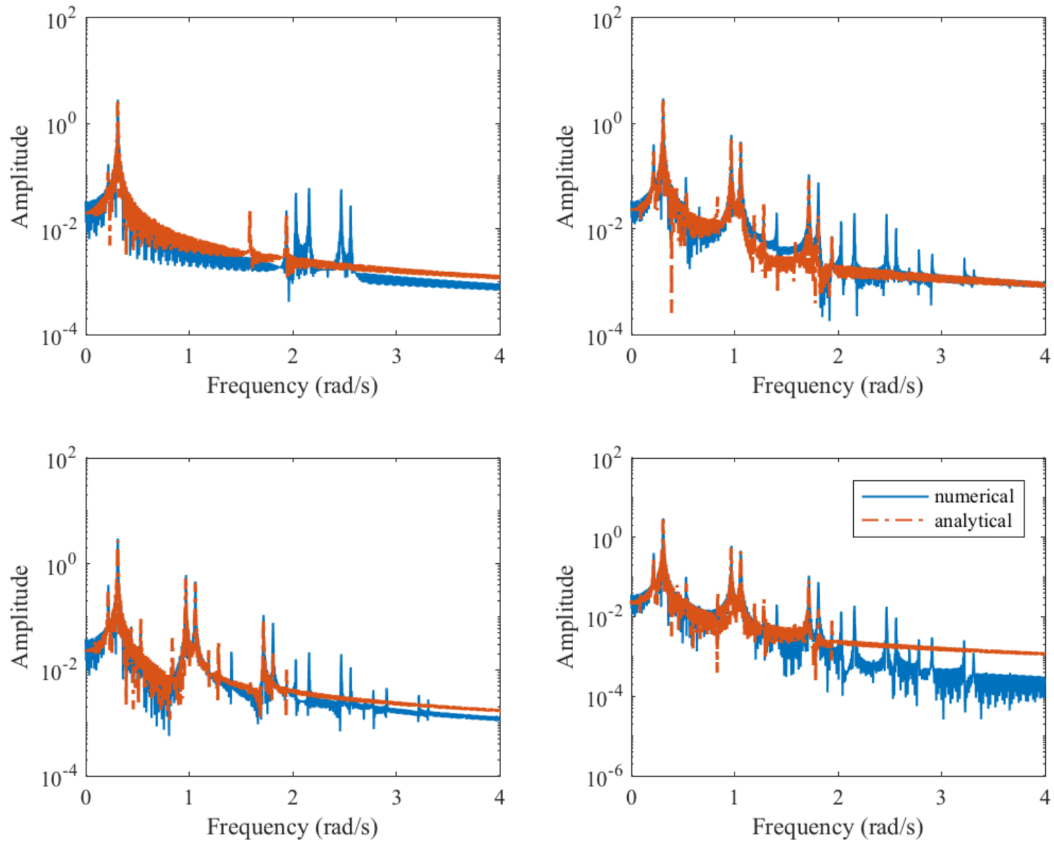

Figure 4.9: FFT plots for $n = 2$, $\omega = 0.75$, $\delta = 0.6$, $\epsilon = 0$, $\gamma = 0.4$, $\boldsymbol{x}(0) = [0 \quad 0 \quad 0 \quad 0]^T$ and $\dot{\boldsymbol{x}}(0) = [1 \quad 1 \quad 1 \quad 1]^T$.

of Equation (4.4) in which matrix $\boldsymbol{A}$ has elements with μ^2 terms. The characteristic equation is polynomial of degree $2d(2n + 1)$ in μ. As the number of harmonics, n, increases there may be computational limits on finding symbolic solutions for the μ. Despite this, $n = 2$ harmonics were able to effectively predict the response for the systems studied in this study.

4.4 Conclusions

General responses of a 4 DOF mass-spring system with parametric excitation were studied. Assuming a Floquet-type solution, and applying the harmonic balance method, the frequency content and stability of the solution were found. Later, the analysis was extended to a system with mistuned parameters, and the effect of symmetry breaking on system response was studied. In addition, the time response and FFT plots were produced for various parameters and initial conditions in the both tuned and mistuned case. Then, analytical results were confirmed by

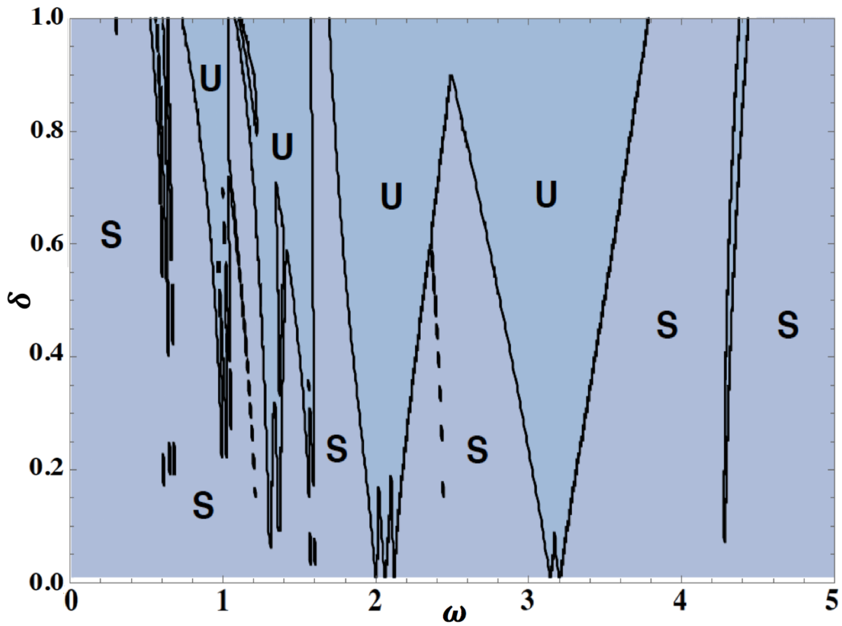

Figure 4.10: Stability plot of the mistuned 4 DOF system for $n = 1$, $\epsilon = 0.2$, $\beta = 1$ and $\gamma = 0.4$

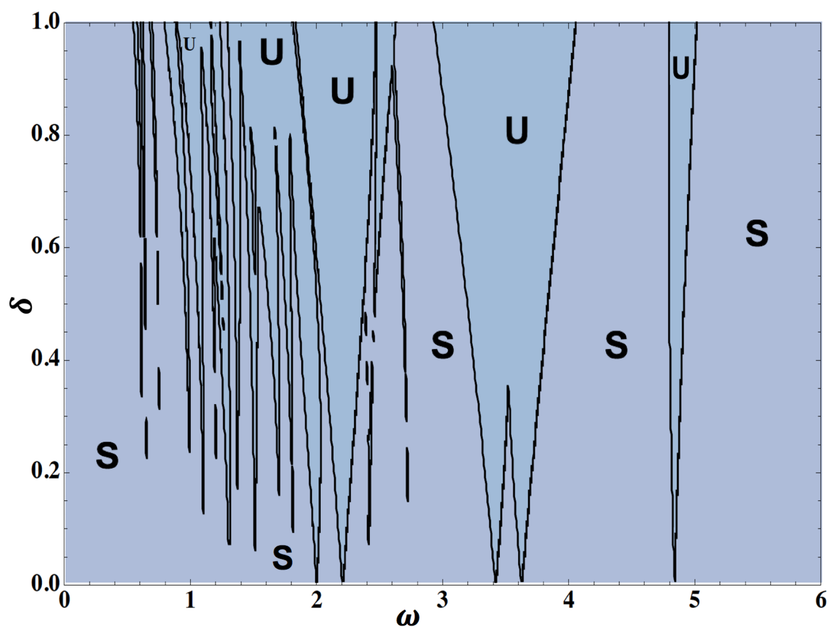

Figure 4.11: Stability plot for the mistuned 4 DOF system for $n = 2$, $\epsilon = 1$, $\beta = 1$ and $\gamma = 0.4$

numerical simulations. In future work, this method will be applied on mistuned three-blade wind turbine models to find the response characteristics.

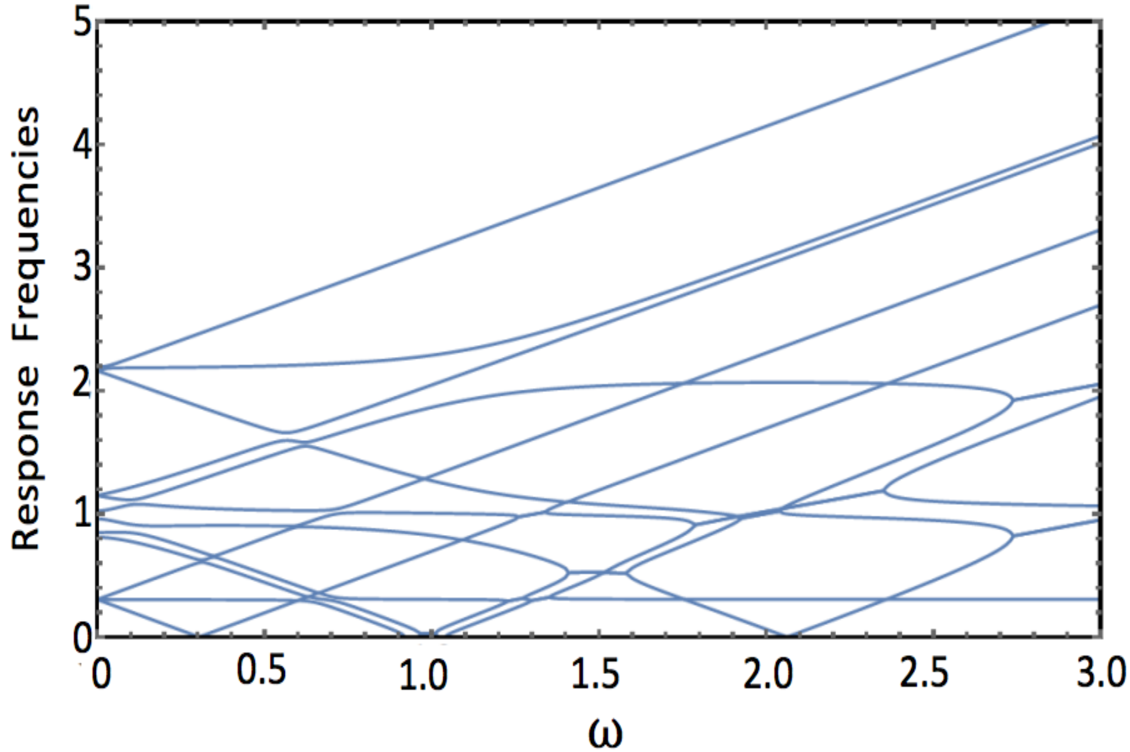

Figure 4.12: Response frequency plot as a function of excitation frequency for mistuned case with parameters $n = 1$, $\epsilon = 0.2$, $\gamma = 0.4$, $\beta = 1$ and $\delta = 0.6$.

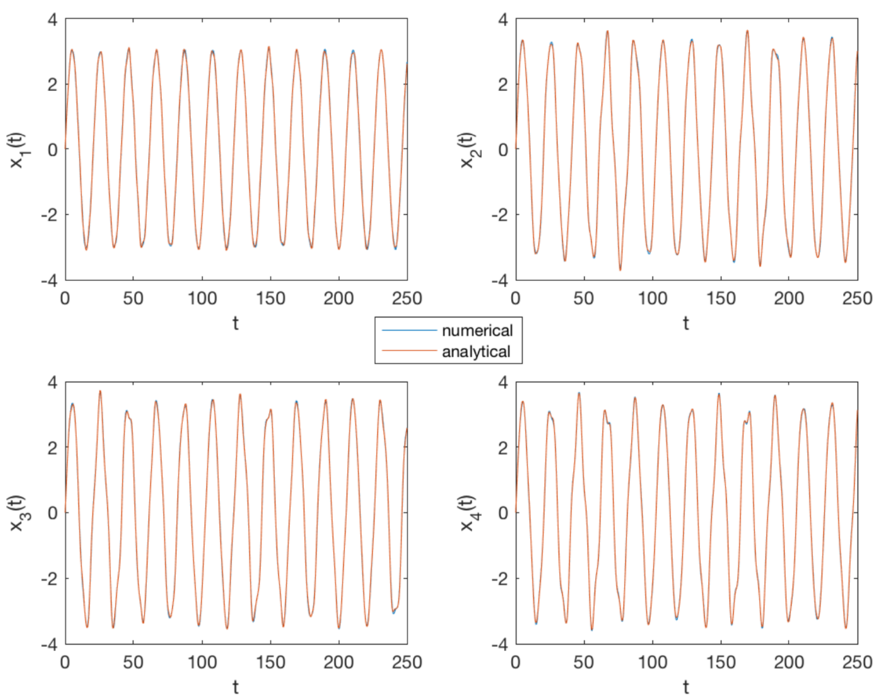

Figure 4.13: Response plots of detuned system for $n = 2$, $\epsilon = 0.2$, $\omega = 0.8$, $\delta = 0.2$, $\gamma = 0.4$, $\boldsymbol{x}(0) = [0 \quad 0 \quad 0 \quad 0]^T$ and $\dot{\boldsymbol{x}}(0) = [1 \quad 1 \quad 1 \quad 1]^T$.

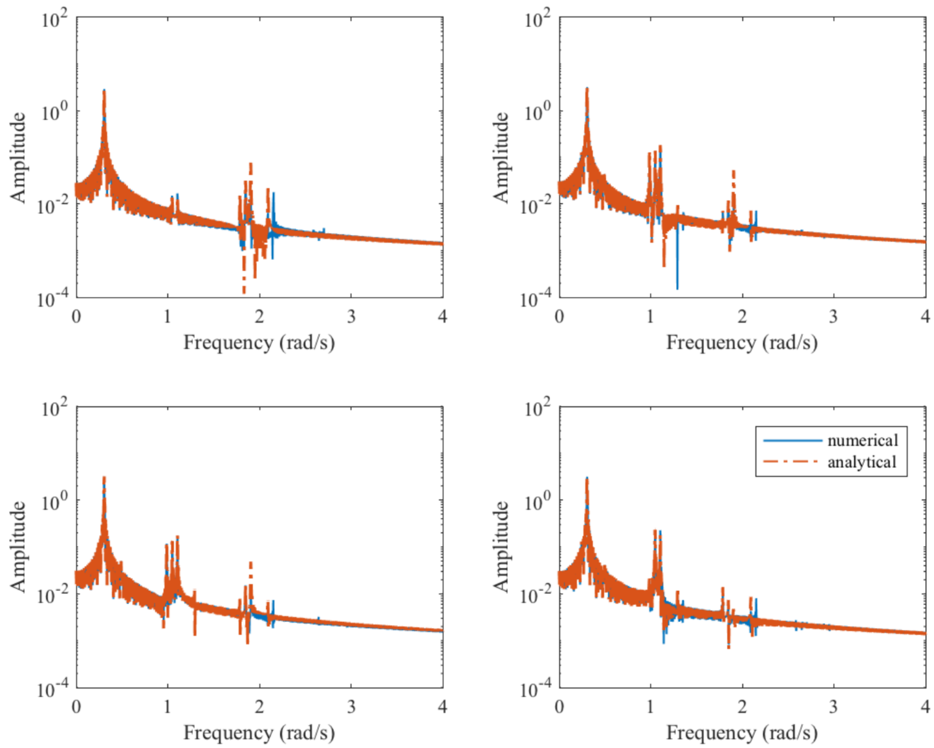

Figure 4.14: FFT plots of detuned system for $n = 2$, $\epsilon = 0.2$, $\omega = 0.8$, $\delta = 0.2$, $\gamma = 0.4$, $\boldsymbol{x}(0) = [0 \quad 0 \quad 0 \quad 0]^T$ and $\dot{\boldsymbol{x}}(0) = [1 \quad 1 \quad 1 \quad 1]^T$.

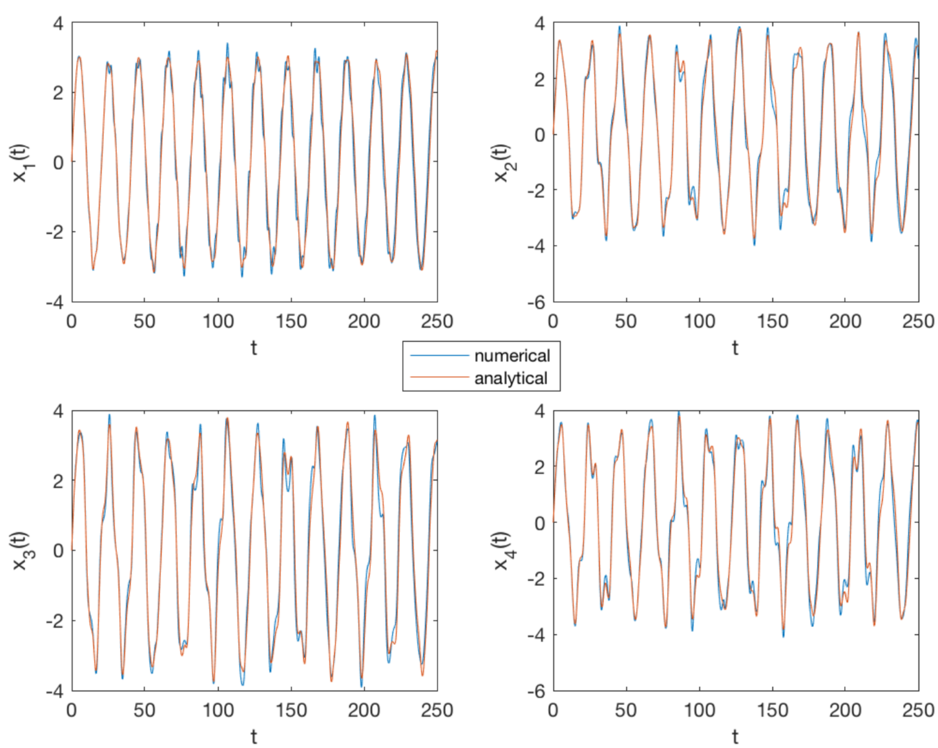

Figure 4.15: Response plots of detuned system for $n = 2$, $\epsilon = 0.2$, $\omega = 0.8$, $\delta = 0.6$, $\gamma = 0.4$, $\boldsymbol{x}(0) = [0 \quad 0 \quad 0 \quad 0]^T$ and $\dot{\boldsymbol{x}}(0) = [1 \quad 1 \quad 1 \quad 1]^T$.

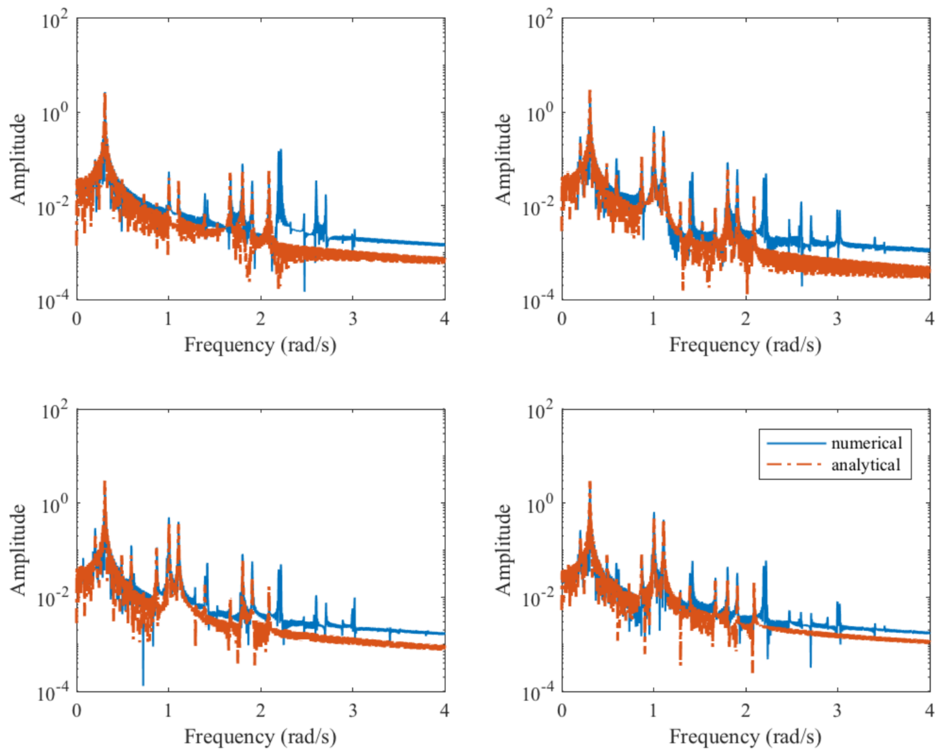

Figure 4.16: FFT plots of detuned system for $n = 2$, $\epsilon = 0.2$, $\omega = 0.8$, $\delta = 0.6$, $\gamma = 0.4$, $\boldsymbol{x}(0) = [0 \quad 0 \quad 0 \quad 0]^T$ and $\dot{\boldsymbol{x}}(0) = [1 \quad 1 \quad 1 \quad 1]^T$.

Table 4.1: Primary, superharmonic and subharmonic instability wedges based at $\frac{\omega_i+\omega_j}{N}$ for tuned and mistuned cases

	Primary	Superharmonic	Subharmonic
Tuned Case $(n = 2, \epsilon = 0)$ $\omega_1 = 0.3047$, $\omega_{2,3} = 1$, $\omega_4 = 2.075$	ω_1 ω_2 ω_3	$\frac{\omega_1+\omega_2}{2}$, $\frac{\omega_1+\omega_3}{2}$ $\frac{\omega_2+\omega_4}{2}$, $\frac{\omega_3+\omega_4}{2}$, $\frac{\omega_4}{2}$	$(\omega_1+\omega_2)$, $(\omega_1+\omega_3)$ $(\omega_2+\omega_3)$, $(\omega_2+\omega_4)$ $(\omega_3+\omega_4)$, $2\omega_4$
Mistuned Case $(n = 2, \epsilon = 1)$ $\omega_1 = 0.3065$, $\omega_2 = 1$, $\omega_3 = 1.206$, $\omega_4 = 2.4188$	ω_2 ω_3 ω_4	$\frac{\omega_1+\omega_2}{2}$, $\frac{\omega_1+\omega_3}{2}$, $\frac{\omega_2+\omega_4}{2}$ $\frac{\omega_3+\omega_4}{2}$, $\frac{\omega_1+\omega_4}{2}$, $\frac{\omega_2+\omega_3}{2}$	$2\omega_1$, $2\omega_2$, $2\omega_3$ $2\omega_4$ $(\omega_1+\omega_2)$, $(\omega_1+\omega_3)$ $(\omega_2+\omega_3)$, $(\omega_2+\omega_4)$ $(\omega_3+\omega_4)$, $(\omega_1+\omega_4)$
Mistuned Case $(n = 1, \epsilon = 0.2)$ $\omega_1 = 0.3053$, $\omega_2 = 1$, $\omega_3 = 1.059$, $\omega_4 = 2.1409$	ω_1 ω_2 ω_3 ω_4	$\frac{\omega_1+\omega_2}{2}$, $\frac{\omega_1+\omega_3}{2}$, $\frac{\omega_2+\omega_4}{2}$ $\frac{\omega_3+\omega_4}{2}$, $\frac{\omega_2+\omega_3}{2}$, $\frac{\omega_4}{2}$	$2\omega_1$, $2\omega_2$, $2\omega_3$, $2\omega_4$ $(\omega_1+\omega_2)$, $(\omega_1+\omega_3)$ $(\omega_2+\omega_3)$, $(\omega_2+\omega_4)$ $(\omega_3+\omega_4)$, $(\omega_1+\omega_4)$

CHAPTER 5

ONGOING WORK

5.1 Parametric Identification of The Mathieu Equation with a Constant Load

5.1.1 Introduction and Objective

Studies on parametrically excited systems have many applications, including ship dynamics, wind-turbine-blade vibration, and micro resonators. This study regards a linear Mathieu equation with a constant force term:

$$\ddot{q} + 2\epsilon\mu\dot{q} + (\omega^2 + \epsilon\gamma\cos\Omega t)q = F_0 \tag{5.1}$$

The wind turbine blade models include cyclic stiffness and constant-plus-cyclic direct loading, in the form of a forced Mathieu equation. It would be interesting to consider parameter estimation in the Mathieu system. The unforced, damped Mathieu system has a zero solution that is either stable or unstable, while the forced Mathieu systems have non-zero steady-state oscillations, which can be stable or unstable. We consider exploiting the steady-state response of a forced Mathieu system to estimate the parameters, namely the strength of parametric excitation, damping, and excitation level. Much attention has been given to the response and stability analysis of the Mathieu equation, for example by perturbation techniques such as the method of multiple scales. In this work we aim to estimate parameters μ, γ and F_0 from responses.

5.1.2 Background

The solution of the fored linear Mathieu equation can be expressed as a sum of homogeneous and particular solutions, given as $q = q_h + q_p$, where q_h satisfies $\ddot{q}_h + 2\epsilon\mu\dot{q}_h + (\omega^2 + \epsilon\gamma\cos\Omega t)q_h = 0$ and q_p satisfies $\ddot{q}_p + 2\epsilon\mu\dot{q}_p + (\omega^2 + \epsilon\gamma\cos\Omega t)q_p = F_0$. From the Floquet theory, the q_h term has the various instabilities that originate due to parametric excitation. The q_p part has been

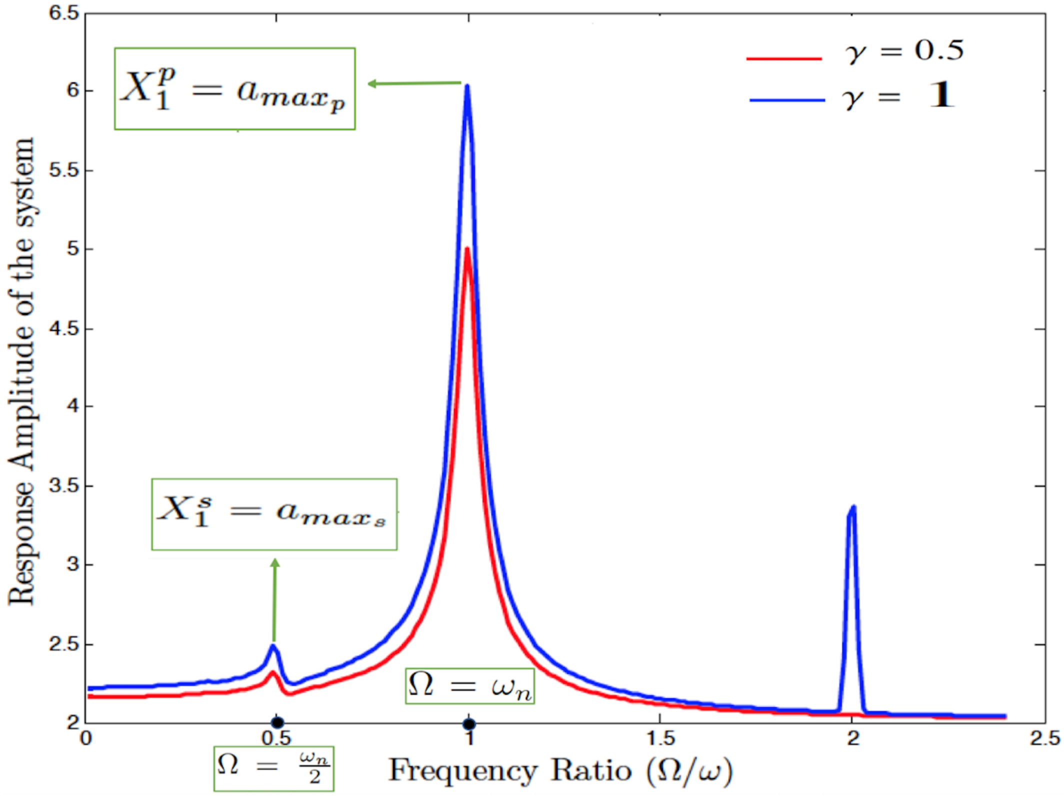

Figure 5.1: Amplitudes of simulated responses of Equation (5.1) showing primary and superharmonic resonances and an unstable response at subharmonic resonance due to increase of the parametric forcing amplitude; $\epsilon = 0.1, \mu = 0.25, F_0 = 2$. Different curves depict $\gamma = 0.5$ and 1. (Figure taken from [1]).

approximated by perturbation techniques, and can have resonance conditions as well as instabilities [1]. Figure 5.1 shows steady-state forced-response amplitudes as a function of the parametric frequency Ω, and illustrates that the system of Equation (5.1) can have primary and secondary resonances and instabilities.

In [1], a second-order multiple scales analysis was applied to find expressions for response amplitudes at primary and superharmonic resonance conditions as a function of system parameters. Perturbation analysis is "valid" for "small" ϵ. Predictions deteriorate when $\epsilon\gamma$ becomes "large". Special steady-state solutions are approximated below.

1. Low frequency limit: a quasi-static approximation is made by letting $\dot{q} \cong 0$ and $\ddot{q} \cong 0$ in

Equation (5.1) and solving for q:

$$q = \frac{F_0}{{\omega_n}^2 + \epsilon\gamma\cos\Omega t} \cong \frac{F_0}{{\omega_n}^2} - \frac{F_0}{{\omega_n}^2}\epsilon\gamma\cos\Omega t$$

which oscillates with a mean, maximum, and minimum values of $\bar{q} \cong \frac{F_0}{{\omega_n}^2}$, $q_{max} \cong \frac{F_0}{{\omega_n}^2 - \epsilon\gamma}$, $q_{min} \cong \frac{F_0}{{\omega_n}^2 + \epsilon\gamma}$.

2. Superharmonic resonance of order 2: If $\Omega \cong \omega_n/2$, then the response is

$$q \cong \frac{F_0}{{\omega_n}^2} + a\cos(2\Omega t - \phi) \pm \frac{\epsilon F_0\gamma}{\omega_n^2(\omega_n^2 - \Omega^2)}\cos(\Omega t) + O(\epsilon^2)$$

with a peak value of a as $a_{max_s} = \frac{\epsilon F_0\gamma^2}{3\mu\omega_n^5}$.

3. Primary resonance: If $\Omega \cong \omega_n$, then the response is

$$q \cong \frac{F_0}{{\omega_n}^2} + a\cos(\Omega t - \phi) + \frac{\epsilon\gamma a\cos\left[(\omega_n + \Omega)t + \beta\right]}{2(\Omega^2 + 2\omega_n\Omega)} + \frac{\epsilon a}{\omega_n^2}\cos\left(\epsilon\sigma t + \beta\right)$$

with a peak value of as $a_{max_p} = \frac{F_0\gamma}{2\mu\omega_n^3}$

5.1.3 Parameter Estimation Procedure

We follow an idea by Nayfeh [62], in which expressions for resonant responses and bifurcation points from perturbation analyses were compared to simulated or experimental measurements of these events in order to estimate parameters in a differential equation model. We do as follows.

1. We estimate ω_n from the peaks of a frequency sweep such as that in Figure 5.1.

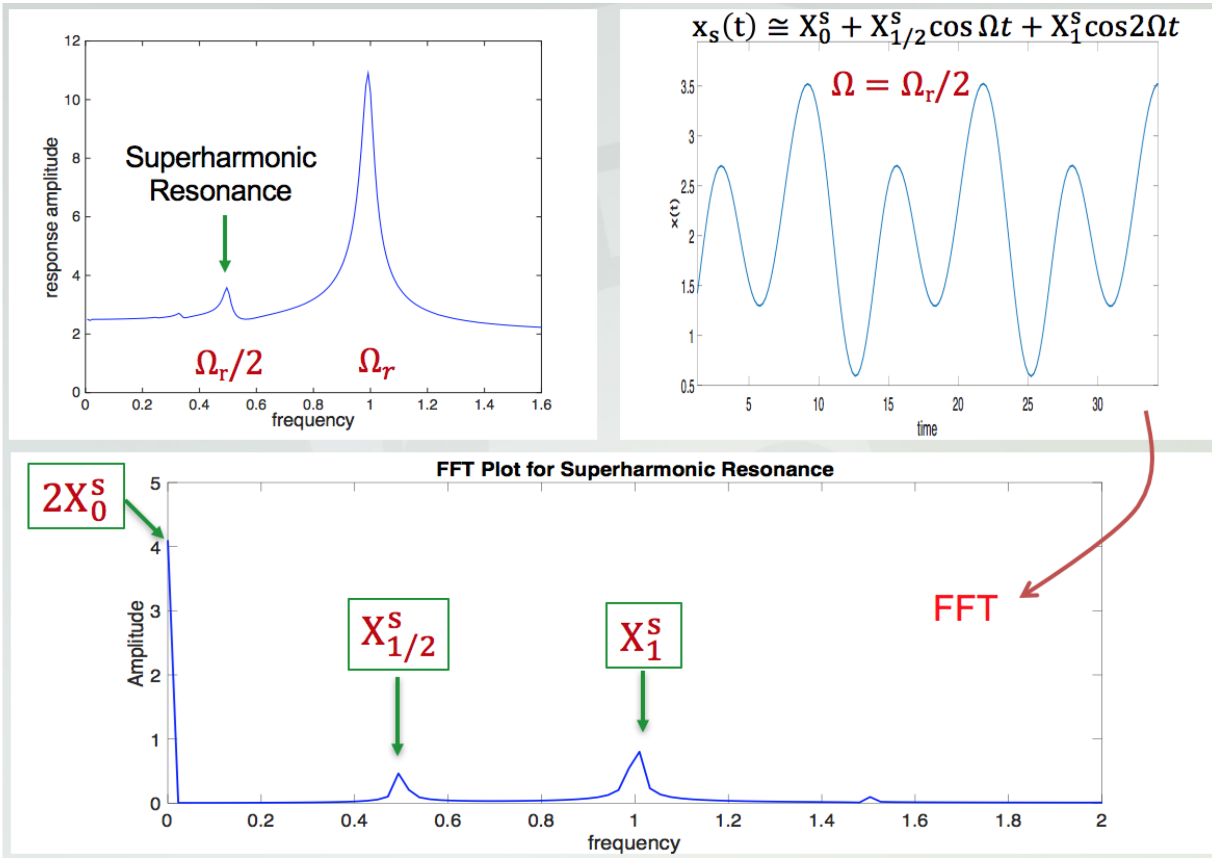

Figure 5.2: Example calculation with the superharmonic resonance

2. We excite superharmonic resonance at $\Omega \approx \omega_n/2$,

$$x = X_0^s + X_1^s \cos(\omega_n t + \beta) + X_{1/2}^s \cos(\tfrac{\omega_n}{2} t),$$

$$\text{where } X_0^s = \frac{F_0}{\omega_n^2}, \quad X_1^s = a_{max_s} = \frac{\epsilon F_0 \gamma^2}{3\mu\omega_n^5}, \quad X_{1/2}^s = \frac{4F_0\epsilon\gamma}{3\omega_n^4},$$

at the peak response, and we obtain values of X_0^s, X_1^s and $X_{1/2}^s$ with the help of a fast Fourier transform (FFT) as seen in Figure 5.2.

3. We excite primary resonance at $\Omega \approx \omega_n$,

$$x = X_0^p + X_1^p \cos(\omega_n t + \beta)$$

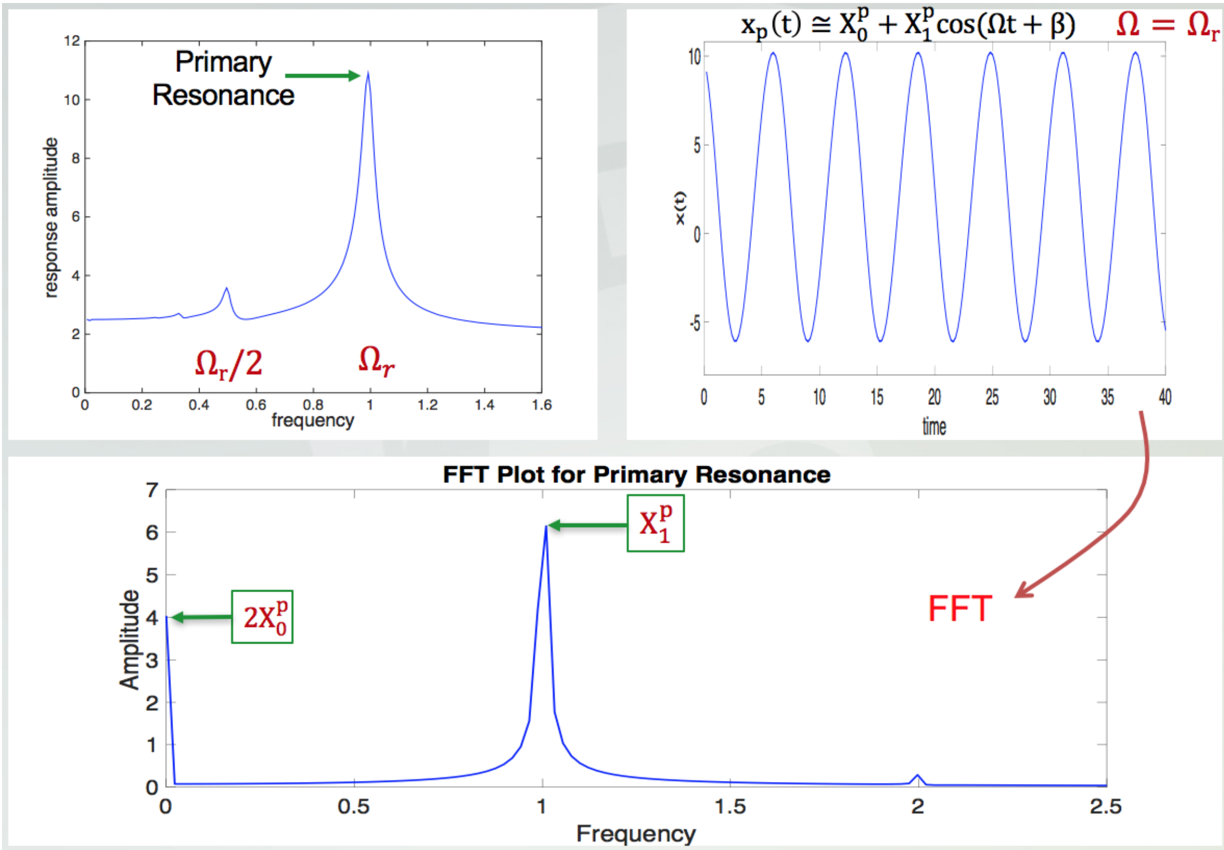

Figure 5.3: Example calculation with the primary resonance

where $X_0^p = \dfrac{F_0}{\omega_n^2}$, $\quad X_1^p = a_{maxp} = \dfrac{F_0\gamma}{2\mu\omega_n^3}$ at the peak. We find the values of X_0^p and X_1^p using the FFT plots as shown in Figure 5.3.

The values of X_0^s and X_0^p give us F_0. Figure 5.4 shows the estimated force compared to true values of F_0 with respect to different γ values. From $\dfrac{X_1^s}{X_1^p} = \dfrac{2\epsilon\gamma}{3\omega_n^2}$, we extract the value of $\epsilon\gamma$. Next, $\epsilon\gamma$ is inserted into the expression $X_1^s = \dfrac{F_0(\epsilon\gamma)^2}{3(\epsilon\mu)\omega_n^2}$ to obtain $\epsilon\mu$. Damping ratio is also found from $2\zeta\omega_n = 2\epsilon\mu$ as $\zeta = \dfrac{\epsilon\mu}{\omega_n}$.

5.1.4 Results and Discussion

We simulated responses with $\omega_n = 1$, $\mu = 0.5$, $\epsilon = 0.1$, and $F_0 = 2$, and various values of γ. We estimated parameters by comparing resonant amplitudes to their analytical expressions. Figure 5.5

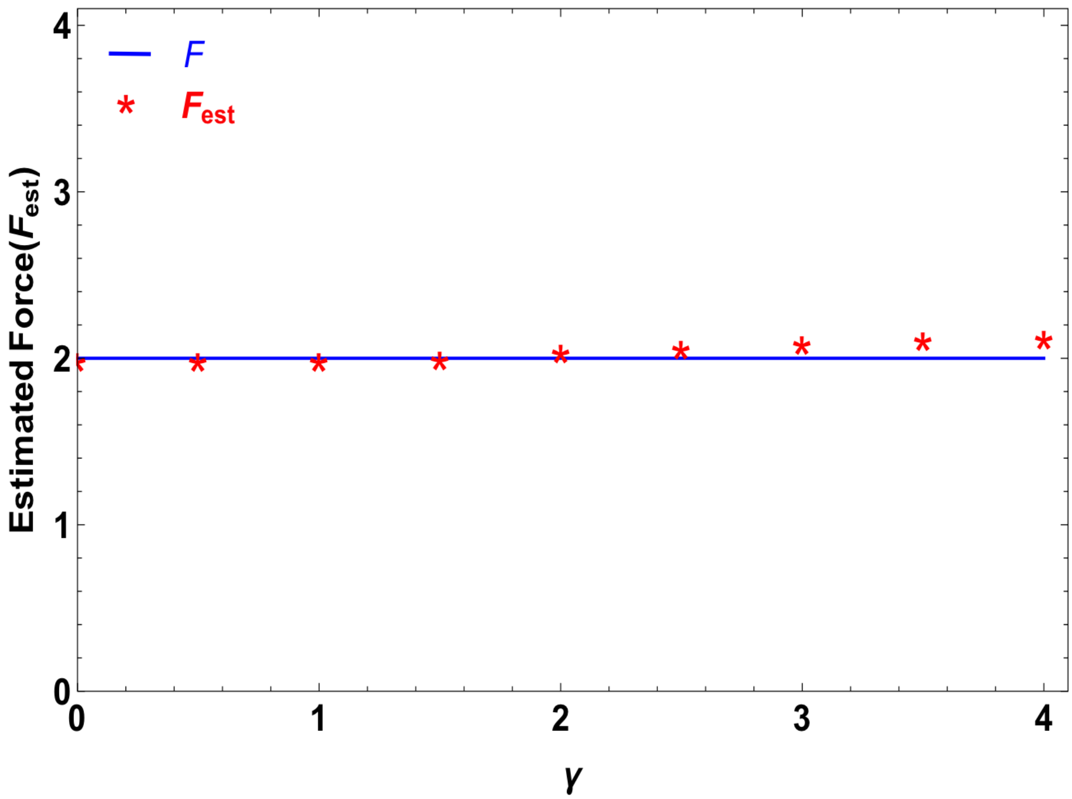

Figure 5.4: Estimated force F

demonstrates the estimation of γ and μ (8μ is plotted) for various true values of γ.

The perturbation solution degrades as $\epsilon\gamma$ increases, but we see good estimates of γ within a limited range. Damping μ is estimated within about 25%. Damping can be difficult to obtain accurately in vibration systems.

5.1.5 Proposed Work

We estimated parameters in a linear parametrically excited vibration system. Accuracy depends on the asymptotics of perturbation solutions which underlie the approach. Future work can involve sensitivity analysis, error analysis, and experiments. Also, this approach can be formulated for the case of

$$\ddot{q} + 2\epsilon\mu\dot{q} + (\omega^2 + \epsilon\gamma\cos\Omega t)q = F_1 \sin\Omega t$$

Then, we can combine(superpose) for case of $F_0 + F_1 \sin\Omega t$, as wind-turbine models.

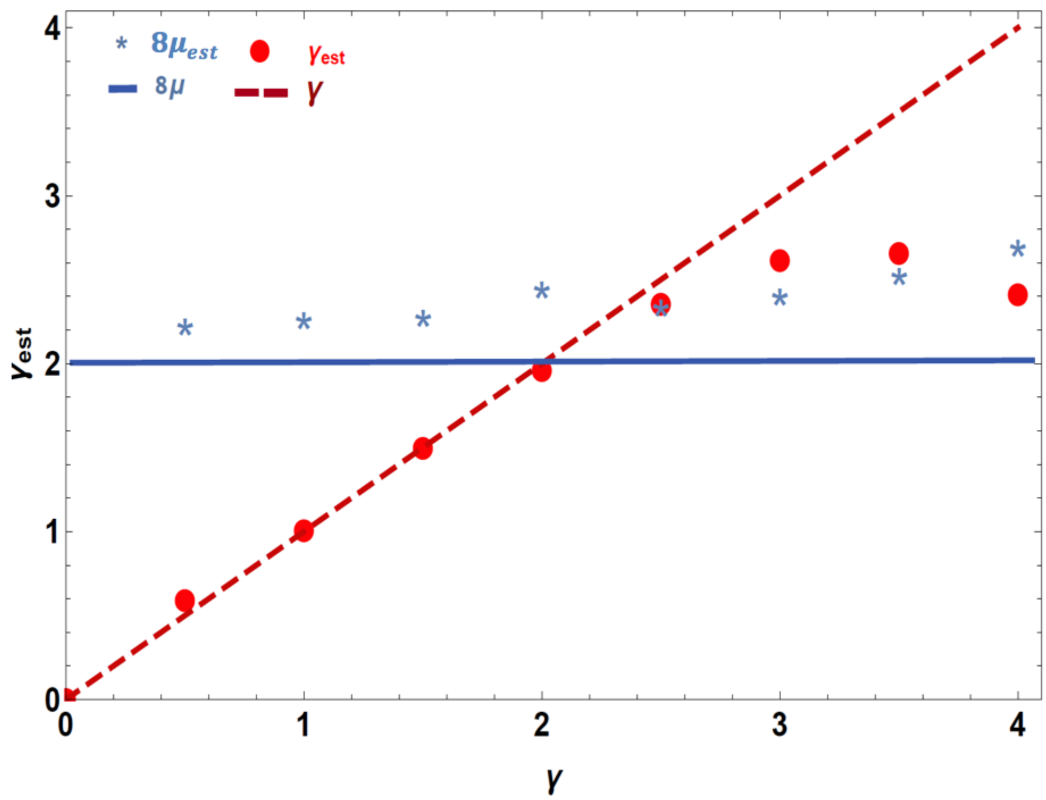

Figure 5.5: Estimated μ's and γ's. (The values of 8μ and $8\mu_{est}$ are plotted.)

5.2 Second-Order Perturbation Analysis of Forced Nonlinear Mathieu Equation

5.2.1 Introduction

Our interest in studying the in-plane dynamics of wind turbine blade directs us to this study. There has been various reseach on parametrically excited systems that suits specific minor variations of the Mathieu equation. Newman *et al.* [63] studied dynamics of a nonlinear parametrically excited partial differential equation. Bifurcations in a Mathieu equation with cubic nonlineraties were analyzed in [64] and stability analysis of a parametrically excited rotating system was done in [65]. Frequency locking in a forced Mathieu-van der Pol-Duffing system was studied by Pandey *et al.* [66] and bifurcation of subharmonic resonances in the Mathieu equation was analyzed in [67]. Higher-order perturbation analysis [68] and Floquet theory with harmonic balance solution [34] have been applied to study the stability wedges of the Mathieu equation. Since the Mathieu equation aligns well with higher-order multiple scales analysis to figure out stability characteristics out, we work with second-order method of multiple scales.

In this work, we look for superharmonic resonance at order three for the nonlinear Mathieu system with hard forcing by applying a second-order perturbation expansion. Sayed *et al.* [27] applied higher-order expansions to analyse stability and response of a nonlinear dynamical system. On the other hand, Romero *et al.* [69] employed different scaling techniques to analyze the quasiperiodic damped Mathieu equation.

5.2.2 A Nonlinear Mathieu Equation with Hard Excitation

In this analysis, we consider hard excitation, i.e. direct forcing F which is of order 1. The equation with nonlinearity is

$$\ddot{q} + 2\epsilon\mu\dot{q} + (\omega^2 + \epsilon\gamma\cos\Omega t)q + \epsilon\alpha q^3 = F\sin(\Omega t + \theta), \tag{5.2}$$

Applying the method of multiple scales, we work with three time scales (T_0, T_1, T_2) and q_0 as the dominant solution, with q_1 and q_2 are slow variations of that solution. Specifically,

$$q = q_0(T_0, T_1, T_2) + \epsilon q_1(T_0, T_1, T_2) + \epsilon^2 q_2(T_0, T_1, T_2) + \ldots \tag{5.3}$$

where $T_i = \epsilon^i T_0$. Then $\frac{d}{dt} = D_0 + \epsilon D_1 + \epsilon^2 D_2$ and where $D_i = \frac{\partial}{\partial T_i}$.

We insert these expressions into our ordinary differential Equation (5.2) and then simplify and the equations for $\epsilon^0, \epsilon^1, \epsilon^2$ coefficients are pulled out as

$$\begin{array}{llcl}
O(1): & D_0^2 q_0 + \omega^2 q_0 & = & F(\sin\Omega T_0 + \theta) \\
O(\epsilon): & D_0^2 q_1 + \omega^2 q_1 & = & -2\mu D_0 q_0 - 2D_0 D_1 q_0 - \gamma q_0\cos\Omega T_0 - \alpha q_0^3 \\
O(\epsilon^2): & D_0^2 q_2 + \omega^2 q_2 & = & -2D_0 D_1 q_1 - (D_1^2 + 2D_0 D_2)q_0 - 2\mu(D_0 q_1 + D_1 q_0) - \gamma q_1\cos\Omega T_0 \\
 & & & -3\alpha q_0^2 q_1
\end{array} \tag{5.4}$$

By solving the $O(1)$ equation, we obtain the q_0 solution as

$$q_0 = Ae^{i\omega T_0} - i\Lambda e^{i\Omega T_0} + c.c. \tag{5.5}$$

where $\Lambda = \dfrac{F}{2(\omega^2 - \Omega^2)}$, and $A = Be^{i\sigma\epsilon t}$, with $B = X + iY$

The coefficient A, and hence X and Y are functions of T_1 and T_2. Plugging Equation (5.5) into the $O(\epsilon)$ expression, we get

$$\begin{aligned} D_0^2 q_1 + \omega^2 q_1 \quad = \quad & -2\mu(Ai\omega e^{i\omega T_0} + \Lambda\Omega e^{i\Omega T_0}) - 2D_1 Ai\omega e^{i\omega T_0} \\ & -\tfrac{\gamma}{2}\left(Ae^{i(\omega+\Omega)T_0} + \bar{A}e^{i(\Omega-\omega)T_0} - i\Lambda e^{2i\Omega T_0} - i\Lambda\right) \\ & -\alpha\big[A^3 e^{3i\omega T_0} + i\Lambda^3 e^{3i\Omega T_0} - 3A^2 i\Lambda e^{i(2\omega+\Omega)T_0} \\ & -3\Lambda^2 Ae^{i(\omega+2\Omega)T_0} + 3iA^2\bar{\Lambda}e^{i(2\omega-\Omega)T_0} \\ & +3A^2\bar{A}e^{i\omega T_0} - 3i\Lambda^2\bar{\Lambda}e^{i\Omega T_0} - 3i\Lambda^2\bar{A}e^{i(2\Omega-\omega)T_0} \\ & +6A\Lambda\bar{\Lambda}e^{i\omega T_0} - 6iA\bar{A}\Lambda e^{i\Omega T_0}\big] + c.c \end{aligned} \tag{5.6}$$

For Equation (5.6), there are five possible cases that lead up to resonance conditions.

1. No specific relationship between Ω and ω at $O(\epsilon)$
2. $\Omega \approx \omega$
3. $\Omega \approx 2\omega$
4. $\Omega \approx \omega/2$
5. $\Omega \approx \omega/3$

5.2.3 Case 1: No Resonance at $O(\epsilon)$

Between the natural frequency ω and the forcing frequency Ω, there is no specific relationship. We extract secular terms from Equation (5.6) and equate them to zero, such that

$$-2i\omega D_1 A - 2\mu i\omega A - 3\alpha A^2\bar{A} + 6A\alpha\Lambda\bar{\Lambda} = 0.$$

Then, solving the rest of the ODE in Equation (5.6), we obtain the particular solution for q_1 as

$$\begin{aligned}
q_1 = & \frac{2\mu\Lambda\Omega e^{i\Omega T_0}}{\Omega^2-\omega^2} + \frac{\gamma A}{2\left[(\omega+\Omega)^2-\omega^2\right]}e^{i(\omega+\Omega)T_0} + \frac{\gamma\bar{A}}{2\left[(\Omega-\omega)^2-\omega^2\right]}e^{i(\Omega-\omega)T_0} + \frac{\gamma i\Lambda}{2(\omega^2-4\Omega^2)}e^{2i\Omega T_0} \\
& + \frac{\alpha A^3}{8\omega^2}e^{3i\omega T_0} + \frac{i\alpha\Lambda^3}{9\Omega^2-\omega^2}e^{3i\Omega T_0} + \frac{3iA^2\alpha\Lambda}{\left[\omega^2-(2\omega+\Omega)^2\right]}e^{i(2\omega+\Omega)T_0} + \frac{3\alpha\Lambda^2 A}{\left[\omega^2-(\omega+2\Omega)^2\right]}e^{i(\omega+2\Omega)T_0} \\
& + \frac{3i\alpha A^2\bar{\Lambda}}{\left[(2\omega-\Omega)^2-\omega^2\right]}e^{i(2\omega-\Omega)T_0} + \frac{3i\alpha\Lambda^2\bar{\Lambda}}{\omega^2-\Omega^2}e^{i\Omega T_0} + \frac{3i\alpha\Lambda^2\bar{A}}{\left[\omega^2-(2\Omega-\omega)^2\right]}e^{i(2\Omega-\omega)T_0} + \frac{6i\alpha A\bar{A}\Lambda}{\omega^2-\Omega^2}e^{i\Omega T_0} \\
& + \frac{\gamma i\Lambda}{2\omega^2} + c.c
\end{aligned} \tag{5.7}$$

5.2.4 Case 2: Primary Resonance at $O(\epsilon)$

When $\Omega \approx \omega$, i.e. letting $\Omega = \omega + \epsilon\sigma$ (σ is detuning parameter) in Equation (5.6), the solvability condition is

$$-2i\omega D_1 A - 2\mu i\omega A - 3\alpha A^2\bar{A} + 6A\alpha\Lambda\bar{\Lambda} - e^{i\sigma T_1}\left[2\mu\Lambda\Omega + 3\alpha i A^2\bar{\Lambda} + 3\alpha i\Lambda^2\bar{\Lambda} + 3i\alpha\Lambda^2\bar{A} + 6\alpha i A\bar{A}\Lambda\right] = 0$$

Then, the particular solution for q_1 turns out to be

$$\begin{aligned}
q_1 = & \frac{\gamma A}{2\left[(\omega+\Omega)^2-\omega^2\right]}e^{i(\omega+\Omega)T_0} + \frac{\gamma\bar{A}}{2\left[(\Omega-\omega)^2-\omega^2\right]}e^{i(\Omega-\omega)T_0} + \frac{\gamma i\Lambda}{2(\omega^2-4\Omega^2)}e^{2i\Omega T_0} + \frac{\alpha A^3}{8\omega^2}e^{3i\omega T_0} \\
& + \frac{i\alpha\Lambda^3}{9\Omega^2-\omega^2}e^{3i\Omega T_0} + \frac{3iA^2\alpha\Lambda}{\left[\omega^2-(2\omega+\Omega)^2\right]}e^{i(2\omega+\Omega)T_0} + \frac{3\alpha\Lambda^2 A}{\left[\omega^2-(\omega+2\Omega)^2\right]}e^{i(\omega+2\Omega)T_0} + \frac{\gamma i\Lambda}{2\omega^2} + c.c
\end{aligned} \tag{5.8}$$

5.2.5 Case 3: Subharmonic Resonance of Order $1/2$ at $O(\epsilon)$

When $\Omega \approx 2\omega$, i.e. $\Omega = 2\omega + \epsilon\sigma$, the solvability condition for Equation (5.6) is

$$-2i\omega D_1 A - 2\mu i\omega A - 3\alpha A^2\bar{A} + 6A\alpha\Lambda\bar{\Lambda} - \frac{\gamma\bar{A}}{2}e^{i\sigma T_1} = 0$$

The particular solution of Equation (5.6) for q_1 is obtained as

$$q_1 = \frac{2\mu\Lambda\Omega e^{i\Omega T_0}}{\Omega^2 - \omega^2} + \frac{\gamma A}{2\left[(\omega+\Omega)^2 - \omega^2\right]}e^{i(\omega+\Omega)T_0} + \frac{\gamma i\Lambda}{2(\omega^2 - 4\Omega^2)}e^{2i\Omega T_0} + \frac{\alpha A^3}{8\omega^2}e^{3i\omega T_0} + \frac{\gamma i\Lambda}{2\omega^2}$$

$$+ \frac{i\alpha\Lambda^3}{9\Omega^2 - \omega^2}e^{3i\Omega T_0} + \frac{3iA^2\alpha\Lambda}{\left[\omega^2 - (2\omega+\Omega)^2\right]}e^{i(2\omega+\Omega)T_0} + \frac{3\alpha\Lambda^2 A}{\left[\omega^2 - (\omega+2\Omega)^2\right]}e^{i(\omega+2\Omega)T_0} + \frac{3i\alpha\Lambda^2\bar{\Lambda}}{\omega^2 - \Omega^2}e^{i\Omega T_0}$$

$$+ \frac{3i\alpha A^2\bar{\Lambda}}{\left[(2\omega-\Omega)^2 - \omega^2\right]}e^{i(2\omega-\Omega)T_0} + \frac{3i\alpha\Lambda^2\bar{A}}{\left[\omega^2 - (2\Omega-\omega)^2\right]}e^{i(2\Omega-\omega)T_0} + \frac{6i\alpha A\bar{A}\Lambda}{\omega^2 - \Omega^2}e^{i\Omega T_0} + c.c \quad (5.9)$$

5.2.6 Case 4: Superharmonic Resonance of Order 2 at $O(\epsilon)$

When $\Omega \approx \omega/2$, i.e. $2\Omega = \omega + \epsilon\sigma$, the solvability condition for Equation (5.6) is

$$-2i\omega D_1 A - 2\mu i\omega A - 3\alpha A^2\bar{A} + 6A\alpha\Lambda\bar{\Lambda} + \frac{\gamma i\Lambda}{2}e^{i\sigma T_1} = 0$$

The particular solution of Equation equation (5.6) for q_1 is found as

$$q_1 = \frac{2\mu\Lambda\Omega e^{i\Omega T_0}}{\Omega^2 - \omega^2} + \frac{\gamma A}{2\left[(\omega+\Omega)^2 - \omega^2\right]}e^{i(\omega+\Omega)T_0} + \frac{\gamma\bar{A}}{2\left[(\Omega-\omega)^2 - \omega^2\right]}e^{i(\Omega-\omega)T_0} + \frac{\alpha A^3}{8\omega^2}e^{3i\omega T_0}$$

$$+ \frac{3i\alpha\Lambda^2\bar{\Lambda}}{\omega^2 - \Omega^2}e^{i\Omega T_0} + \frac{i\alpha\Lambda^3}{9\Omega^2 - \omega^2}e^{3i\Omega T_0} + \frac{3iA^2\alpha\Lambda}{\left[\omega^2 - (2\omega+\Omega)^2\right]}e^{i(2\omega+\Omega)T_0} + \frac{3\alpha\Lambda^2 A}{\left[\omega^2 - (\omega+2\Omega)^2\right]}e^{i(\omega+2\Omega)T_0}$$

$$+ \frac{3i\alpha A^2\bar{\Lambda}}{\left[(2\omega-\Omega)^2 - \omega^2\right]}e^{i(2\omega-\Omega)T_0} + \frac{3i\alpha\Lambda^2\bar{A}}{\left[\omega^2 - (2\Omega-\omega)^2\right]}e^{i(2\Omega-\omega)T_0} + \frac{6i\alpha A\bar{A}\Lambda}{\omega^2 - \Omega^2}e^{i\Omega T_0} + \frac{\gamma i\Lambda}{2\omega^2} + c.c$$

$$(5.10)$$

5.2.7 Case 5: Superharmonic Resonance of Order 3 at $O(\epsilon)$

When $\Omega \approx \omega/3$, i.e. $3\Omega = \omega + \epsilon\sigma$, the solvability condition for Equation (5.6) is

$$-2i\omega D_1 A - 2\mu i\omega A - 3\alpha A^2\bar{A} + 6A\alpha\Lambda\bar{\Lambda} - \alpha i\Lambda^3 e^{i\sigma T_1} = 0 \tag{5.11}$$

The particular solution for q_1 then becomes

$$q_1 = \frac{2\mu\Lambda\Omega e^{i\Omega T_0}}{\Omega^2 - \omega^2} + \frac{\gamma A}{2\left[(\omega+\Omega)^2 - \omega^2\right]} e^{i(\omega+\Omega)T_0} + \frac{\gamma\bar{A}}{2\left[(\Omega-\omega)^2 - \omega^2\right]} e^{i(\Omega-\omega)T_0} + \frac{\alpha A^3}{8\omega^2} e^{3i\omega T_0}$$

$$+ \frac{\gamma i\Lambda}{2(\omega^2 - 4\Omega^2)} e^{2i\Omega T_0} + \frac{3iA^2\alpha\Lambda}{\left[\omega^2 - (2\omega+\Omega)^2\right]} e^{i(2\omega+\Omega)T_0} + \frac{3\alpha\Lambda^2 A}{\left[\omega^2 - (\omega+2\Omega)^2\right]} e^{i(\omega+2\Omega)T_0} + \frac{\gamma i\Lambda}{2}$$

$$+ \frac{3i\alpha A^2\bar{\Lambda}}{\left[(2\omega-\Omega)^2 - \omega^2\right]} e^{i(2\omega-\Omega)T_0} + \frac{3i\alpha\Lambda^2\bar{\Lambda}}{\omega^2 - \Omega^2} e^{i\Omega T_0} + \frac{3i\alpha\Lambda^2\bar{A}}{\left[\omega^2 - (2\Omega-\omega)^2\right]} e^{i(2\Omega-\omega)T_0} + \frac{6i\alpha A\bar{A}\Lambda}{\omega^2 - \Omega^2} e^{i\Omega T_0}$$

$$+ c.c \tag{5.12}$$

To follow the next steps smoothly, the expression of Equation (5.12) is simplified as follows:

$$q_1 = \frac{N}{\omega^2 - \Omega^2} e^{i\Omega T_0} + \frac{M}{\omega^2 - 4\Omega^2} e^{2i\Omega T_0} + \frac{P}{\omega^2 - (\Omega+\omega)^2} e^{i(\Omega+\omega)T_0} + \frac{Q}{\omega^2} + \frac{R}{\omega^2 - (\Omega-\omega)^2} e^{i(\Omega-\omega)T_0}$$

$$+ \frac{S}{\omega^2 - 9\omega^2} e^{3i\omega T_0} + \frac{T}{\omega^2 - (\Omega+2\omega)^2} e^{i(\Omega+2\omega)T_0} + \frac{U}{\omega^2 - (2\Omega+\omega)^2} e^{i(2\Omega+\omega)T_0}$$

$$+ \frac{V}{\omega^2 - (\Omega-2\omega)^2} e^{i(\Omega-2\omega)T_0} + \frac{W}{\omega^2 - (2\Omega-\omega)^2} e^{i(2\Omega-\omega)T_0} + c.c \tag{5.13}$$

where $N = -2\mu\Omega\Lambda + 3\alpha i\Lambda^2\bar{\Lambda} + 6i\alpha A\bar{A}\Lambda$, $\quad M = \frac{\gamma i\Lambda}{2}$, $\quad P = -\frac{\gamma A}{2}$, $\quad Q = \frac{\gamma i\Lambda}{2}$, $\quad R = -\frac{\gamma\bar{A}}{2}$,

$S = -\alpha A^3$, $\quad T = 3\alpha A^2\Lambda i$, $\quad U = 3\alpha\Lambda^2 A$, $\quad V = 3i\alpha\bar{A}^2\Lambda$, $\quad W = 3\alpha\Lambda^2\bar{A}$

We are specifically focusing on superharmonic resonance case of $O(\epsilon^2)$ at order 3 to determine terms that can effect the resonance condition.

Substituting solutions for q_0 from Equation (5.5) and q_1 from Equation (5.13) into Equation (5.4) at $O(\epsilon^2)$, for superharmonic case when $\Omega \approx \omega/3$, i.e. $3\Omega = \omega + \epsilon\sigma$, the equation at $O(\epsilon^2)$ becomes

$$D_0^2 q_2 + \omega^2 q_2 = \Bigg[-2\omega i D_2 A - D_1^2 A - 2\mu D_1 A - \frac{\gamma P}{2\big(\omega^2 - (\Omega+\omega)^2\big)} - \frac{\gamma \bar{R}}{2\big(\omega^2 - (\Omega-\omega)^2\big)} + \frac{3\alpha A i \Lambda \bar{N}}{\omega^2 - \Omega^2}$$

$$- \frac{3\alpha A i \bar{\Lambda} N}{\omega^2 - \Omega^2} + \frac{3\alpha i \bar{A} \bar{V} \Lambda}{\omega^2 - (\Omega - 2\omega)^2} - \frac{3\alpha \bar{A}^2 S}{\omega^2 - 9\Omega^2} - \frac{3\alpha i \bar{\Lambda} \bar{A} T}{\omega^2 - (2\omega + \Omega)^2} + \frac{3\alpha \bar{\Lambda}^2 U}{\omega^2 - (2\Omega + \omega)^2} + \frac{3\alpha \Lambda^2 \bar{W}}{\omega^2 - (2\Omega - \omega)^2}\Bigg] e^{i\omega T_0}$$

$$\Bigg[- \frac{\gamma M}{2\big(\omega^2 - 4\Omega^2\big)} + \frac{3\alpha \Lambda^2 N}{\omega^2 - \Omega^2} + \frac{3\alpha U i \Lambda \bar{A}}{\omega^2 - (2\Omega + \omega)^2} + \frac{A i \Lambda W}{\omega^2 - (2\Omega - \omega)^2}\Bigg] e^{3i\Omega T_0} + N.S.T. \quad (5.14)$$

where $N.S.T.$ refers non secular terms.

Equating the expressed secular terms to zero, letting $3\Omega \approx \omega + \epsilon\sigma$, provides the solvability condition at $O(\epsilon^2)$. This colvability condition and the solvability condition from $O(\epsilon)$ in Equation (5.11) are now listed together, following the analysis done in [68]:

$$\begin{aligned} O(\epsilon): &\quad -2i\omega D_1 A - 2\mu i \omega A - 3\alpha A^2 \bar{A} + 6A\alpha\Lambda\bar{\Lambda} - \alpha i \Lambda^3 e^{i\sigma T_1} = 0 \\ O(\epsilon^2): &\quad -2i\omega D_2 A - D_1^2 A - 2\mu D_1 A + (K_1 + K_2 A + K_3 \bar{A}) e^{i\sigma T_1} + K_4 + K_5 A + K_6 \bar{A} + K_7 \bar{A}^2 = 0 \end{aligned} \quad (5.15)$$

where $K_1 = \dfrac{\gamma M}{2(\omega^2 - 4\Omega^2)} + \dfrac{3\Lambda^2 \alpha N}{\omega^2 - \Omega^2}, \quad K_2 = \dfrac{3i\Lambda\alpha W}{\omega^2 - (2\Omega - \omega)^2}, \quad K_3 = \dfrac{3i\alpha\Lambda U}{\omega^2 - (2\Omega + \omega)^2},$

$$K_4 = -\frac{\gamma}{2}\Big(\frac{P}{\omega^2 - (\Omega + \omega)^2} + \frac{\bar{R}}{\omega^2 - (\Omega - \omega)^2}\Big) + \frac{3\alpha\bar{\Lambda}^2 U}{\omega^2 - (2\Omega + \omega)^2} + \frac{3\alpha\Lambda^2 \bar{W}}{\omega^2 - (2\Omega - \omega)^2},$$

$$K_5 = \frac{3\alpha i \Lambda \bar{N}}{\omega^2 - \Omega^2} - \frac{3\alpha i \bar{\Lambda} N}{\omega^2 - \Omega^2}, \quad K_6 = \frac{3\alpha i \Lambda \bar{V}}{\omega^2 - (\Omega - 2\omega)^2} - \frac{3\alpha i \bar{\Lambda} T}{\omega^2 - (\Omega + 2\omega)^2}, \quad K_7 = -\frac{3\alpha S}{\omega^2 - 9\omega^2}$$

We unfold the superharmonic resonance at order 3 by using hard forcing in this analysis, however it was not captured with weak forcing in [21]. In a process called reconstitution, we put the terms at $O(\epsilon)$ and $O(\epsilon^2)$ together into a single ordinary differential equation and look for solutions.

From expression of $O(\epsilon)$ in Equation (5.15), we extract $D_1 A$, then obtain $D_1 \bar{A}$ as

$$D_1 A = -\mu A + \frac{3\alpha i A^2 \bar{A}}{2\omega} + \frac{6\alpha i A\Lambda\bar{\Lambda}}{2\omega} - \frac{\alpha\Lambda^3 e^{i\sigma T_1}}{2\omega}$$

and

$$D_1 \bar{A} = -\mu\bar{A} - \frac{3\alpha i \bar{A}^2 A}{2\omega} - \frac{6\alpha i \bar{A}\bar{\Lambda}\Lambda}{2\omega} - \frac{\alpha\bar{\Lambda}^3 e^{-i\sigma T_1}}{2\omega}.$$

We compute the expression of $D_1^2 A$ using $D_1 A$ and $D_1 \bar{A}$ as

$$D_1^2 A = \mu^2 A - \frac{6i\alpha\mu A^2\bar{A}}{\omega} - \frac{6i\alpha\mu A\Lambda\bar{\Lambda}}{\omega} + \frac{\alpha\mu\Lambda^3 e^{i\sigma T_1}}{2\omega} - \frac{9\alpha^2 A^3\bar{A}^2}{4\omega^2} - \frac{36\alpha^2 A^2\bar{A}\Lambda\bar{\Lambda}}{4\omega^2} + \frac{36\alpha^2 A\Lambda^2\bar{\Lambda}^2}{4\omega^2}$$

$$-\frac{3i\alpha^2 A^2\bar{\Lambda}^3 e^{-i\sigma T_1}}{4\omega^2} - \frac{3i\alpha^2\Lambda^3 A\bar{A}e^{i\sigma T_1}}{4\omega^2} - \frac{6i\alpha^2\bar{\Lambda}\Lambda^4 e^{i\sigma T_1}}{4\omega^2} - \frac{i\alpha\sigma\Lambda^3 e^{i\sigma T_1}}{2\omega}$$

Then, we insert the $D_1 A$ and $D_1^2 A$ into the $O(\epsilon^2)$ expression in the Equation (5.15) to obtain $D_2 A$.

$$\begin{aligned}-2i\omega D_2 A &= \mu^2 A - \frac{6i\alpha\mu A^2\bar{A}}{\omega} - \frac{6i\alpha\mu A\Lambda\bar{\Lambda}}{\omega} + \frac{\alpha\mu\Lambda^3 e^{i\sigma T_1}}{2\omega} - \frac{9\alpha^2 A^3\bar{A}^2}{4\omega^2} - \frac{36\alpha^2 A^2\bar{A}\Lambda\bar{\Lambda}}{4\omega^2} + \frac{36\alpha^2 A\Lambda^2\bar{\Lambda}^2}{4\omega^2} \\ &-\frac{3i\alpha^2 A^2\bar{\Lambda}^3 e^{-i\sigma T_1}}{4\omega^2} - \frac{3i\alpha^2\Lambda^3 A\bar{A}e^{i\sigma T_1}}{4\omega^2} - \frac{6i\alpha^2\bar{\Lambda}\Lambda^4 e^{i\sigma T_1}}{4\omega^2} - \frac{i\alpha\sigma\Lambda^3 e^{i\sigma T_1}}{2\omega} + 2\mu\Big(- \mu A + \frac{3\alpha i A^2\bar{A}}{2\omega} \\ &+\frac{6\alpha i A\Lambda\bar{\Lambda}}{2\omega} - \frac{\alpha\Lambda^3 e^{i\sigma T_1}}{2\omega}\Big) - (K_1 + K_2 A + K_3\bar{A})e^{i\sigma T_1} - K_4 - K_5 A - K_6\bar{A} - K_7\bar{A}^2\end{aligned} \tag{5.16}$$

Noting that $\frac{dA}{dt} = (D_0 + \epsilon D_1 + \epsilon D_2)A = \epsilon D_1 A + \epsilon^2 D_2 A$ the solvability condition equations $D_1 A$ and $D_2 A$ are worked together out to get a single ODE for A. (As we mentioned in Chapter 3.3.2, recombining the time scales (T_0, T_1, T_3) is a process called "reconstitution" [26] and [29]). The resulting reconstituted equation is

$$-2i\omega\frac{dA}{dt}+2\omega i\epsilon D_1A+2\omega i\epsilon^2D_2A=0 \tag{5.17}$$

Subsequently, D_1A and D_2A expressions are placed into the equation (5.17) to get the reconstituted differential equation as

$$\begin{aligned}
&-2\omega i\tfrac{dA}{dt}+\epsilon\Big(-2i\omega\mu A-3\alpha A^2\bar{A}-6\alpha A\Lambda\bar{\Lambda}-i\alpha\Lambda^3e^{i\sigma T_1}\Big)-\epsilon^2\Big(\mu^2A-\tfrac{6i\alpha\mu A^2\bar{A}}{\omega}-\tfrac{6i\alpha\mu A\Lambda\bar{\Lambda}}{\omega}\\
&+\tfrac{\alpha\mu\Lambda^3e^{i\sigma T_1}}{2\omega}-\tfrac{9\alpha^2A^3\bar{A}^2}{4\omega^2}-\tfrac{36\alpha^2A^2\bar{A}\Lambda\bar{\Lambda}}{4\omega^2}+\tfrac{36\alpha^2A\Lambda^2\bar{\Lambda}^2}{4\omega^2}-\tfrac{3i\alpha^2A^2\bar{\Lambda}^3e^{-i\sigma T_1}}{4\omega^2}-\tfrac{3i\alpha^2\Lambda^3A\bar{A}e^{i\sigma T_1}}{4\omega^2}\\
&-\tfrac{6i\alpha^2\bar{\Lambda}\Lambda^4e^{i\sigma T_1}}{4\omega^2}-\tfrac{i\alpha\sigma\Lambda^3e^{i\sigma T_1}}{2\omega}+2\mu\big(-\mu A+\tfrac{3\alpha iA^2\bar{A}}{2\omega}+\tfrac{6\alpha iA\Lambda\bar{\Lambda}}{2\omega}-\tfrac{\alpha\Lambda^3e^{i\sigma T_1}}{2\omega}\big)\\
&-(K_1+K_2A+K_3\bar{A})e^{i\sigma T_1}-K_4-K_5A-K_6\bar{A}-K_7\bar{A}^2\Big)=0
\end{aligned} \tag{5.18}$$

Following the procedure in [68], we seek a solution in the Cartesian coordinate form $A=(X+iY)e^{i\sigma\epsilon t}$, with real X and Y. Expressions A and Λ are inserted into the equation (5.18), then the equation is divided by common exponential term $e^{i\sigma\epsilon t}$ and real and imaginary parts are separated.

Imaginary part:

$$\begin{aligned}
&-2\omega\dot{X}+Z_0\sin 3\theta-Z_1\cos 3\theta-Z_2X^2\cos 3\theta-Z_3Y^2\cos 3\theta+Z_4X^2\cos 3\theta+Z_5Y^2\cos 3\theta\\
&+Z_6XY\sin 3\theta+Z_7X+Z_9Y+Z_{11}XY^2+Z_{14}X^2Y+Z_{15}X^2Y^3+Z_{17}X^4Y+Z_{19}Y^3+Z_{21}Y^5\\
&+Z_{22}\cos\theta+Z_{23}X^3=0
\end{aligned} \tag{5.19}$$

Real Part:

$$2\omega\dot{Y} + Z_0\cos 3\theta - Z_1\sin 3\theta - Z_2X^2\sin 3\theta - Z_3Y^2\sin 3\theta + Z_4X^2\sin 3\theta + Z_5Y^2\sin 3\theta$$

$$+Z_6XY\cos 3\theta + Z_8X + Z_{10}Y + Z_{12}XY^2 + Z_{13}XY^4 + Z_{16}X^3Y^2 + Z_{18}X^3 + Z_{20}X^5 + Z_{22}\sin\theta$$

$$+Z_{24}X^2Y + Z_{25}Y^3 = 0 \tag{5.20}$$

where Z_0, Z_1, Z_2, Z_3, Z_4, Z_5, Z_6, Z_7, Z_8, Z_9, Z_{10}, Z_{11}, Z_{12}, Z_{13}, Z_{14}, Z_{15}, Z_{16}, Z_{17}, Z_{18}, Z_{19}, Z_{20}, Z_{21}, Z_{22}, Z_{23}, Z_{24}, Z_{25} can be found in Appendix D.

Equations (5.19) and (5.20) are demonstrated in matrix form as

$$2\omega\begin{bmatrix}\dot{X}\\ \dot{Y}\end{bmatrix} = \begin{bmatrix}Z_7 & Z_8\\ -Z_8 & Z_7\end{bmatrix}\begin{bmatrix}X\\ Y\end{bmatrix} + (X^2+Y^2)\begin{bmatrix}Z_{11} & Z_{12}\\ -Z_{12} & Z_{11}\end{bmatrix}\begin{bmatrix}X\\ Y\end{bmatrix} + (X^2+Y^2)^2\begin{bmatrix}0 & Z_{13}\\ Z_{13} & 0\end{bmatrix}\begin{bmatrix}X\\ Y\end{bmatrix}$$

$$+\begin{bmatrix}(Z_2+Z_4)X^2\cos(3\theta) - Z_4(2XY)\sin(3\theta) + (Z_2-Z_4)Y^2\cos(3\theta)\\ (Z_2-Z_4)X^2\sin(3\theta) + Z_4(2XY)\cos(3\theta) + (Z_2+Z_4)Y^2\sin(3\theta)\end{bmatrix} + \begin{bmatrix}Z_0\sin(3\theta) + (Z_1+Z_{22})\cos(3\theta)\\ -Z_0\cos(3\theta) + (Z_1+Z_{22})\sin(3\theta)\end{bmatrix} \tag{5.21}$$

In the next stages of this work, we will seek steady-state solutions of X and Y in Equation (5.21), analyze the stability, and then make interpretations.

5.2.8 Conclusion

The hard-forced, nonlinear Mathieu equation was analyzed. Second-order perturbation expansion was applied to determine stability characteristic based on system parameters, γ, μ, ϵ, F, σ and ω. It reveals a primary resonance, superhamonics at orders 2 and 3 and also a subharmonic at order $1/2$.

Since we have a challenge to solve the nonlinear ordinary differential equations (5.21) due to the fifth degree term in the $\dot{X}$ and $\dot{Y}$ expressions, this analysis is not yet completed, and we will focus on steady-state solutions and stabilities in the future.

5.2.9 Proposed Work

We would like to solve the nonlinear ordinary differential equations (5.21) analytically and numerically, and then we will perform numerical simulations to validate the analytical results on the resonances.

CHAPTER 6

CONCLUSION AND FUTURE WORK

6.1 Conclusion

The purpose of this thesis was to analyze the characteristics of the dynamics of horizontal axis wind turbines. Cylic loads on wind turbine blades and their effects on the blade vibration were considered. An analysis of in-plane coupled blade-hub dynamics of three-blade wind turbines with tuned and mistuned blades was studied. Four-degree-of-freedom systems with parametric stiffness were examined because this system matched the motivation of three-blade wind turbine and rotor system.

In Chapter 2, by using a simplified model, in-plane vibrations were taken into consideration for a detuned three-blade wind turbine. Coupled blades and rotor equation of motions in time domain were transformed into the ϕ (rotor-angle) domain to decouple the blade equations from the rotor equation. Since we assumed variations in the rotor speed were small and applied a nondimensionalization and parameter scaling, blade equations were decoupled from rotor equation. The first-order method of multiple scales was employed to analyse the uncoupled blade equations. After decoupling steps, the blade equations included parametric and direct excitation. Superharmonic and subharmonic resonances were caused by these excitations. We examined resonances due to cyclic gravitational and aerodynamic loading. Superharmonic resonance was observed near $2\omega_1 = 1 + \epsilon\sigma$ where ω_1 is a scaled excitation order. For the small positive mistuning, the blade amplitudes go through variations. When the mistuning was larger, the mistuned blade amplitudes diminished. Very small mistuning was the worst, meaning one blade experienced larger vibration amplitude than in the symmetric case. We have observed that superharmonic resonances that were seen in the symmetric case could be split into multiple resonance peaks, and that the blades could then take on different steady state amplitudes. Likewise, the same was true for primary resonance. The effects of parameters on the superharmonic resonances are studied, and a numerical study is carried out aimed at verifying the analytical results. Moreover, the rotor dynamics during resonance was investigated. Addition to illustrating the effects of damping and forcing level, the first-order perturbation solutions are verified with comparisons to numerical simulations at superharmonic resonance of order two. The simulation point to speed-locking phenomenon, in which the superharmonic speed is locked in for an interval of applied mean loads. Later, the effect of rotor loading on the rotor speed and blade amplitudes is investigated for different initial conditions and mistuning cases. Lastly, we aim to analytically confirm the blade response amplitudes at various rotor speeds near resonance and verify speed locking phenomenon by applying method of harmonic balance. From another point of view, subharmonic resonance would not occur in a rotating system with similar parameter scaling. Subharmonic resonances may or may not be possible in this dynamical system, depending on parameters, and at rotor speeds well outside the expected operating conditions of wind turbines. Subharmonic resonances involve instabilities similar to those of the Mathieu equation, but more complicated. we aimed to analytically confirm the blade response amplitudes at various rotor speeds near resonance and verify speed locking phenomenon.

Furthermore, we extended the previous study to higher-order perturbation expansion analysis on the coupled blade-rotor dynamics of horizontal-axis wind turbines with and without mistuning. Second-order method of multiple scales analysis revealed the superharmonic resonance case at order three. However, this resonance could not be observed in the linearized system with a first-order expansion. The superharmonic resonance split a single resonance peak on the tuned case into several resonance peaks due to weak blade mistuning for steady-state superharmonic resonance response. The amplitude inceased while the damping factor ζ decreased. Also, the response amplitude gets larger when $|\lambda\kappa|$ increases. The resonance amplitude of one blade for the symmetry-broken system increased compared to the tuned case for $0 < \kappa_v < 0.03$, while the other two blades' amplitudes diminished. This implies to the possibility of vibration localization.

In Chapter 4, general responses of a tuned four-degree-of-freedom mass-spring system with parametric excitation were studied. The frequency content and the stability characteristics of the general solution were obtained by assuming a multi-degree-of-freedom Floquet-type solution and applying the harmonic balance method. Later on, this work was extended to the mistuned four-degree-of-freedom system to focus on the effect of symmetry breaking on system response. When we compared the tuned and mistuned stability graphs, numerous instability wedges were observed in the detuned case and showed more tendency to destabilize in general. The instability wedges were based at $\omega = (\omega_i + \omega_j)/N$, where $i = 1, ..., d$, and $j = 1, ..., d$, where d is the degree of freedom, and N is the positive integer. Additionaly, FFT and time response graphs were generated for different sets of parameters and initial conditions for both the tuned and mistuned cases. Then, these results showed good agreement with the numerical simulations done by the ODE solver on MATLAB.

In the first part of Chapter 5, a linear Mathieu eqauation with a constant load was studied to estimate parameters in a linear parametrically excited vibration system. Parameters were calculated approximately by comparing resonant amplitudes to their analytical expressions. We have seen good estimates of γ within a limited range, since the perturbation solution degrades as $\epsilon\gamma$ increases. Although, damping can be diffucult to determine properly in vibration systems, μ was estimated within about 25%. Accuracy depends on the asymptotics of perturbation solutions which constitute the approach.

The second part of Chapter 5 was on the second-order perturbation analysis of a forced nonlinear Mathieu equation. A perturbation expansion of the equation showed the existence of multiple subharmonic and superharmonic resonance cases. An analytical framework was produced by a second-order perturbation expansion method to perceive the system behavior more effectively. The method was applied to determine the stability characteristics based on system parameters, $\gamma, \mu, \epsilon, F, \sigma$ and ω. Primary resonance, superhamonics at orders 2 and 3 and also subharmonics at order $1/2$ were obtained. However, we specifically focused on superharmonic resonance case at $O(\epsilon^2)$ at order 3 to find the terms that can influence the resonance condition for the hard-forced nonlinear Mathieu eqaution. Since wind turbines were invented to perform below the lowest natural frequency level, the existence of superharmonic resonances may be considerably important.

Overall, this thesis presented first and second-order perturbation analyses on both tuned and detuned three-blade wind turbines. Four-degree-of-freedom systems with parametric excitation analysis were also studied.

6.2 Future Work

The study done in this thesis can be extended to the following.

- In Chapter 3, future work can address a formulation of the resulting dynamics of the rotor and the effects of the constant loading. Steady-state response amplitudes can be obtained for superharmonic resonance case at order two. Later, numerical plots can be drawn for all three blades' amplitudes with respect to the detuning parameter, and numerical simulations can be done to verify analytical solutions at order two and three. The effect of nonlinearity on the resonance is also of interest.

- The Floquet-based analysis of four-degree-of-freedom systems with parametric excitation can be applied to mistuned three-blade wind-turbine equations to observe the parametric instabilities behavior in the transient dynamics of coupled blade-hub turbine models.

- The study of parametric identification of the Mathieu equation with a constant load can follow the sensitivity analysis, error analysis, and experiments.

- Second-order perturbation analysis of the forced nonlinear Mathieu equation can be solved analytically and/or numerically, and then numerical simulations can be performed to verify the analytical outcomes.

APPENDICES

APPENDIX A

IN-PLANE THREE-BLADE MISTUNED TURBINE EQUATIONS

A.1 Parameters used in the Equations of Motion

Expressions for the parameters in Equations equation (3.1) and equation (2.2) are given below:

$$
\begin{aligned}
m_b &= \int_0^L \left(m(x)\gamma_v(x)^2 + J_{\zeta\zeta}(x)\gamma_v'(x)^2\right) dx, \\
k_0 &= \int_0^L \mathrm{EI}_{\zeta\zeta}(x)\gamma_v''(x)^2 \, dx, \\
k_1 &= \int_0^L \left(xm(x)\int_0^x \gamma_v'(\xi)^2 \, d\xi - m(x)\gamma_v(x)^2 - J_{\zeta\zeta}(x)\gamma_v'(x)^2\right) dx, \\
k_2 &= \int_0^L gm(x)\left(\int_0^x \gamma_v'(\xi)^2 \, d\xi\right) dx, \\
d &= \int_0^L gm(x)\gamma_v(x) \, dx, \\
e &= \int_0^L (xm(x)\gamma_v(x) + J_{\zeta\zeta}(x)\gamma_v'(x)) \, dx, \\
J_r &= J_{hub} + 3\int_0^L (x^2 m(x) + J_{\zeta\zeta}(x)) \, dx, \\
Q_j &= \int_0^L f_j(x)\gamma_v(x) \, dx, \\
Q_\phi &= \sum_{j=1}^{3}\int_0^L x f_j(x) \, dx.
\end{aligned}
$$

where x is the axis along the length of the undeformed blade, $m(x)$ is mass per unit length, $EI_{\zeta\zeta}$ and $J_{\zeta\zeta}$ are the in-plane bending stiffness and mass moment of inertia per length about the neutral axis, J_{hub} is the hub inertia, γ_v is the assumed modal function, which is the first uniform cantilever beam mode, and $f_j(x)$ accounts for the distributed aerodynamic loads on the j^{th} blade. In these expressions, $()' = d()/dx$.

The flow is assumed to be steady for a simplified model in [43], and the wind speed is assumed to be slightly increasing linearly with height h as $u_{wind} = u_0 + \epsilon h u_1 = u_0 - \epsilon x \cos\phi_j u_1$. Though contribution of state variations on the angle of attack is neglected, the lift force is proportional to

$|\vec{u}_{rel}|^2$, where

$$\begin{aligned} \vec{u}_{blade} &= x\dot{\phi}\hat{y}_j \cdot \vec{u}_{rel} \\ \vec{u}_{rel} &= \vec{u}_{wind} - \vec{u}_{blade}. \end{aligned}$$

$f_j(x)$ and $\vec{u}_{rel}$ are defined as

$$\begin{aligned} \vec{u}_{rel} &= (u_0 - \epsilon x \cos\phi_j u_1)\hat{z} - x\dot{\phi}\hat{y}_j, \\ f_j(x) &= c_p \left[(u_0 - \epsilon x \cos\phi_j u_1)^2 + (x\dot{\phi})^2 \right], \end{aligned}$$

where c_p is a constant which is related the air density, lift coefficient, and other geometric parameters, $\hat{x}_j$ and $\hat{y}_j$ are the axial and the in-plane bending directions of the j^{th} blade, and z is the out-of plane direction.

Inserting $f_j(x)$ into the Q_j and Q_ϕ expressions, we get

$$\begin{aligned} Q_j &= \int_0^L c_p \left(u_0^2 - 2\epsilon u_0 u_1 x \cos\phi_j + \dot{\phi}^2 x^2 + O(\epsilon^2) \right) \gamma_\nu(x)\, dx, \\ Q_\phi &= \sum_{j=1}^{3} c_p \left(u_0^2 \frac{L^2}{2} + \dot{\phi}^2 \frac{L^4}{4} - 2\epsilon u_0 u_1 \cos\phi_j \frac{L^3}{3} + O(\epsilon^2) \right). \end{aligned}$$

Since $\sum_{j=1}^{3} \cos\phi_j = 0$, Q_ϕ can be expressed as $Q_\phi = \hat{Q}_{\phi 0} + \hat{Q}_{\phi 1}\dot{\phi}^2$. Then, Q_j is assumed to have the form of $Q_j = \hat{Q}_{j0} + \epsilon\hat{Q}_{j1}\cos\phi_j + \hat{Q}_{j2}\dot{\phi}^2$ for small ϵ. After $\dot{\phi} = \Omega\nu = \Omega(1 + \epsilon^2\nu_1)$ is plugged into Q_j and Q_ϕ expressions, then they become as follow

$$\begin{aligned} Q_\phi &= \hat{Q}_{\phi 0} + \hat{Q}_{\phi 1}\Omega^2 + O(\epsilon^2) \\ Q_j &= \hat{Q}_{j0} + \hat{Q}_{j2}\Omega^2 + \epsilon\hat{Q}_{j1}\cos\phi_j + O(\epsilon^2). \end{aligned} \tag{A.1}$$

Although, Ω is constant, Q_ϕ and Q_ϕ can be written as

$$\begin{aligned} Q_\phi &= Q_{\phi 0} + O(\epsilon^2) \\ Q_j &= Q_{j0} + \epsilon Q_{j1}\cos\phi_j + O(\epsilon^2). \end{aligned} \tag{A.2}$$

A.2 Modal Frequency Equations and Roots of Coefficient Matrix

As mentioned in section 2.2, third and fourth modal frequency equations are given below:

$$\omega_{n3}^2 = \frac{\epsilon m_b J_r k_v + 2k_1\dot{\phi}^2 m_b J_r + 2k_0 m_b J_r - 2e^2\epsilon k_v - 3e^2 k_1\dot{\phi}^2 - 3e^2 k_0}{2\left(m_b^2 J_r - 3e^2 m_b\right)}$$

$$- \left[\frac{\left(-\epsilon m_b J_r k_v - 2k_1\dot{\phi}^2 m_b J_r - 2k_0 m_b J_r + 2e^2\epsilon k_v + 3e^2 k_1\dot{\phi}^2 + 3e^2 k_0\right)^2}{2\left(m_b^2 J_r - 3e^2 m_b\right)}\right.$$

$$\left. - \frac{4\left(m_b^2 J_r - 3e^2 m_b\right)\left(k_1\epsilon\dot{\phi}^2 J_r k_v + k_0\epsilon J_r k_v + k_1^2\dot{\phi}^4 J_r + 2k_0 k_1\dot{\phi}^2 J_r + k_0^2 J_r\right)}{2\left(m_b^2 J_r - 3e^2 m_b\right)}\right]^{1/2}$$

$$\omega_{n4}^2 = \frac{\epsilon m_b J_r k_v + 2k_1\dot{\phi}^2 m_b J_r + 2k_0 m_b J_r - 2e^2\epsilon k_v - 3e^2 k_1\dot{\phi}^2 - 3e^2 k_0}{2\left(m_b^2 J_r - 3e^2 m_b\right)}$$

$$+ \left[\frac{\left(-\epsilon m_b J_r k_v - 2k_1\dot{\phi}^2 m_b J_r - 2k_0 m_b J_r + 2e^2\epsilon k_v + 3e^2 k_1\dot{\phi}^2 + 3e^2 k_0\right)^2}{2\left(m_b^2 J_r - 3e^2 m_b\right)}\right.$$

$$\left. - \frac{4\left(m_b^2 J_r - 3e^2 m_b\right)\left(k_1\epsilon\dot{\phi}^2 J_r k_v + k_0\epsilon J_r k_v + k_1^2\dot{\phi}^4 J_r + 2k_0 k_1\dot{\phi}^2 J_r + k_0^2 J_r\right)}{2\left(m_b^2 J_r - 3e^2 m_b\right)}\right]^{1/2}$$

In Equation 2.16, we have represantation of the real and imaginary part in matrix form. At steady state solution, the roots of coefficient matrix for non resonant case are:

$$\lambda_3 \;=\; -\zeta - \left[\frac{-\tilde{e}^2\left(3\sqrt{-2\tilde{e}^2\kappa_v + 9\tilde{e}^4 + \kappa_v^2} + 2\kappa_v\right) - \kappa_v\left(\sqrt{-2\tilde{e}^2\kappa_v + 9\tilde{e}^4 + \kappa_v^2} + \kappa_v\right) - 9\tilde{e}^4}{2}\right]^{1/2}$$

$$\lambda_4 = -\zeta + \left[\frac{-\tilde{e}^2\left(3\sqrt{-2\tilde{e}^2\kappa_v + 9\tilde{e}^4 + \kappa_v^2} + 2\kappa_v\right)\kappa_v\left(\sqrt{-2\tilde{e}^2\kappa_v + 9\tilde{e}^4 + \kappa_v^2} + \kappa_v\right) - 9\tilde{e}^4}{2}\right]^{1/2}$$

$$\lambda_5 = -\zeta - \left[\frac{\tilde{e}^2\left(3\sqrt{-2\tilde{e}^2\kappa_v + 9\tilde{e}^4 + \kappa_v^2} - 2\kappa_v\right)\kappa_v\left(\sqrt{-2\tilde{e}^2\kappa_v + 9\tilde{e}^4 + \kappa_v^2} - \kappa_v\right) - 9\tilde{e}^4}{2}\right]^{1/2}$$

$$\lambda_6 = -\zeta + \left[\frac{\tilde{e}^2\left(3\sqrt{-2\tilde{e}^2\kappa_v + 9\tilde{e}^4 + \kappa_v^2} - 2\kappa_v\right) + \kappa_v\left(\sqrt{-2\tilde{e}^2\kappa_v + 9\tilde{e}^4 + \kappa_v^2} - \kappa_v\right) - 9\tilde{e}^4}{2}\right]^{1/2}$$

APPENDIX B

WIND TURBINES PARAMETERS

B.1 Blade's Modal Parameters

System modal parameters for four baseline wind turbine models are calculated by using the data from National Renewable Energy Laboratory's technical report by Rinker and Dykes [58]. The models have four different rated powers as 750 kilowatts [kW], 1.5 megawatts [MW], 3.0 MW, and 5.0 MW. Each baseline model has three identical blades that are placed in an upwind configuration and all four baseline blade models were assumed to consist of a 1.78-mm-thick fiberglass skin of largely triaxial material sandwiching a balsa core for stability [70]. The hub is made of a ductile iron casting in the shape of a sphere with openings for the blades and for the shaft connections. The hub is modeled as a sphere made of ductile iron with openings for the blades and for the shaft connections. The hub height is 20% larger than the rotor diameter and the hub outer diameter is 0.05 times the rotor diameter. The longer blades tend to operate at lower rotor speeds than the shorter blades. The wind turbine parts structural properties for the four baseline models are summarized in Table B.1. The blade and tower structural damping values were not provided in the original WindPACT design files, therefore the damping values obtained in the WindPact 1.5 MW model were provided. We should note that these damping values are substantially higher than those used in the NREL 5 MW model [58]. Jonkman *et al.* [8] provide structural damping ratio as 0.4774% of the critical damping for the NREL offshore 5-MW baseline wind turbine (61.5 meters).

By using the distributed blade structural properties data from National Renewable Energy Laboratory's technical report [58], we have calculated the modal parameters defined in Appendix A.1. The data for 5 MW wind turbine model is provided at Table B.2 as a reference. The 750 kW, 1.5 MW and 3 MW models blade's distributed parameters are tabulated in NREL's technical report [58]. Mass moment of inertia per length about the neutral axis, $J_{\zeta\zeta}$, is not taken into account.

Table B.1: Structural Properties for the Baseline Wind Turbine Models

Parameters	**750 KW**	**1.5 MW**	**3 MW**	**5 MW**
Blade Length (m)	23.75	33.25	47.025	60.8
Blade Mass (kg)	1,941	4,336	13,238	27,854
Hub Inertia about LSS ($kg.m2$)	5,160	29,975	197,987	668,485
Hub Height (m)	60	84	119	154
Hub Diameter (m)	2.5	3.50	4.95	6.40
Rotor Diameter (m)	50	70	99	128
Rotor Mass (kg)	12,381	32,167	101,319	209,407
Tower Mass (kg)	53,776	125,364	351,798	775,094
Nacelle Mass (kg)	20,950	52,839	132,598	270,669
Rated Rotor Speed Ω (rpm)	28.648	20.463	14.469	11.191
Blade first Mass Moment of Inertia ($kg.m$)	14,605	46,497	207,135	563,188
Blade Second Mass Moment of Inertia ($kg.m^2$)	180,640	798,506	5,012,212	17,475,408
Blade Flapwise Structural Damping	3.882% of critical			
Blade Edgewise Structural Damping	5.900% of critical			
Tower Structural Damping, All Modes	3.435% of critical			

The mid-point numerical integration rule is applied to distributed blade structural property data tabulated in [58] and the result is compared with the provided blade mass. The estimations are able to predict the total mass with over 99.7% accuracy as seen in Table B.3. The system modal parameters in the equations of motion in time domain can be found in Table B.4. Only edgewise natural frequencies for baseline models, ω_{n2} are provided in the table.

Edgewise and flapwise modal natural frequencies for 61.5 meter blade are found by method of assumed mode. These values are compared with NREL and Sandia's results in Table B.5. National laboratories have used different type of methods to find blade natural frequencies. In [71], [72] and [73], we have found the reference data to compare. Jonkman *et. al* [71] from NREL have used FAST and ADAMS, although Resor *et. al* from Sandia have used ANSYS [72] and BMODES [73] softwares to calculate the blade modal frequencies. Total mass of the blade is 17740 kg, rated rotor speed is 12.1 rpm and blade tip speed is 80 m/s. Since single assumed mode is taken into account in our calculation, flapwise and edgewise modal frequencies are slightly higher than NREL and Sandia. When the number of assumed modes is increased, the modal natural frequencies will approach convergence to their reference values.

B.2 The Relation Between the Blade Size and the Parametric Effects

The parametric effects become more significant when horizontal axis wind turbine blades get longer. As wind turbine blades are designed longer, their thickness is not necessarily changed in the same proportion, and is more likely to change in a smaller proportion such that the blades become relatively more slender with increasing size. The length of NREL's 23.75 m, 33.25m, 47.025 m and 60.8 m baseline models are scaled while the other dimensions are kept the same to investigate the effect of blade size on the parametric effects. In a worst-case scenario, the length of the blades in Table B.4 is multiplied by two and three, while the crosssectional area is kept the same.

While parametric stiffness ratios for the 5.0 MW model is 0.0623 for the doubled length blade, it is 0.21 for the 3 times scaled up blade which is about 27 times higher than the original blade's ratio as seen in Table B.6. Scaling only the length caused dramatic changes in the parametric effects. Since we have only scaled the length of the blades instead of scaling the whole volume, these values draw the worst scenario in the sense of parametric effects on the systems. Scaling the whole blade would result in a linear-like increase in the parametric effects with increasing length. Then, we expect a realistic blade trend to be somewhere between the scaled length and volume ratios. Therefore we can conclude that as the blades get longer in length, the parametric effects become more meaningful.

As seen from Figure B.1, the ratio of the parametric and elastic modal stiffnesses is estimated for the scaled versions of the NREL's blades for four models to present the relation between the blade size and the parametric effects.

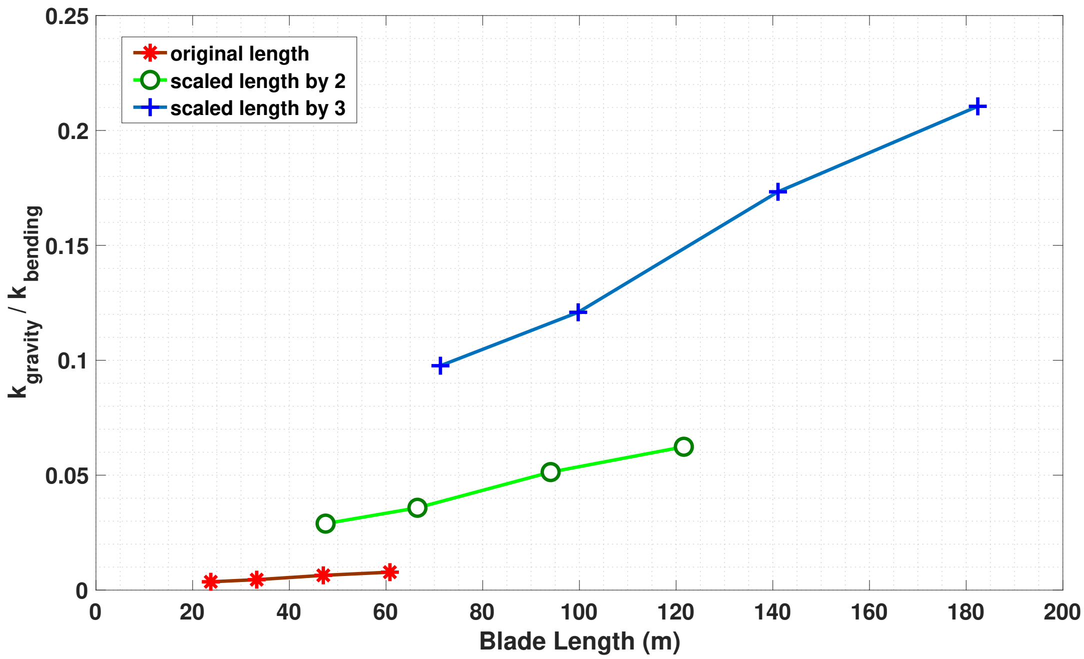

Figure B.1: Parametric stiffness ratios for scaled blade models and actual blade models

Natural frequencies are found at different rotation angles to show the significance of the gravity's parametric effect. The blade natural frequencies alter with the rotor angle, ϕ, due the gravity has stiffening and softening effects. When the blade is upright, $\phi = \pi$, the gravitational force compresses it, and makes the blade less stiff in bending. When the rotor angle is $\phi = 0$, the gravitational force pulls the blade and increases the blade's bending stiffness. These variations in stiffness can be estimated from the natural frequencies. For a blade with modal mass m_b, elastic stiffness k_0 and parametric stiffness, k_2, due to gravity, the system natural frequency in upright, horizontal and downward positions can be calculated respectively as follow:

$$\omega_u = \sqrt{\frac{k_0 - k_2}{m_b}}, \quad \omega_h = \sqrt{\frac{k_0}{m_b}}, \quad \omega_d = \sqrt{\frac{k_0 + k_2}{m_b}}.$$

The ratio of the frequencies of downward and horizontal orientations is

$$\frac{\omega_d}{\omega_h} = \sqrt{\frac{k_0 + k_2}{k_0}}$$

where ω_d and ω_h are downward and horizontal blade frequencies, respectively. Therefore the ratio of the parametric stiffness to elastic stiffness can be found as

$$\frac{k_2}{k_0} = \left(\frac{\omega_d}{\omega_h}\right)^2 - 1.$$

In the Table B.7, modal natural frequencies of baseline blade models are provided for different positions.

The parametric effect is estimated for scaled versions of the NREL's blades by using expression $k_2/k_0 = \omega_d^2/\omega_h^2 - 1$. Modal frequencies for scaled blade models of NREL 60.8 meter wind turbine are provided for different position to show the effect of parametric stiffness due to gravity in Table B.8. Additionaly, Table B.9 present how the parametric effect becomes more significant by increasing the length of blades.

Actual and scaled-length blade tip placements are obtained for superharmonic resonances at order 2 and 3 in Figure B.2. Red and blue lines show the scaled length blade tip displacement for superharmonic resonances at order 2 and 3 but these tip displacements are stand for upper bound of the modal coordinate amplitude. Damping ratio is taken $\zeta = 5.9$ for blades $L < 64$, and $\zeta = 0.477$ for blades $L \leq 64$. Jason Jonkman *et al.* [8] provide damping factor as $\zeta = 0.477$ for 64-meter 5-mw reference wind turbine. Although Dykes and Rinker [58] stated that $\zeta = 5.9$ is for 35-meter blade, they have used same damping factor for 25, 35, 49 and 64-meter blades. Therefore, we were not able to find the damping ratios for longer blades, we only applied these two damping ratios in out plots.

Parametric effect on actual and scaled-length blade tip placements are investigated for superharmonic resonances at order 2 in Figure B.3. When blade is shorter, parametric effect is not powerful, but when blade gets longer, it becomes meaningful. Since we only scaled the blades lenghtwise, these tip displacement values give the worst-case scenario in terms of the parametric stiffness effect.

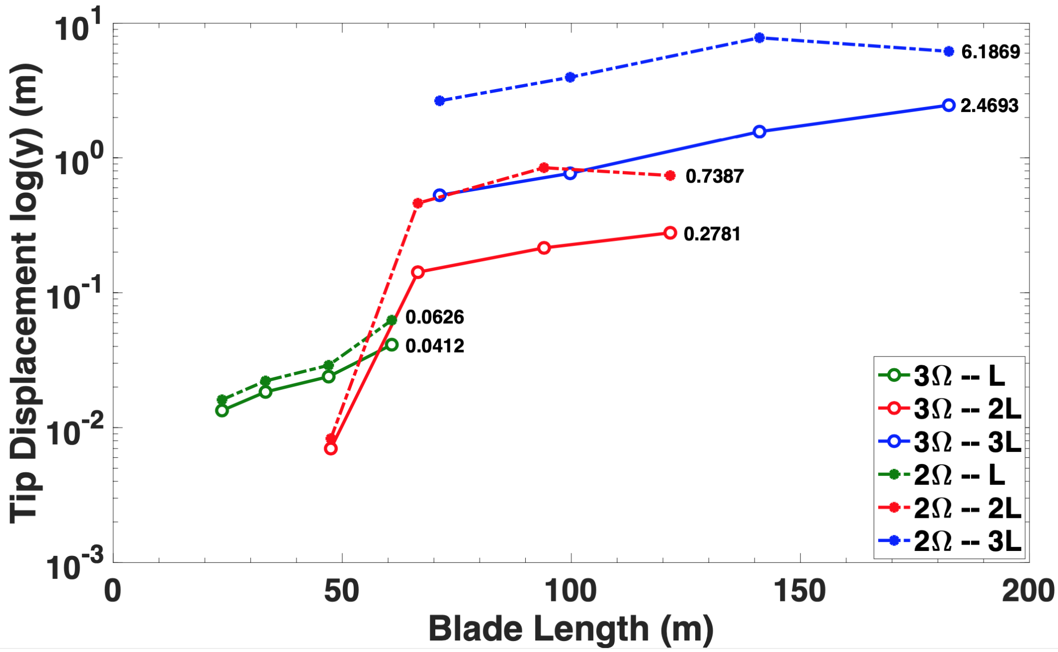

Figure B.2: Superharmonic resonance order effect on actual and scaled blade tip displacement

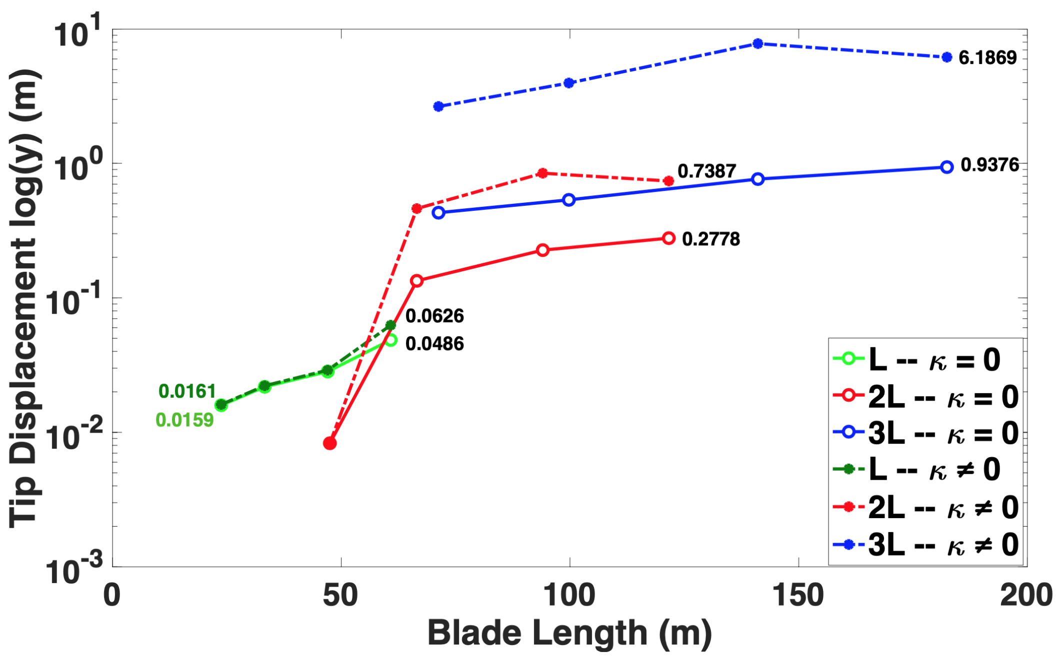

Figure B.3: Parametric effect on actual and scaled blade tip displacement for superharmanic resonance at order 2

Table B.2: Distributed blade structural properties for the 5 MW model taken from NREL

Radius (m)	Δr	**Mass Denstiy** (kg/m)	**Edgewise Stiffness EI** ($N.m^2$)
3.2	3.2	3708.41	6.37E+10
4.5	1.3	622.32	1.40E+10
6.4	1.9	632.67	1.38E+10
9.6	3.2	649.91	1.34E+10
12.8	3.2	667.16	1.30E+10
16	3.2	684.4	1.26E+10
19.2	3.2	650.77	1.06E+10
22.4	3.2	617.15	8.58E+09
25.6	3.2	583.52	6.57E+09
28.8	3.2	549.9	4.55E+09
32	3.2	516.27	2.54E+09
35.2	3.2	458.05	2.15E+09
38.4	3.2	399.83	1.77E+09
41.6	3.2	341.6	1.38E+09
44.8	3.2	283.38	9.96E+08
48	3.2	225.16	6.10E+08
51.2	3.2	184.52	4.99E+08
54.4	3.2	143.89	3.88E+08
57.6	3.2	103.25	2.76E+08
60.8	3.2	62.62	1.65E+08
64	3.2	21.99	5.36E+07

Table B.3: Blade mass comparison for baseline model and mid-point numerical integration method (Mid-point I.M.)

Baseline Models	**750 kW**	**1.5 MW**	**3.0 MW**	**5.0 MW**
Provided Blade Mass (kg)	1,941	4,336	13,238	27854
Blade Mass by Mid-point I.M. (kg)	1935.8	4326.6	13216	27843
Accuracy Rate (%)	99.73209686	99.78321033	99.83381175	99.96050837

Table B.4: Blade modal parameters for baseline wind turbine models

Baseline Models	**750 kW**	**1.5 MW**	**3.0 MW**	**5.0 MW**
Length from center m	25	35	49.5	64
Blade Length (m)	23.75	33.25	47.025	60.8
Modal Mass m_b (kgm^2)	997.0195	1904.3	6963.9	14441
Elastic stiffness k_0 (Nm)	224610	246280	453990	603670
Centrifugal Stiffness k_1 (kgm^2)	303.5731	598.3964	2149.8	4479.3
Gravitational Stiffness k_2 (Nm)	812.2177	1118	2914.3	4706.5
Direct Gravitational term d (Nm)	1340.2	2010.9	4816	7861.8
Coupling Term e (kgm^2)	14449	41953	201430	541840
Total Inertia J_r (kgm^2)	666600	2957400	18578000	64311000
$\epsilon = m_b/J_r$	0.001495679	0.00064391	0.000374847	0.000224549
k_0/k_1	739.887691	411.5666471	211.177784	134.7688255
$\omega_{n2} = \sqrt{\frac{(k_0 + k_1 * \Omega^2)}{m_b}}$ (Hz)	2.404520805	1.820943987	1.292662632	1.034768525
k_2/k_0	0.003616124	0.004539548	0.006419304	0.007796478

Table B.5: Blade modal frequencies (Hz) comparison with the data from NREL and SANDIA

	NREL		**SANDIA**		**Calculated**
Method	FAST	ADAMS	ANSYS	BMODES	Assumed Modes
Flapwise	0.69	0.70	0.87	0.95	1.09
Edgewise	1.089	1.087	1.060	1.240	1.240

Table B.6: Parametric effect for scaled blade size

Baseline Models	**750 kW**	**1.5 MW**	**3.0 MW**	**5.0 MW**
k_2/k_0 for L	0.003616124	0.004539548	0.006419304	0.007796478
k_2/k_0 for 2L	0.028928222	0.035818937	0.051354209	0.062372446
k_2/k_0 for 3L	0.097634055	0.120885609	0.173315492	0.210506306

Table B.7: Modal frequencies (Hz) for the baseline blade models

Baseline Models	**750 kW**	**1.5 MW**	**3.0 MW**	**5.0 MW**
$\omega_d(\phi = 0)$	2.394345889	1.814975491	1.289812899	1.033541542
$\omega_h(\phi = \pi/2)$	2.390028468	1.810869879	1.285692873	1.029535957
$\omega_u(\phi = \pi)$	2.385703234	1.806754938	1.281559603	1.025514726

Table B.8: Modal frequencies (Hz) for the scaled blade models of NREL 60.8 m

Blade Length	**L=60.8 m**	**2L=2*60.8**	**3L=3*60.8**
$\omega_d(\phi = 0)$	1.033541542	0.265283507	0.125856627
$\omega_h(\phi = \pi/2)$	1.029535957	0.257378254	0.114391185
$\omega_u(\phi = \pi)$	1.025514726	0.249222376	0.101640523

Table B.9: Parametric effect (k_2/k_0) for the scaled blade of NREL baseline models

Scaled Length	(k_2/k_0) **for L**	(k_2/k_0) **for 2L**	(k_2/k_0) **for 3L**
L=23.75 m	0.003616124	0.028928222	0.097634055
L=33.25 m	0.004539548	0.035818937	0.120885609
L=49.5 m	0.006419304	0.051354209	0.173315492
L=60.8 m	0.007796478	0.062372446	0.210506306

APPENDIX C

SECOND-ORDER PERTURBATION ANALYSIS OF IN-PLANE THREE-BLADE TUNED AND MISTUNED TURBINES

C.1 Superharmonic Case at Order 3 at $O(\epsilon^2)$

Coefficients of X and Y terms in Equation (3.21) and Equation (3.22) are given below

$$z_1 = -\frac{1}{2}(\zeta\epsilon)$$

$$z_2 = -\frac{\epsilon^2\tilde{e}^2\zeta}{2}$$

$$z_3 = -\frac{1}{2}\epsilon\kappa_{v_j} + \frac{1}{8}\epsilon^2\zeta^2 + \frac{1}{8}\epsilon^2\kappa_{v_j}^2 + \epsilon\sigma$$

$$z_4 = -\frac{\epsilon^2\tilde{e}^2\kappa_{v_j}}{4} - \frac{9\epsilon^2\tilde{e}^4}{8} - \frac{\epsilon\tilde{e}^2}{2}$$

$$z_5 = -\epsilon^2\kappa^2\lambda$$

where $\lambda = \frac{F_{j0}}{16(1-\omega_1^2)(1-4\omega_1^2)}$

C.2 Superharmonic Case at Order 2 at $O(\epsilon^2)$

C.2.1 Mistuned case coefficients

Coefficients of reconstituted differential equation's real part from Equation (3.35), and imaginary part from Equation (3.36) are

$$C_1 = -\frac{1}{2}(\zeta\epsilon)$$

$$C_2 = -\frac{\epsilon^2\tilde{e}^2\zeta}{2}$$

$$C_3 = -\frac{1}{2}\epsilon\kappa_{v_j} + \frac{1}{8}\epsilon^2\zeta^2 + \frac{1}{8}\epsilon^2\kappa_{v_j}^2 + \epsilon\sigma$$

$$C_4 = -\frac{\epsilon^2\tilde{e}^2\kappa_{v_j}}{4} - \frac{9\epsilon^2\tilde{e}^4}{8} - \frac{\epsilon\tilde{e}^2}{2}$$

$$C_5 = \frac{\epsilon^2\kappa\tilde{e}^2\omega_1^2}{8(1-\omega_1^2)}$$

$$C_6 = -\frac{\epsilon^2\kappa F_{j0}\zeta}{32(1-\omega_1^2)} - \frac{\epsilon^2\kappa F_{j1}}{8(1-\omega_1^2)} + \frac{\epsilon^2\zeta\kappa F_{j0}\omega_1}{16(1-\omega_1^2)^2} + \frac{\epsilon^2\kappa^2 F_j}{16(1-\omega_1^2)}$$

$$C_7 = \frac{\epsilon\kappa F_{j0}}{8(1-\omega_1^2)} - \frac{\epsilon^2\kappa F_{j0}\kappa_{v_j}}{32(1-\omega_1^2)}$$

$$C_8 = \frac{\epsilon^2 3\tilde{e}^2\kappa F_{j0}}{32(1-\omega_1^2)}$$

C.2.2 Tuned case coefficients

Coefficients of real (3.37) and imaginary (3.38) parts of reconstituted differential equation for tuned system are

$$T_1 = -\frac{1}{2}\left(\zeta\epsilon\right)$$

$$T_2 = -\frac{\epsilon^2\tilde{e}^2\zeta}{2}$$

$$T_3 = \frac{1}{8}\epsilon^2\zeta^2 + \epsilon\sigma$$

$$T_4 = -\frac{9\epsilon^2\tilde{e}^4}{8} - \frac{\epsilon\tilde{e}^2}{2}$$

$$T_5 = \frac{\epsilon^2\kappa\tilde{e}^2\omega_1^2}{8(1-\omega_1^2)}$$

$$T_6 = -\frac{\epsilon^2\kappa F_{j0}\zeta}{32(1-\omega_1^2)} - \frac{\epsilon^2\kappa F_{j1}}{8(1-\omega_1^2)} + \frac{\epsilon^2\zeta\kappa F_{j0}\omega_1}{16(1-\omega_1^2)^2} + \frac{\epsilon^2\kappa^2 F_j}{16(1-\omega_1^2)}$$

$$T_7 = \frac{\epsilon\kappa F_{j0}}{8(1-\omega_1^2)}$$

$$T_8 = \frac{\epsilon^2 3\kappa\tilde{e}^2 F_{j0}}{32(1-\omega_1^2)}$$

APPENDIX D

SECOND-ORDER PERTURBATION ANALYSIS OF NONLINEAR MATHIEU EQUATION WITH HARD EXCITATION

$Z's$ terms from Equations (5.20) and (5.19) in section 5.2.7 are

$$Z_0 = -\frac{6\epsilon^2\alpha\mu\Omega F^3}{8(\omega^2-\Omega^2)^4} + \frac{6\epsilon^2\alpha^2 F^5}{128\omega^2(\omega^2-\Omega^2)^5} + \frac{\epsilon^2\alpha\mu F^3}{16\omega(\omega^2-\Omega^2)^3}$$

$$Z_1 = \frac{\epsilon^2\alpha\sigma F^3}{16\omega(\omega^2-\Omega^2)^3} + \frac{9\epsilon^2\alpha^2 F^3}{32(\omega^2-\Omega^2)^6} - \frac{\epsilon\alpha F^3}{8(\omega^2-\Omega^2)^3}$$

$$Z_2 = Z_3 = \frac{3\epsilon^2\alpha^2 F^3}{32\omega^2(\omega^2-\Omega^2)^3} + \frac{18\epsilon^2\alpha^2 F^3}{8(\omega^2-\Omega^2)^4} + \frac{9\epsilon^2\alpha^2 F^3}{8(\omega^2-(2\Omega-\omega)^2)(\omega^2-\Omega^2)^3}$$

$$+\frac{9\epsilon^2\alpha^2 F^3}{8(\omega^2-(2\Omega+\omega)^2)(\omega^2-\Omega^2)^3}$$

$$Z_6 = 2Z_5 = -2Z_4 = -\frac{6\epsilon^2\alpha^2 F^3}{32\omega^2\omega(\omega^2-\Omega^2)^3}$$

$$Z_7 = -Z_{10} = -2\epsilon\mu\omega$$

$$Z_8 = Z_9 = 2\epsilon\omega\sigma + \epsilon^2\mu^2 - \frac{6\epsilon\alpha F^2}{4(\omega^2-\Omega^2)^2} + \epsilon^2\left(\frac{\gamma^2}{4(\omega^2-(\Omega+\omega)^2)} + \frac{\gamma^2}{4(\omega^2-(\Omega-\omega)^2)}\right.$$

$$\left.+\frac{9\alpha^2 F^4}{(\omega^2-(2\Omega+\omega)^2)} + +\frac{9\alpha^2 F^4}{(\omega^2-(2\Omega-\omega)^2)}\right) + \frac{18\epsilon^2\alpha^2 F^4}{16(\Omega^2-\omega^2)^5} - \frac{36\epsilon^2\alpha^2 F^4}{64\omega^2(\omega^2-\Omega^2)}$$

$$Z_{11} = Z_{23} = -Z_{24} = -Z_{25} = \frac{6\epsilon^2\alpha\mu}{2\omega}$$

$$Z_{12} = Z_{14} = Z_{18} = Z_{19} = -3\epsilon\alpha + \frac{36\epsilon^2\alpha^2F^2}{16\omega^2(\omega^2-\Omega^2)^2} + \frac{\epsilon^2\alpha^2F^2}{8\omega(\omega^2-\Omega^2)^2} + \frac{36\epsilon^2\alpha^2F^2}{4(\omega^2-\Omega^2)^3}$$

$$+ \frac{9\epsilon^2\alpha^2F^2}{4(\omega^2-\Omega^2)}\left(\frac{1}{\omega^2-(\Omega-2\omega)^2} + \frac{1}{\omega^2-(\Omega+2\omega)^2}\right)$$

$$Z_{15} = Z_{16} = 2Z_{13} = 2Z_{17} = 2Z_{20} = 2Z_{21} = \frac{15\epsilon^2\alpha^2}{4\omega^2}$$

$$Z_{22} = \frac{\epsilon^2\gamma^2F}{4(\omega^2-4\Omega^2)(\omega^2-\Omega^2)}$$

BIBLIOGRAPHY

BIBLIOGRAPHY

[1] Venkatanarayanan Ramakrishnan. *Analysis of Wind Turbine Blade Vibration and Drivetrain Loads*. PhD thesis, Michigan State University, 2017.

[2] Global Wind Energy Council. Global wind report annual market update. online, 2017. http://www.gwec.net/global-figures/graphs/.

[3] U.S Department Energy Information Admisnistration. Today in energy. online, 2017. https://www.eia.gov/todayinenergy/detail.php?id=31632.

[4] U.S. Department of Energy. The wind vision road map: A pathway forward. online, 2014. https://www.energy.gov/eere/wind/maps/wind-vision.

[5] World Energy Council. World energy resources wind,2016. online, 2016. https://www.worldenergy.org/wp-content/uploads/2017/03/WEResources_Wind_2016.pdf.

[6] Us Depatment of Energy. 2015 wind technologies market report. online, 2015. https://www.energy.gov/sites/prod/files/2016/08/f33/2015-Wind-Technologies-Market-Report-08162016.pdf.

[7] D Todd Griffith and Thomas D Ashwill. The sandia 100-meter all-glass baseline wind turbine blade: Snl100-00. *Sandia National Laboratories, Albuquerque, Report No. SAND2011-3779*, page 67, 2011.

[8] Jason Jonkman, Sandy Butterfield, Walter Musial, and George Scott. Definition of a 5-mw reference wind turbine for offshore system development. *National Renewable Energy Laboratory, Golden, CO, Technical Report No. NREL/TP-500-38060*, 2009.

[9] C Lindenburg. Aeroelastic modelling of the lmh64-5 blade. *Energy Research Center of the Netherlands, Technical Report No. DOWEC-02-KL-083/0, DOWEC 10083_001*, 2002.

[10] GE Renewable Energy. Haliade-x offshore wind turbine platform. online, 2018. https://www.ge.com/renewableenergy/wind-energy/turbines/haliade-x-offshore-turbine.

[11] George Scott Tyler Stehly, Donna Heimiller. 2016 cost of wind energy review. online, 2016. https://www.nrel.gov/docs/fy18osti/70363.pdf.

[12] Shuangwen Sheng. Report on wind turbine subsystem reliability?a survey of various databases. *National renewable energy laboratory-NREL/PR-5000-59111*, 2013.

[13] M.R.M. Crespo da Silva. Nonlinear flexural-flexural-torsional-extensional dynamics of beams. i. formulation. *International Journal of Solids and Structures*, 24(12):1225–1234, 1988.

[14] Gunjit S Bir and Francisco Oyague. *Estimation of blade and tower properties for the gearbox research collaborative wind turbine*. National Renewable Energy Laboratory, 2007.

[15] Bjarne Skovmose Kallesøe. Equations of motion for a rotor blade, including gravity, pitch action and rotor speed variations. *Wind Energy*, 10(3):209–230, 2007.

[16] Venkatanarayanan Ramakrishnan and Brian F Feeny. In-plane nonlinear dynamics of wind turbine blades. In *ASME 2011 International Design Engineering Technical Conferences and Computers and Information in Engineering Conference*, pages 761–769. American Society of Mechanical Engineers, 2011.

[17] Gizem Acar and Brian F Feeny. Linear modal analysis of a horizontal-axis wind turbine blade. In *Special Topics in Structural Dynamics, Volume 6*, pages 125–131. Springer, 2015.

[18] Venkatanarayanan Ramakrishnan and Brian F Feeny. Resonances of a forced Mathieu equation with reference to wind turbine blades. *Journal of Vibration and Acoustics*, 134(6):064501, 2012.

[19] Acar Gizem D. and Feeny Brian F. Bend-bend-twist vibrations of a wind turbine blade. *Wind Energy*, 21(1):15–28, 2017. doi: 10.1002/we.2141. URL https://onlinelibrary.wiley.com/doi/abs/10.1002/we.2141.

[20] Dayuan Ju and Qiao Sun. Modeling of a wind turbine rotor blade system. *Journal of Vibration and Acoustics*, 139(5):051013, 2017.

[21] Venkatanarayanan Ramakrishnan and Brian F Feeny. Second order perturbation analysis of a forced nonlinear Mathieu equation. In *ASME 2012 International Design Engineering Technical Conferences and Computers and Information in Engineering Conference*, pages 1073–1082. American Society of Mechanical Engineers, 2012.

[22] Ayse Sapmaz and Brian F Feeny. Second-order perturbation analysis of in-plane blade-hub dynamics of horizontal-axis wind turbines. In *ASME 2018 International Design Engineering Technical Conferences and Computers and Information in Engineering Conference*, pages V008T10A027–V008T10A027. American Society of Mechanical Engineers, 2018.

[23] Tsuyoshi Inoue, Yukio Ishida, and Takashi Kiyohara. Nonlinear vibration analysis of the wind turbine blade (occurrence of the superharmonic resonance in the out of plane vibration of the elastic blade). *Journal of Vibration and Acoustics*, 134(3):031009, 2012.

[24] Yukio Ishida, Tsuyoshi Inoue, and Kohei Nakamura. Vibration of a wind turbine blade (theoretical analysis and experiment using a single rigid blade model). *Journal of Environment and Engineering*, 4(2):443–454, 2009.

[25] Brian Fredrik Feeny. Identification of nonlinear ship motion using perturbation techniques. Master's thesis, Virginia Polytechnic Institute and State University, 1986.

[26] Ali H Nayfeh. Perturbation methods in nonlinear dynamics. In *Lecture Notes in Physics*, pages 238–314. Springer, 1986.

[27] M Sayed and YS Hamed. Stability and response of a nonlinear coupled pitch-roll ship model under parametric and harmonic excitations. *Nonlinear Dynamics*, 64(3):207–220, 2011.

[28] Vahid Zamani, Ehsan Kharazmi, and Ranjan Mukherjee. Asymmetric post-flutter oscillations of a cantilever due to a dynamic follower force. *Journal of Sound and Vibration*, 340:253–266, 2015.

[29] Ali H Nayfeh and Dean T Mook. *Nonlinear Oscillations*. John Wiley & Sons, New York, 2008.

[30] Lawrence Ruby. Applications of the Mathieu equation. *American Journal of Physics*, 64(1): 39–44, 1996.

[31] Yan Li, Shangchun Fan, Zhanshe Guo, Jing Li, Le Cao, and Haihan Zhuang. Mathieu equation with application to analysis of dynamic characteristics of resonant inertial sensors. *Communications in Nonlinear Science and Numerical Simulation*, 18(2):401–410, 2013.

[32] Gizem Acar and Brian F Feeny. Approximate general responses of multi-degree-of-freedom systems with parametric stiffness. In *Special Topics in Structural Dynamics, Volume 6*, pages 211–219. Springer, 2016.

[33] Ilaria Panardo. Stability of periodic systems and floquet theory. 2014.

[34] R. Rand. Lecture notes on nonlinear vibrations. Published online, 2012. http://www.math.cornell.edu/~rand/randdocs/nlvibe52.pdf.

[35] Norman W McLachlan. *Theory and Application of Mathieu Functions*. Dover, New York, 1961.

[36] Andrew Peterson and Malcolm Bibby. *Accurate Computation of Mathieu Functions*. Morgan & Claypool Publishers, San Rafael, 2013.

[37] DB Hodge. *The calculation of the eigenvalues and eigenfunctions of Mathieu's equation*, volume 1937. National Aeronautics and Space Administration, 1972.

[38] Matthew S Allen, Michael W Sracic, Shashank Chauhan, and Morten Hartvig Hansen. Output-only modal analysis of linear time-periodic systems with application to wind turbine simulation data. *Mechanical Systems and Signal Processing*, 25(4):1174–1191, 2011.

[39] AS Alsuwaiyan and Steven W Shaw. Performance and dynamic stability of general-path centrifugal pendulum vibration absorbers. *Journal of Sound and Vibration*, 252(5):791–815, 2002.

[40] W Ker Wilson. *Pratical Solution of Torsional Vibration Problems Chapter XXX*. Chapman & Hall, London, 1968.

[41] Chang-Po Chao, SW Shaw, and Cheng-Tang Lee. Stability of the unison response for a rotating system with multiple tautochronic pendulum vibration absorbers. *Journal of Applied Mechanics*, 64(1):149–156, 1997.

[42] C-P Chao, C-T Lee, and SW Shaw. Non-unison dynamics of multiple centrifugal pendulum vibration absorbers. *Journal of Sound and Vibration*, 204(5):769–794, 1997.

[43] Gizem Acar, Mustafa A Acar, and Brian F Feeny. In-plane blade-hub dynamics in horizontal-axis wind-turbines. In *ASME 2016 International Design Engineering Technical Conferences and Computers and Information in Engineering Conference*, pages V008T10A046–V008T10A046. American Society of Mechanical Engineers, 2016.

[44] Takashi Ikeda, Yuji Harata, and Yukio Ishida. Unstable vibrations of a wind turbine tower with two blades. In *ASME 2012 International Design Engineering Technical Conferences and Computers and Information in Engineering Conference*, pages 757–766. American Society of Mechanical Engineers Digital Collection, 2012.

[45] A Sinha and JH Griffin. Stability of limit cycles in frictionally damped and aerodynamically unstable rotor stages. *Journal of Sound and Vibration*, 103(3):341–356, 1985.

[46] AJ Dick, B Balachandran, and CD Mote. Intrinsic localized modes in microresonator arrays and their relationship to nonlinear vibration modes. *Nonlinear Dynamics*, 54(1-2):13–29, 2008.

[47] AV Srinivasan and HM Frye. Effects of mistuning on resonant stresses of turbine blades. *Structural Dynamic Aspects of Bladed Disk Assemblies*, pages 57–71, 1976.

[48] H Dare Afolabi. *Vibration of mistuned bladed disc assemblies.* PhD thesis, Imperial College London (University of London), 1982.

[49] JH Griffin and TM Hoosac. Model development and statistical investigation of turbine blade mistiming. *ASME Journal of Vibration, Acoustics, Stress, Reliability in Design*, 106:204–210, 1984.

[50] Marlin Kruse and Christophe Pierre. Forced response of mistuned bladed disks using reduced-order modeling. In *37th Structure, Structural Dynamics and Materials Conference*, page 1545, 1996.

[51] DS Whitehead. Research note: effect of mistuning on forced vibration of blades with mechanical coupling. *Journal of Mechanical Engineering Science*, 18(6):306–307, 1976.

[52] D J_ Ewins. The effects of detuning upon the forced vibrations of bladed disks. *Journal of Sound and Vibration*, 9(1):65IN273–7279, 1969.

[53] Douksoon Cha and Alok Sinha. Computation of the optimal normal load for a mistuned and frictionally damped bladed disk assembly under different types of excitation. *Journal of Computational and Nonlinear Dynamics*, 6(2):021012, 2011.

[54] Takashi Ikeda, Yuji Harata, and Yukio Ishida. Parametric instability and localization of vibrations in three-blade wind turbines. *Journal of Computational and Nonlinear Dynamics*, 13(7):071001, 2018.

[55] Ayse Sapmaz, Gizem D Acar, and Brian F Feeny. Approximate general responses of tuned and mistuned 4-degree-of-freedom systems with parametric stiffness. In *Topics in Modal Analysis & Testing, Volume 9*, pages 315–324. Springer, 2019.

[56] Thomas M. Theisen. Gravity's effect on centrifugal pendulum vibration absorbers. M.S. Thesis, Michigan State University, 2011.

[57] Brian J Olson, Steven W Shaw, Chengzhi Shi, Christophe Pierre, and Robert G Parker. Circulant matrices and their application to vibration analysis. *Applied Mechanics Reviews*, 66(4):040803, 2014.

[58] Katherine L Dykes and Jennifer Rinker. Windpact reference wind turbines. Technical report, National Renewable Energy Lab.(NREL), Golden, CO (United States), 2018.

[59] M. Acar G. Acar and B. F. Feeny. Parametric resonances of a three-blade-rotor system with reference to wind turbines. *Journal of Vibration and Acoustics*, 2020.

[60] Ayse Sapmaz, Gizem D Acar, and Brian Feeny. In-plane blade-hub dynamics of horizontal-axis wind turbine with mistuned blades. In *ASME 2017 International Design Engineering Technical Conferences and Computers and Information in Engineering Conference*, pages V008T12A033–V008T12A033. American Society of Mechanical Engineers, 2017.

[61] Ayse Sapmaz, Gizem D Acar, and Brian F Feeny. Numerical study of superharmonic resonances in a mistuned horizontal-axis wind-turbine blade-rotor set. In *ASME 2019 International Design Engineering Technical Conferences and Computers and Information in Engineering Conference*. American Society of Mechanical Engineers Digital Collection.

[62] Ali H Nayfeh. Parametric identification of nonlinear dynamic systems. In *Advances and Trends in Structures and Dynamics*, pages 487–493. Elsevier, 1985.

[63] WI Newman, RH Rand, and AL Newman. Dynamics of a nonlinear parametrically excited partial differential equation. *Chaos: An Interdisciplinary Journal of Nonlinear Science*, 9(1): 242–253, 1999.

[64] Leslie Ng and Richard Rand. Bifurcations in a mathieu equation with cubic nonlinearities. *Chaos, Solitons & Fractals*, 14(2):173–181, 2002.

[65] DB Marghitu, SC Sinha, and D Boghiu. Stability and control of a parametrically excited rotating system. part i: Stability analysis. *Dynamics and Control*, 8(1):5–18, 1998.

[66] Manoj Pandey, Richard H Rand, and Alan T Zehnder. Frequency locking in a forced mathieu–van der pol–duffing system. *Nonlinear Dynamics*, 54(1-2):3–12, 2008.

[67] Leslie Anne Month and Richard H Rand. Bifurcation of 4: 1 subharmonics in the nonlinear mathieu equation. *Mech. Res. Commun*, 9(4):233–240, 1982.

[68] Ali H. Nayfeh and Dean T. Mook. *Nonlinear Oscillations*. Wiley Interscience Publications. John Wiley and Sons, New York, 1979.

[69] Louis Anthony Romero, John R Torczynski, and Andrew M Kraynik. A scaling law near the primary resonance of the quasiperiodic mathieu equation. *Nonlinear Dynamics*, 64(4): 395–408, 2011.

[70] DJ Malcolm and AC Hansen. Windpact turbine rotor design study. national renewable energy laboratory. Technical report, Report No. NREL/SR-500-32495, 2006.

[71] J Jonkman, S Butterfield, W Musial, and G Scott. Definition of a 5-mw reference wind turbine for offshore system development nrel. *Golden CO*, 2009.

[72] Brian R Resor, David C Maniaci, Jonathan C Berg, and Phillip Richards. Effects of increasing tip velocity on wind turbine rotor design. *Sandia National Laboratories: SAND2013-XXXX*, 2013.

[73] Brian R Resor. Definition of a 5mw/61.5 m wind turbine blade reference model. *Albuquerque, New Mexico, USA, Sandia National Laboratories, SAND2013-2569*, 2013, 2013.